

**Master of Science Thesis****Isolated Bi-directional DC-DC  
Converter for a PEM Fuel Cell  
Energy Management System****EPE 2005-05      Abdelhafid El Bouhali****Coaches:**    Dr. Jorge Duarte (TU/e, The Netherlands)  
                 Ir. Marcel Hendrix (TU/e and Philips Lighting)**Eindhoven, March 2005**

# Abstract

As part of my master thesis I have taken part in the Electromechanics and Power Electronics (EPE) group of the Eindhoven University of Technology (TU/e). During my graduation period, research has been done on a  $1kW$ ,  $100kHz$  Bi-directional DC-DC converter for a Fuel Cell energy management system. As the Fuel Cell has a slow response, this converter should operate a secondary energy source, such as a battery, during the start up process of the Fuel cell. Furthermore, a literature research on a Front end DC-DC converter has been carried out. The Front end DC-DC converter is presented in chapter 2.

After a literature study, a converter topology for the Bi-directional DC-DC converter has been chosen. This resulted in an active clamp converter during discharging mode of operation and a phase shifted converter during charging mode of operation. This converter has two active switch bridges on both sides of an isolation transformer. The bridge on the high voltage side fed by a voltage source (referred to as voltage fed full-bridge) and the bridge on the low voltage side fed by a current source (referred to as current-fed full bridge).

The active clamp branch consisting of an active switch and an energy storage capacitor which is placed across the current-fed bridge, can be used to achieve soft switching for the voltage-fed bridge switches in charging mode, and clamp the transient voltage during discharging mode. Furthermore, in case of boost mode it limits the overshoot of the bridge switch's turn off voltage and enables the energy stored in the transformer leakage inductance to be used for zero voltage switching.

The power stage design including the magnetic design and the open loop control circuit is described in chapter 5 and 6.

The bi-directional DC-DC converter has been implemented on a few PCB's and has been tested in both discharging mode and charging mode. The experimental results are presented in chapter 7. In discharging mode, for  $P_{in} = 1kW$  and a switching frequency  $F_s = 100kHz$ , the converter showed an efficiency of about 85% which is quite satisfactory. In order to explain the power losses, a power loss calculation has been carried out and is given in paragraph 7.2.3. The efficiency in charging mode of operation for  $P_{bat} = 100W$  is over 90%.

Keywords	
Bi-directional DC-DC converter	Fuel Cell system
Discharging mode	Phase shift control
Charging mode	Pulse width modulation
Front end DC-DC converter	UPS system

# Acknowledgements

I would like to express my appreciation and gratitude to the following people for their help in conducting the graduation project.

First of all, I wish to thank Prof. Dr. Ir. André Vandenput for allowing me to perform my graduation project in the EPE group.

I would also like to thank my supervisors Dr. Jorge Duarte and Ir. Marcel Hendrix for their calm and patience guidance during my graduation period to assist me to gain insight and experience in solving real engineering issues.

Furthermore, I would like to extend my appreciation to the EPE staff members and Phd. students for creating a pleasant work environment that is hard to forget. I would especially like to thank my colleague Redouane Eddeane for his friendship and inspirations. And special thanks goes to Marijn Uytdewilligen who was always willing to help me with practical issues during the design period.

Last but not least, I would like to thank my parents and my close friends for their support and inspirations during my studies.

Abdelhafid El Bouhali  
Tilburg, the Netherlands  
March 2005

# Contents

<b>1</b>	<b>Introduction</b>	<b>1</b>
1.1	Background information and motivation . . . . .	1
1.2	Fuel Cells . . . . .	3
1.3	Objective and outline . . . . .	6
1.4	Overview of the complete system . . . . .	8
<b>2</b>	<b>Front end DC-DC converter</b>	<b>9</b>
2.1	Introduction . . . . .	9
2.2	Principle of operation . . . . .	9
2.3	Converter analysis . . . . .	12
2.4	Simulation results . . . . .	15
<b>3</b>	<b>Numerical analysis of the ZVS FB DC-DC converter</b>	<b>19</b>
3.1	Introduction . . . . .	19
3.2	Key circuit waveforms . . . . .	21
3.3	Initial conditions . . . . .	25
3.4	Average output current in continuous conduction mode . . . . .	27
3.5	Average output current in discontinuous conduction mode . . . . .	29
<b>4</b>	<b>Bi-directional DC-DC converter</b>	<b>33</b>
4.1	Introduction . . . . .	33
4.2	Topology evaluation for Bi-directional DC-DC converter . . . . .	33
4.3	Discharging mode operation (Boost mode) . . . . .	35
4.3.1	Principle of operation . . . . .	35
4.3.2	Design of the energy storage capacitor $C_c$ : . . . . .	37
4.3.3	Voltage across the active clamp branch: . . . . .	38
4.3.4	Input inductor design . . . . .	39
4.4	Simulation results . . . . .	42
4.5	Charging mode operation (Buck mode) . . . . .	47
4.5.1	Charging mode operation without synchronous rectification . . . . .	47
4.5.2	Simulation results . . . . .	52
4.6	Charging mode operation with synchronous rectification . . . . .	55

<b>5 Power stage design</b>	<b>57</b>
5.1 Introduction . . . . .	57
5.2 Magnetic design . . . . .	57
5.2.1 Magnetic design using Magtool . . . . .	57
5.2.2 Transformer design using Magtool . . . . .	57
5.2.3 Inductor design using Magtool . . . . .	60
5.2.4 Inductor design . . . . .	61
5.3 Power component design . . . . .	63
5.3.1 Discharging mode . . . . .	63
5.3.2 Charging mode . . . . .	66
<b>6 Design of open loop control circuit</b>	<b>69</b>
6.1 Introduction . . . . .	69
6.2 Discharging mode . . . . .	69
6.2.1 Control signals . . . . .	69
6.2.2 Power Mosfet driver . . . . .	73
6.3 Charging mode . . . . .	79
6.3.1 Control signals . . . . .	79
6.3.2 Power Mosfet driver . . . . .	81
<b>7 Experimental results</b>	<b>83</b>
7.1 Introduction . . . . .	83
7.2 Discharging mode . . . . .	83
7.2.1 Experimental waveforms . . . . .	83
7.2.2 Efficiency evaluation . . . . .	90
7.2.3 Power loss calculation . . . . .	92
7.3 Charging mode . . . . .	99
7.3.1 Experimental waveforms . . . . .	99
<b>8 Conclusions and recommendations for future work</b>	<b>103</b>
8.1 Conclusions on bi-directional DC-DC converter . . . . .	103
8.2 Conclusions on bi-directional DC-DC converter in discharging mode . . . . .	104
8.3 Conclusions on bi-directional DC-DC converter in charging mode . . . . .	104
<b>A Matlab code: Derivation of system parameters</b>	<b>107</b>
<b>B Matlab code: DCM and CCM algorithm</b>	<b>109</b>
<b>C Magtool results: Transformer</b>	<b>111</b>
<b>D Magtool results: <math>L_1</math></b>	<b>115</b>
<b>E Magtool results: <math>L_2</math></b>	<b>121</b>

<b>F Magtool results: <math>L_k</math></b>	<b>127</b>
<b>G Power and control circuits discharging mode</b>	<b>133</b>
<b>H Power and control circuits charging mode</b>	<b>137</b>
<b>I Pcad Schematic: Discharging mode</b>	<b>141</b>
<b>J Pcad Schematic: Charging mode</b>	<b>144</b>
<b>K Measurement results @ 100kHz</b>	<b>147</b>
<b>L Measurement results @ 120kHz</b>	<b>148</b>
<b>M Measurement results @ 80kHz</b>	<b>149</b>
<b>N List of equipment used for test setup</b>	<b>150</b>

# List of Figures

1.1	Block diagram of Fuel Cell System . . . . .	1
1.2	Overview of the Fuel Cell Energy management system . . . . .	8
2.1	Conventional Full-Bridge PWM converter . . . . .	10
2.2	Phase Shifted Full-Bridge PWM converter . . . . .	11
2.3	Typical waveforms of the Phase Shifted FB-PWM Converter . . . . .	12
2.4	Simulation circuit of the Front End DC-DC converter . . . . .	15
2.5	Switching patterns of $S_1, S_3$ and $S_2, S_4$ . . . . .	16
2.6	1)Output voltage of the bridge 2)Input voltage of the transformer . . . . .	16
2.7	1)Leakage inductance current 2)Converter's output current 3)Load current 4)Output voltage across the load . . . . .	17
2.8	1)Voltage $V_{ds}$ across one switch of the converter 2)Current through one switch of the converter . . . . .	17
3.1	Bi-directional DC-DC converter in discharging mode . . . . .	19
3.2	FB ZVS DC-DC converter [3] . . . . .	20
3.3	Key waveforms of the ZVS FB DC-DC converter . . . . .	21
3.4	Electrical equivalent circuit of stage 3 . . . . .	22
3.5	Electrical equivalent circuit of stage 4 . . . . .	23
3.6	Electrical equivalent circuit of stage 6 . . . . .	23
3.7	Average output current of the converter in CCM . . . . .	27
3.8	Converter operating in DCM during stage 3 . . . . .	29
3.9	Converter operating in DCM during stage 8 . . . . .	29
3.10	Average output current of the converter in DCM . . . . .	30
3.11	Relation between average output current and the DC conversion ratio as function of the duty cycle . . . . .	32
4.1	Low-side full-bridge current-fed with active clamp and high-side full-bridge voltage-fed converter . . . . .	34
4.2	Bi-directional DC-DC converter in discharging mode . . . . .	35
4.3	Typical waveforms of the Bi-directional DC-DC converter in discharging mode	36
4.4	Bi-directional DC-DC converter with the corresponding currents and voltages	36
4.5	Bi-directional DC-DC converter in discharging mode with modification of input inductor . . . . .	39

4.6	Design configuration $L_2$	40
4.7	Illustration of current ripple	40
4.8	Design configuration $L_1$	40
4.9	Simulation circuit of the Bi-directional DC-DC converter in discharging mode	42
4.10	Switching patterns of the MOSFET's	43
4.11	1) Output voltage of the bridge 2) Input voltage of the transformer	43
4.12	1) Voltage across the clamp capacitor 2) Current through the clamp capacitor	44
4.13	1) Voltage across $S_c$ 2) Current through $S_c$	44
4.14	1) Leakage inductance current 2) Average output current	45
4.15	1) Voltage across $S_1$ 2) Current through $S_1$	45
4.16	1) Load current 2) Load voltage	46
4.17	Bi-directional DC-DC converter in charging mode	47
4.18	Bi-directional DC-DC converter in charging mode with corresponding currents and voltages	48
4.19	Typical waveforms of the Bi-directional DC-DC converter	48
4.20	Simulation circuit of the Bi-directional DC-DC converter in charging mode	52
4.21	Switching patterns of the switches	53
4.22	1) Output voltage of converter bridge 2) Voltage across secondary side of transformer	53
4.23	1) Leakage inductance current 2) Current through output inductor 3) Charging current to battery 4) Battery voltage 5) Current through active clamp capacitor	54
4.24	1) Voltage ( $V_{ds}$ ) across $S_5$ 2) Current through $S_5$	54
4.25	Typical waveforms of the converter with synchronous rectification	56
5.1	Current through primary side of transformer	58
5.2	Current through $L_1$ , $L_2$ respectively	61
5.3	Current through $L_k$	61
5.4	Power stage component selection	63
5.5	Power stage component selection	66
6.1	Circuit used for implementing PWM signals	70
6.2	<b>Ch1:</b> $S_a$ 10V/div. <b>Ch2:</b> $S_b$ 10V/div.	70
6.3	Control circuit of $S_c$ including deadtime circuit	71
6.4	<b>Ch1:</b> $S_c$ 10V/div.	72
6.5	Mosfet driver circuit of $S_1$ and $S_2$	73
6.6	Mosfet driver circuit of $S_3$ and $S_4$	73
6.7	Mosfet driver of $S_c$	77
6.8	<b>Ch1:</b> $V_{gs}$ of $S_1$ , $S_2$ 10V/div <b>Ch2:</b> $V_{gs}$ of $S_2$ , $S_4$ 10V/div <b>Ch3:</b> $V_{gs}$ of $S_c$ 10V/div	78
6.9	<b>Ch1:</b> $V_{gs}$ of $S_1$ , $S_2$ 10V/div <b>Ch2:</b> $V_{gs}$ of $S_2$ , $S_4$ 10V/div <b>Ch3:</b> $V_{gs}$ of $S_c$ 10V/div	78
6.10	Phase shift control of converter leg 1	79

6.11	Phase shift control of converter leg 2 . . . . .	79
6.12	Signal waveforms of phaseshift generator . . . . .	80
6.13	Mosfet driver circuit of $S_5$ and $S_7$ . . . . .	81
6.14	Mosfet driver circuit of $S_8$ and $S_6$ . . . . .	81
6.15	Control signals of one converter leg with dead time; <b>Ch2:</b> $V_{gs}$ of $S_5$ 10V/div, <b>Ch3:</b> $V_{gs}$ of $S_7$ 10V/div . . . . .	82
6.16	Phase shifted signals of the converter; <b>Ch2:</b> $V_{gs}$ of $S_5$ 10V/div, <b>Ch3:</b> $V_{gs}$ of $S_8$ 10V/div . . . . .	82
7.1	Converter in discharging mode with test points . . . . .	83
7.2	<b>Ch1:</b> $V_{bridge}$ ( $V_{AB}$ ) 50V/div., <b>Ch2:</b> $V_{gs}$ of $S_1$ 10V/div., <b>Ch3:</b> $V_{gs}$ of $S_c$ 10V/div . . . . .	84
7.3	<b>Ch1:</b> $V_{bridge}$ ( $V_{AB}$ ) 50V/div. . . . .	84
7.4	<b>Ch2:</b> $V_{gs}$ of $S_4$ 10V/div., <b>Ch3:</b> $V_{ds}$ of $S_4$ 20V/div. . . . .	85
7.5	<b>Ch2:</b> $V_{gs}$ of $S_4$ 10V/div., <b>Ch3:</b> $V_{ds}$ of $S_4$ 20V/div. for $P_{in} = 1kW$ . . . . .	85
7.6	<b>Ch1:</b> $V_{bridge}$ ( $V_{AB}$ ) 40V/div., <b>Ch2:</b> $V_{gs}$ of $S_c$ 10V/div., <b>Ch3:</b> $I_{cc}$ 10A/div. . . . .	86
7.7	<b>Ch1:</b> $V_{bridge}$ ( $V_{AB}$ ) 40V/div., <b>Ch2:</b> $V_{ds}$ of $S_1$ 40V/div., <b>Ch4:</b> $I_{s1}$ 10A/div. . . . .	86
7.8	<b>Ch2:</b> $V_{ds}$ of $S_1$ 40V/div., <b>Ch4:</b> $I_{s1}$ 25A/div. . . . .	87
7.9	<b>Ch1:</b> $V_{bridge}$ ( $V_{AB}$ ) 40V/div., <b>Ch2:</b> $V_{out}$ 400V/div., <b>Ch3:</b> $V_{cc}$ 25V/div., <b>Ch4:</b> $I_{Lk}$ 25A/div. . . . .	88
7.10	<b>Ch1:</b> $V_{bridge}$ ( $V_{AB}$ ) 40V/div., <b>Ch2:</b> $V_{secondair}$ ( $V_{CD}$ ) 400V/div., <b>Ch4:</b> $I_{out}$ 5A/div. . . . .	88
7.11	<b>Ch1:</b> $V_{bridge}$ ( $V_{AB}$ ) 100V/div., <b>Ch4:</b> $I_{Lk}$ 25A/div. for $P_{in} = 1kW$ . . . . .	89
7.12	<b>Ch1:</b> $V_{bridge}$ ( $V_{AB}$ ) 100V/div., <b>Ch4:</b> $I_{out}$ 5A/div. for $P_{in} = 1kW$ . . . . .	89
7.13	Photograph of converter . . . . .	90
7.14	Efficiency profile for different switching frequencies . . . . .	91
7.15	Photograph of test setup . . . . .	92
7.16	Illustration of test setup . . . . .	93
7.17	Active clamp branch . . . . .	94
7.18	Diode . . . . .	97
7.19	Photograph of converter in charging mode . . . . .	99
7.20	Converter in charging mode with test points . . . . .	100
7.21	<b>Ch2:</b> $V_{gs}$ of $S_8$ , 10V/div., <b>Ch3:</b> $V_{gs}$ of $S_5$ , 10V/div. . . . .	100
7.22	<b>Ch2:</b> $V_{gs}$ of $S_5$ , 10V/div., <b>Ch3:</b> $V_{gs}$ of $S_7$ , 10V/div. . . . .	101
7.23	<b>Ch1:</b> $V_{bridge}$ ( $V_{AB}$ ), 400V/div., <b>Ch2:</b> $V_{gs}$ of $S_5$ , 10V/div., <b>Ch3:</b> $V_{gs}$ of $S_7$ , 10V/div. . . . .	101
7.24	<b>Ch2:</b> $V_{bat}$ , 20V/div., <b>Ch4:</b> $I_{bat}$ , 1.5A/div. . . . .	102
G.1	Circuit used for implementing PWM signals . . . . .	133
G.2	Control circuit of $S_c$ including deadtime circuit . . . . .	134
G.3	Mosfet driver circuit of $S_1$ and $S_2$ . . . . .	134
G.4	Mosfet driver circuit of $S_3$ and $S_4$ . . . . .	135
G.5	Mosfet driver of $S_c$ . . . . .	135

G.6	Power stage component selection	136
H.1	Phase shift control of converter leg 1	137
H.2	Phase shift control of converter leg 2	137
H.3	Mosfet driver circuit of $S_5$ and $S_7$	138
H.4	Mosfet driver circuit of $S_8$ and $S_6$	138
H.5	Power stage component selection	139
I.1	Pcad schematic of discharging mode part 1	142
I.2	Pcad schematic of discharging mode part 2	143
J.1	Pcad schematic of charging mode part 1	145
J.2	Pcad schematic of charging mode part 2	146

# List of Tables

1.1	Type of Fuel Cells and their applications [1]	4
2.1	System parameters of the Front End DC-DC Converter	15
4.1	System parameters of the Bi-directional DC-DC Converter	42
4.2	System parameters for the simulation	52
5.1	Design parameters transformer core	59
5.2	Magtool design results of transformer	59
5.3	Design parameters for the inductor's cores	62
5.4	Magtool design results of inductors	62
5.5	System parameters in discharging mode	63
5.6	Voltage and current ratings of the selected power switches	65
5.7	System parameters in charging mode	66
5.8	Voltage and current ratings of the selected power switches	67
7.1	Measurement results of converter in discharging mode at $F_s = 100kHz$ with varying load	91
7.2	Power dissipation in the devices used	98
K.1	Measurement results of converter in discharging mode at $F_s = 100kHz$	147
L.1	Measurement results of converter in discharging mode at $F_s = 120kHz$	148
M.1	Measurement results of converter in discharging mode at $F_s = 80kHz$	149
N.1	List of equipment for converter in discharging mode	150
N.2	List of equipment for converter in charging mode	151

# Chapter 1

## Introduction

### 1.1 Background information and motivation

Nowadays the environmental concern is the driving force for alternative energy. Therefore, new sustainable energy sources are gaining more and more acceptance in the industrial world.

One of these sources has recently been revived and shows promising results for applications as small as cellular phones to as large as utility power generations. This sustainable energy source is the hydrogen fuel cell. One particular application for medium power fuel cell systems is distributed power generation. Distributed power will allow the utility company to locate small energy saving units closer to the customer. It may even involve stand alone systems for residential use. A block diagram of a fuel cell system used for stand-alone applications or utility connect is shown in figure 1.1.

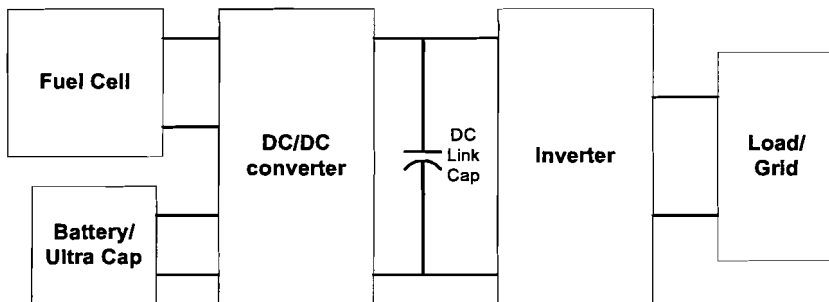


Figure 1.1: Block diagram of Fuel Cell System

Fuel cell power generation systems are expected to see increasing practical use due to the several advantages over conventional generation systems. These advantages include:

- Low environmental pollution
- Highly efficient power generation
- Diversity of fuels such as gas, LPG, methanol and naphtha
- Reusability of exhaust heat
- Modularity and faster installation

Fuel cells are electrochemical devices that convert chemical energy of fuel to electrical energy without combustion. In most of the cases, fuel cells convert the energy from a hydrogen-rich fuel directly into electricity and operate as long as fuel and oxygen are supplied to the cell.

Fuel cells produce direct current (DC) power and need to be electrically connected in stacks to obtain the desired voltage.

## 1.2 Fuel Cells

As mentioned earlier, the Fuel Cell is an electrochemical device that combines hydrogen fuel with oxygen producing electric power, heat and water. In many ways, the Fuel Cell resembles a battery. Rather than applying a periodic recharge, a continuous supply of oxygen and hydrogen is supplied from the outside. Oxygen is drawn from the air, and hydrogen is carried as a fuel in a pressurized container. As alternative fuel, methanol, propane, butane and natural gas can be used. [1]

The Fuel Cell is twice as efficient as combustion. Hydrogen, the simplest element, is an exceptionally clean fuel. It makes up 90% of the composition of the universe and is the third most abundant element on the earth's surface. Such a wealth of fuel would provide an almost unlimited pool of energy at relatively low cost. But there is a price to pay. The Fuel Cell core (or stack), which converts oxygen and hydrogen to electricity, is expensive to build and maintain.

Hydrogen must be carried in a pressurized bottle. If propane, natural gas or diesel is used, a reformer is needed that will convert the fuel to hydrogen. Reformers for proton exchange membranes (the heart of the Fuel Cell, also called polymer electrolyte membranes) are bulky and expensive. They start slowly, and purification is required. Often the hydrogen is delivered at low pressure, and additional compression is required. Some fuel efficiency is lost, and a certain amount of pollution is produced.

A Fuel Cell is electrolysis in reverse, using two electrodes separated by an electrolyte. Hydrogen is presented to the negative electrode (anode) and oxygen to the positive electrode (cathode). A catalyst at the anode separates the hydrogen into positively charged hydrogen ions and electrons. In the PEM system, the oxygen is ionized and migrates across the electrolyte to the anodic compartment where it combines with hydrogen. The byproduct is electricity, some heat and water. A single Fuel Cell produces 0.6V to 0.8V under load. Several cells are connected in series to obtain higher voltages.

### Type of Fuel Cells

Several variations of Fuel Cell systems have emerged. There is the previously mentioned and most widely developed PEM system, using a polymer electrolyte. This system is mostly used for vehicles and portable electronics. Several developers are also targeting stationary applications. The alkaline system, which uses a liquid electrolyte, is the preferred Fuel Cell for aerospace applications, including the space shuttle.

The molten carbonate, the phosphoric acid and the solid oxide Fuel Cell are reserved for stationary applications, such as power generating plants for electric utilities. Among these stationary systems, the solid oxide is the least developed but has received renewed attention due to breakthroughs in cell material and stack designs. Table 1.1 below compares the most common Fuel Cell systems in development.

Type of Fuel Cell	Applications	Advantages	Limitations	Status
<i>Proton Exchange Membrane (PEMFC)</i>	Mobile (buses, cars,) portable power, medium to large-scale stationary power generation (homes, industry).	Compact design; long operating life; adapted by major automakers; offers quick start-up, low temperature operation, operates at 50% efficiency (25%-35% in system).	High manufacturing costs, needs heavy auxiliary equipment and pure hydrogen, no tolerance for contaminates; complex heat and water management	Most widely developed, production; offers promising technology.
<i>Alkaline (AFC)</i>	Space (NASA), terrestrial transport (German submarines).	Low manufacturing and operation costs; does not need heavy compressor, fast cathode kinetics.	Large size; needs pure hydrogen and oxygen, use of corrosive liquid electrolyte.	First-generation technology.
<i>Molten Carbonate (MCFC)</i>	Large-scale power generation.	Highly efficient; uses heat to run turbines for co-generation.	Electrolyte instability; limited service life.	Well-developed; semi-commercial.
<i>Phosphoric Acid (PAFC)</i>	Medium to large-scale power generation.	Commercially available; lenient to fuels; uses heat for co-generation.	Low efficiency, limited service life, expensive catalyst.	Mature but faces competition from PEMFC.
<i>Solid Oxide (SOFC)</i>	Medium to large-scale power generation.	High efficiency, lenient to fuels, takes a natural gas directly, no reformer needed. Operates at 60 per cent efficiency; uses heat for co-generation.	High operating temperature; requires exotic metals, high manufacturing costs, oxidation issues; low specific power.	Least developed. Breakthroughs in cell material and stack design sets off new research.
<i>Direct Methanol (DMFC)</i>	Suitable for portable, mobile and stationary applications.	Compact design, no compress or humidification needed; feeds directly off methanol.	Complex stack structure, slow load response times; operates at 20% efficiency.	Laboratory prototypes.

Table 1.1: Type of Fuel Cells and their applications [1]

The PEM system allows compact designs and achieves a high energy-to-weight ratio. The limitations of the PEM system are high manufacturing costs and complex water management issues. The stack contains hydrogen, oxygen and water. If dry, the input resistance is high and water must be added to get the system going. Too much water causes flooding.

The PEM Fuel Cell also has a limited temperature range. Freezing water can damage the stack. Heating elements are needed to keep the stack within an acceptable temperature range because freezing water can cause damage. The warm-up is slow, and the performance is poor when cold. Heat is also a concern if the temperature rises too high.

The PEM Fuel Cell requires pure hydrogen with little tolerance for contaminants, such as sulfur compounds or carbon monoxide. Carbon monoxide can poison the system. Decomposition of the membrane takes place if different grade fuels are used.

To reduce the internal resistance of the stack, the membrane is made thin. Over time, pinholes can develop in the membrane, which cause a crossover of hydrogen. Once present, the pinholes grow in size and eventually lead to a cell failure due to electrical shorting. Testing and repairing a stack are difficult. The complexity to service a Fuel Cell becomes apparent when considering that a typical 150V, 50kW stack has about 250 cells.

### **Applications**

A Fuel Cell for portable applications would not necessarily replace the battery in the equipment but could serve as a charger that is carried separately. The feasibility to build a mass-produced Fuel Cell that fits into the form factor of a battery is still a few years away.

The advantages of the portable Fuel Cell are: high energy density (as much as five times that of a battery); environmental cleanliness, fast recharge and long runtime. In fact, continuous operation is feasible.

### **Advantages and limitations**

Ironically, the Fuel Cell will not eliminate the chemical battery but will promote it. The Fuel Cell needs batteries as a buffer. For many applications, a battery bank will provide momentary high current loads and the Fuel Cell will keep the battery fully charged. For portable applications, a super capacitor or a battery will improve the loading characteristics and enable high current pulses.

## 1.3 Objective and outline

The M.Sc. project makes part of a larger research project that concerns the applications of Fuel-cell-based Uninterruptible Power Supply (UPS) systems. A UPS system should provide uninterrupted, reliable, and high quality power for vital loads. Applications of UPS systems include medical facilities, data storage and computer systems, emergency equipment, telecommunications, and on-line management systems.

As is well-known PEM Fuel Cells have a delay as much as several tens of seconds and they cannot immediately take over the full load in case of a power failure. For this reason another storage element, such as a battery, should compensate for these response delays by supplying the required instantaneous energy, which is stored during the normal operation.

Another drawback of a PEM Fuel Cell is its slow response, with the result that power demand from the load and power supply from the Fuel Cell does not coincide during transient load condition. Therefore, the secondary energy source is required to match the power difference between the Fuel Cell and the load.

The focus of my study was to design and build a 1kW bi-directional DC-DC converter for a Fuel Cell energy management system. Furthermore the study of a front end DC-DC converter, which is needed to convert the Fuel Cell voltage to a higher output voltage, should be carried out.

This report presents the results of my graduation assignment, which consists of the following parts:

1. A literature research on front end DC-DC converter for a Fuel Cell energy management system with the corresponding simulation results of a 1kW front end DC-DC converter.
2. Topology evaluation of a bi-directional DC-DC converter.
3. The design and implementation of a 1kW bi-directional DC-DC converter

This report is structured as follows:

### **Chapter 2:**

Description of the working and simulation of the front end DC-DC converter.

### **Chapter 3:**

Presentation of a numerical analysis of the ZVS full bridge DC-DC converter.

### **Chapter 4:**

Description of the working and simulation of the bi-directional DC-DC converter in discharging and charging mode operation.

**Chapter 5:**

Description and implementation of the power stage design.

**Chapter 6:**

Implementation of the open loop control of the bi-directional DC-DC converter.

**Chapter 7:**

Presentation of the experimental results.

**Chapter 8:**

Conclusions of the graduation assignment and recommendations for future work.

## 1.4 Overview of the complete system

Figure 1.2 shows an overview of the complete Fuel Cell energy management system. In general, the function of a power conditioning system in a Fuel Cell generation system is to convert the DC output power from the Fuel Cell to a regulated DC or AC power. There might be several stages of power converters.

A DC-DC converter converts the low voltage DC output from the Fuel Cell to a level at which an inverter can safely operate. If AC power is required an inverter should be used to invert the DC output from the DC-DC converter to a suitable AC voltage.

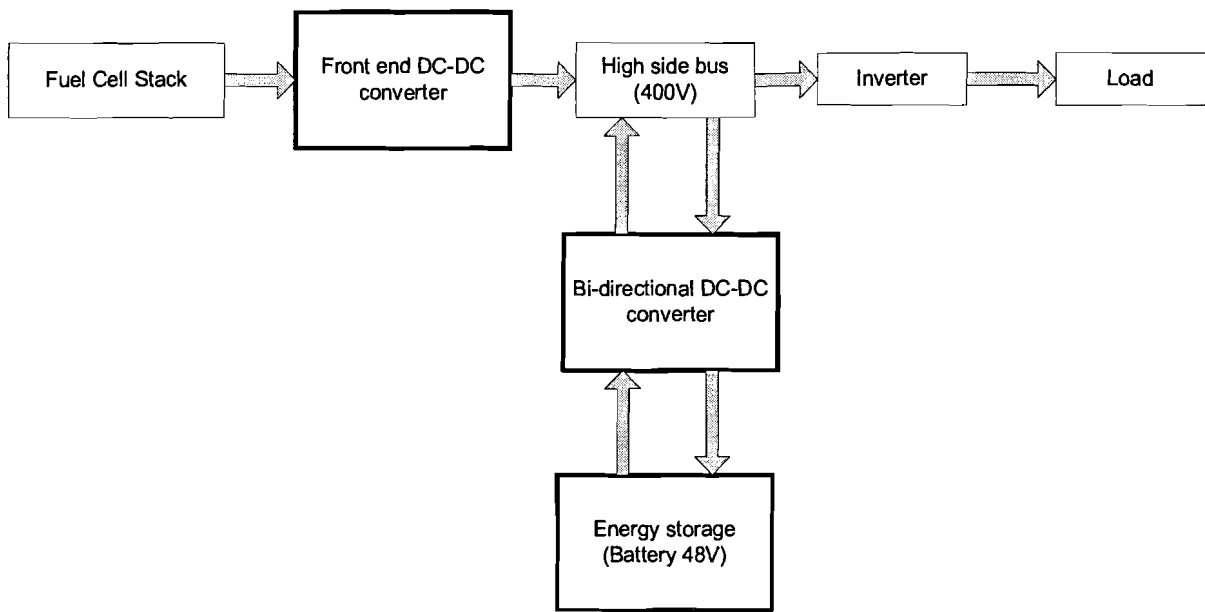


Figure 1.2: Overview of the Fuel Cell Energy management system

As can be seen in figure 1.2, in steady state operation the output voltage of the Fuel Cell ( $25V - 40V$ ) is boosted to the high side bus which operates on a voltage of  $400V$ . The power requirement for the front end DC-DC converter during normal operation is  $1kW$ .

Furthermore, the bi-directional DC-DC converter has two purposes. The first one is to boost DC power from the  $48V$  battery to  $400V$  on the isolated high voltage DC bus during the Fuel-Cell start up process. After the start up process, the Fuel Cell output feeds the high voltage bus. The power requirement for the bi-directional DC-DC converter during start up is to provide  $1kW$  DC power.

After the Fuel Cell voltage builds up and is able to provide  $1kW$  DC power, the bi-directional DC-DC converter should switch to another operation mode which is called charging mode. In this mode, the bi-directional DC-DC converter works as a battery charger and delivers power from the high voltage bus to the  $48V$  bus to charge the battery. The power requirement for the charging mode is about 10% of full power, namely  $100W$ .

# Chapter 2

## Front end DC-DC converter

### 2.1 Introduction

This chapter discusses the front end DC-DC converter. After a topology evaluation and literature research the phase-shifted front end DC-DC converter has been simulated and will be presented in this section.

### 2.2 Principle of operation

The front end DC-DC converter is required to boost the Fuel Cell voltage to a desired higher output voltage. After literature review it can be concluded that two main topologies are widely used:

- The conventional full bridge PWM converter
- The phase shifted full bridge PWM converter

In order to reduce the size and weight of magnetic components it is desirable to increase the switching frequency for DC-DC converters. However, when conventional PWM converters operate at high frequencies, the circuit parasitics have negative effects on the converter performance.

In high power applications switching losses increase which means that snubbers and/or other means of protection are required. The use of snubbers and/or other means of protection introduce significant losses and lower the efficiency.

In the case of the conventional full bridge converter, the diagonally opposite switches, namely  $Q_1$  and  $Q_2$  or  $Q_3$  and  $Q_4$ , are turned on and off simultaneously as depicted in figure 2.1. When all four switches are turned off, the load current freewheels through the rectifier diodes. The energy that is stored in the leakage inductance of the power transformer then causes severe ringing with the MOSFET junction capacitances. This creates the need for using snubbers that increase the overall losses bringing down the converter efficiency.

If snubbers are not used, the selection of the devices becomes more difficult as the voltage rating for these switches has to be much higher. As the voltage rating goes up, the conduction losses increase as well and as a result the cost and the overall losses of the converter increase.

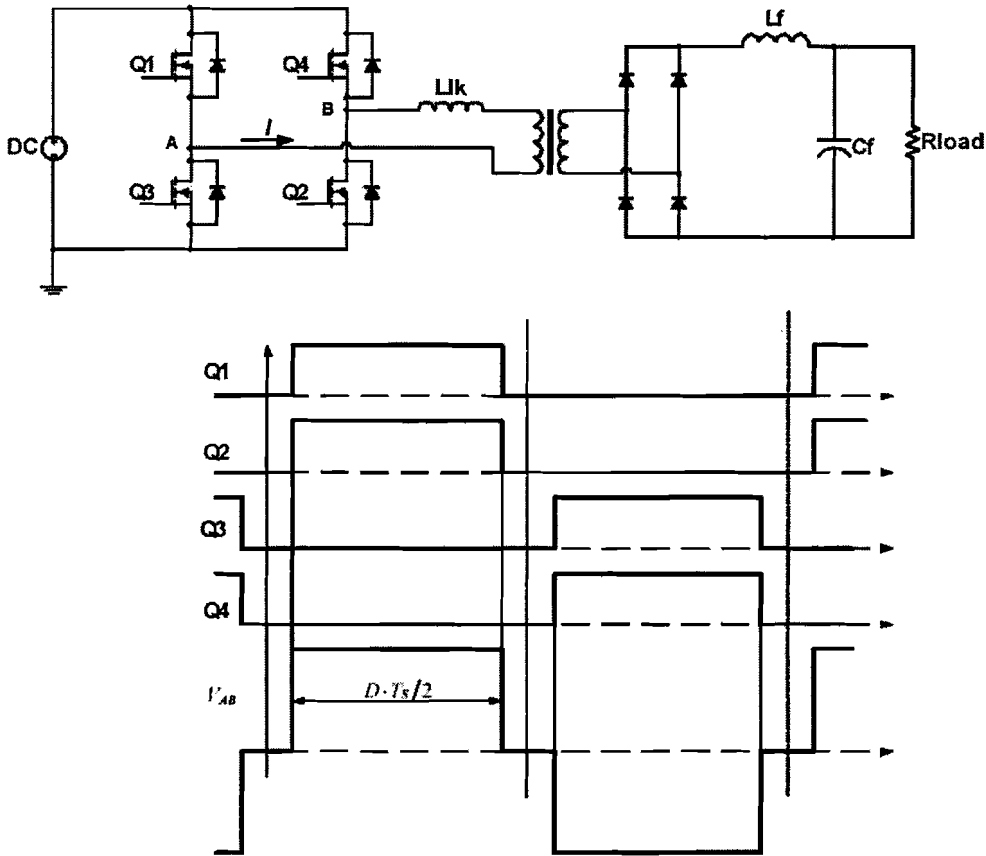


Figure 2.1: Conventional Full-Bridge PWM converter

In order to minimize the parasitic ringing, the gate signals of  $Q_2$  and  $Q_4$  are delayed (phase-shifted) with respect to those of  $Q_1$  and  $Q_3$ , as shown in figure 2.2. This means that the primary side of the transformer is either connected to the input voltage or short circuited. The leakage inductance current is never interrupted, thus solving the problem of parasitic ringing associated with the conventional full-bridge PWM converter.

The energy that is stored in the leakage inductance can be used to discharge the energy stored in the MOSFET junction capacitances to achieve zero voltage switching (ZVS) conditions for all four switches in the primary side. In this case, the converter requires no additional resonant components.

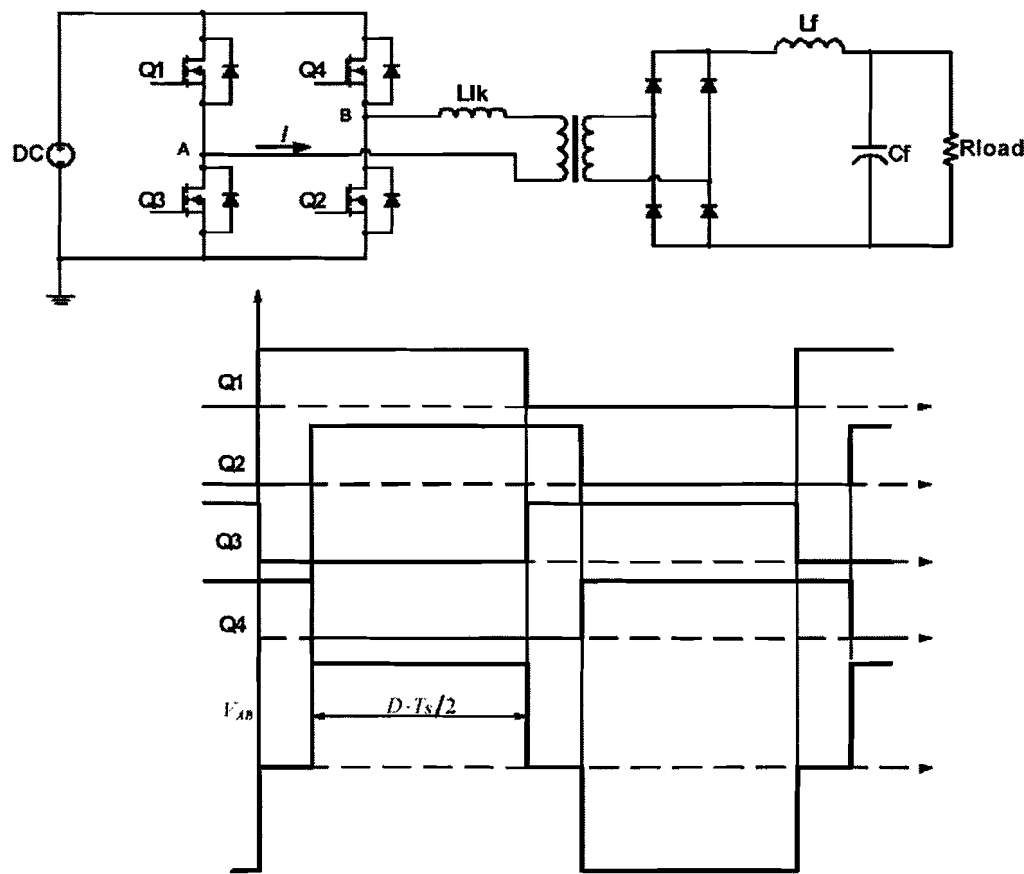


Figure 2.2: Phase Shifted Full-Bridge PWM converter

## 2.3 Converter analysis

The typical waveforms of the phase shifted full bridge converter are depicted in figure 2.3. From the inductor voltage  $V_{Lf}$  the following equation can be written as follows:

$$\left( V_{in} \frac{N_s}{N_p} - V_{Load} \right) \frac{DT_s}{2} = V_{Load} \left( \frac{T_s(1-D)}{2} \right) \quad (2.1)$$

Then, the duty cycle of the phase shifted front-end DC-DC converter can be defined as follows:

$$D = \frac{N_p V_{Load}}{N_s V_{in}} \quad (2.2)$$

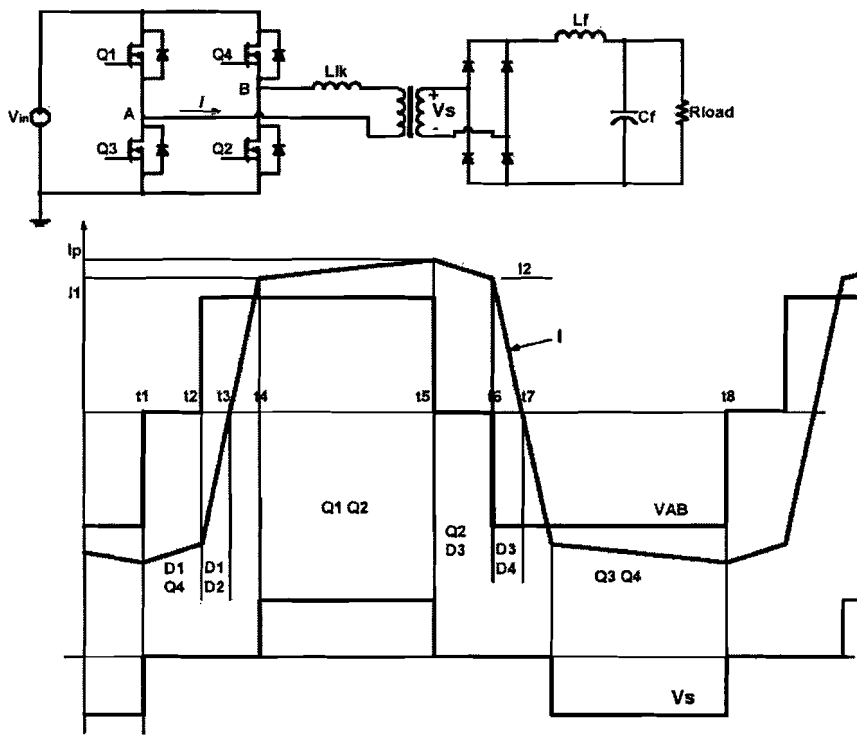


Figure 2.3: Typical waveforms of the Phase Shifted FB-PWM Converter

The front-end FB-ZVS-PWM converter provides ZVS for all four switches in the bridge. However, the mechanism by which ZVS is achieved is different for both legs of the bridge.

The ZVS for transistors Q2 and Q4 is provided by the resonance between the leakage inductance,  $L_{lk}$  and the output capacitance of the switch. The required energy for achieving ZVS is given by:

$$E = \frac{1}{2}L_{lk}I_2^2 \geq \frac{4}{3}C_{mos}V_{in}^2 + \frac{1}{2}C_{TR}V_{in}^2 \quad (2.3)$$

Where:  $I_2$  is the current through the primary side when  $Q_2$  turns off,  $V_{in}$  is the input voltage and  $C_{TR}$  is the transformer winding capacitance.

The factor 4/3 in equation 2.3 is two times the energy stored in the nonlinear drain to source capacitor, whose capacitance is inversely proportional to the square root of the voltage [2].

The resonance between  $L_{lk}$ ,  $C_{mos}$  and  $C_{TR}$  provides a sinusoidal voltage across the capacitances reaching a maximum at one fourth of the resonant frequency period.

The dead time between  $Q_2$  and  $Q_4$  has to be set at  $\delta t_{max}$  to ensure that there is sufficient time to charge and discharge the capacitances. The dead time that is required to ensure ZVS with the maximum possible load range can be determined by the following equation [2]:

$$\delta t_{max} = \frac{T}{4} = \frac{\pi}{2}\sqrt{L_{lk}C} \quad (2.4)$$

Where:  $C = C_{mos} + C_{TR}$

Whether ZVS can be achieved for  $Q_2$  and  $Q_4$  is dependent on the load level of the converter. For light loads, the current through  $L_{lk}$  when  $Q_2$  and  $Q_4$  are turned off may not be enough to turn on the anti-parallel diode.

For switches  $Q_1$  and  $Q_3$ , ZVS is provided by a different mechanism. Before  $Q_1$  is turned off, the current in the primary side is reaching its peak value. The primary current is the filter inductor current reflected to the primary side. When  $Q_1$  is turned off, the energy that is available to charge the output capacitance of  $Q_1$  and to discharge the output capacitance of  $Q_3$  is the energy stored in  $L_{lk}$  and the energy in the output filter inductor. This energy in the output filter inductor is available because the filter inductor current does not freewheel through the rectifier until the voltage across the secondary side has fallen to zero.

Since the energy in the filter inductor is large compared to the energy stored in the switch capacitances on the primary side, the charging of the switches can be approximated by a linear charging with a constant current. That means that the dead time  $dt$  required between the turn off of  $Q_1$  and turn on of  $Q_3$  can be determined from the following equation:

$$dtI_p = 4C_{mos}V_{in} \quad (2.5)$$

Where  $4C_{mos}V_{in}$  corresponds to twice the charge stored in the nonlinear output capacitance of the MOSFET and  $I_p$  is the peak current in the output filter inductor reflected to the primary. The dead time can be calculated for the minimum  $I_p$  chosen to achieve ZVS.

The ZVS for  $Q1$  and  $Q3$  can even be achieved at light loads because  $D1$  and  $D3$  can always be turned on by the energy stored in the output filter inductance. However, ZVS for  $Q2$  and  $Q4$  can only be achieved for a load current above the critical value that is given by the following expression:

$$I_{crit} = \sqrt{\frac{2}{L_{lk}} \left( \frac{4}{3}C_{mos}V_{in}^2 + \frac{1}{2}C_{TR}V_{in}^2 \right)} \quad (2.6)$$

## 2.4 Simulation results

The simulation circuit of the front end dc-dc converter that is implemented in PSIM is depicted in Figure 2.4. It consists of a full bridge dc-dc converter with the corresponding duty cycle and dead time control. The switching patterns of the four switches are shown in figure 2.5. The switching process is performed with a duty cycle of 50%, whereas the phase shift can be regulated.

The front end DC-DC converter has been simulated according to the following system parameters:

DC link power	$P_{dc} = 1kW$
Switching frequency	$F_s = 150kHz$
Input voltage (Fuel Cell)	$V_{FC} = 25 - 40V$
DC link voltage	$V_{dc} = 400V$
Transformer turns ratio	$N_p : N_s = 1 : 30$

Table 2.1: System parameters of the Front End DC-DC Converter

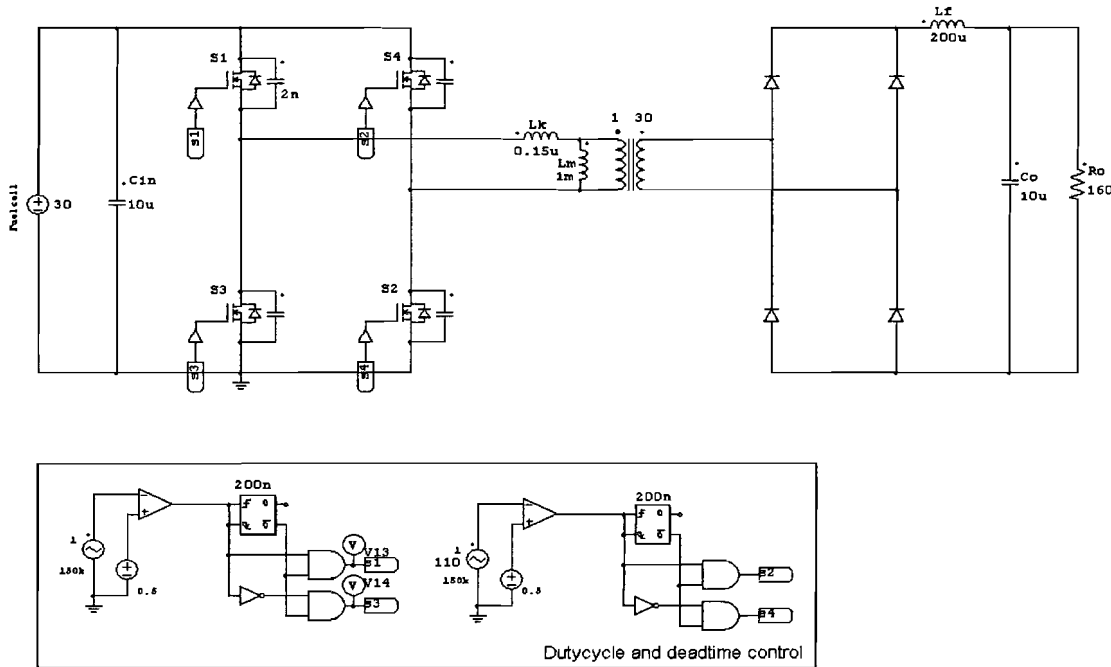


Figure 2.4: Simulation circuit of the Front End DC-DC converter

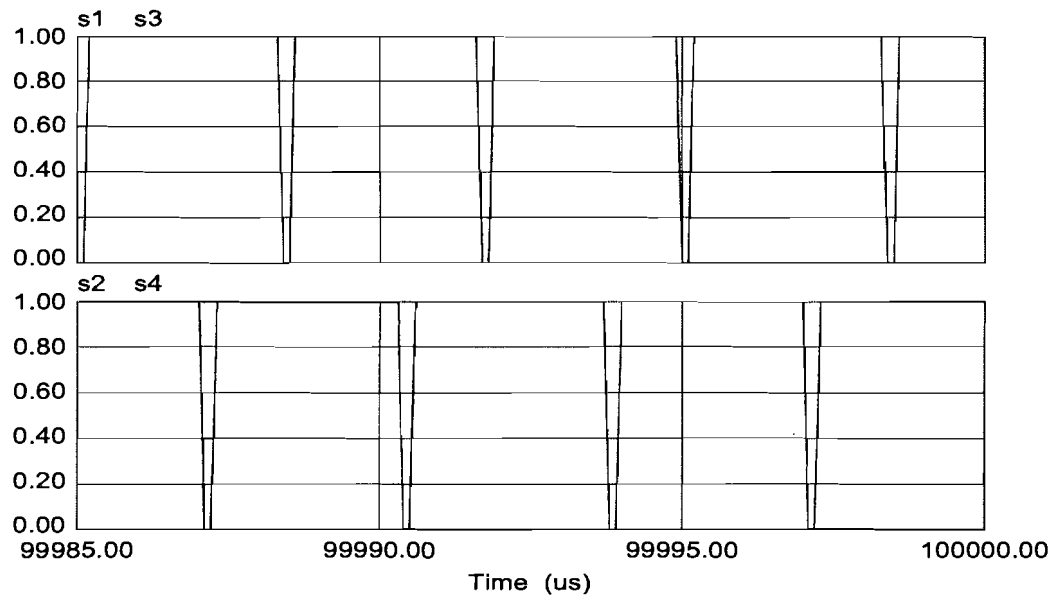


Figure 2.5: Switching patterns of  $S_1, S_3$  and  $S_2, S_4$

The output voltage of the converter bridge and the input voltage of the transformer are depicted in figure 2.6.

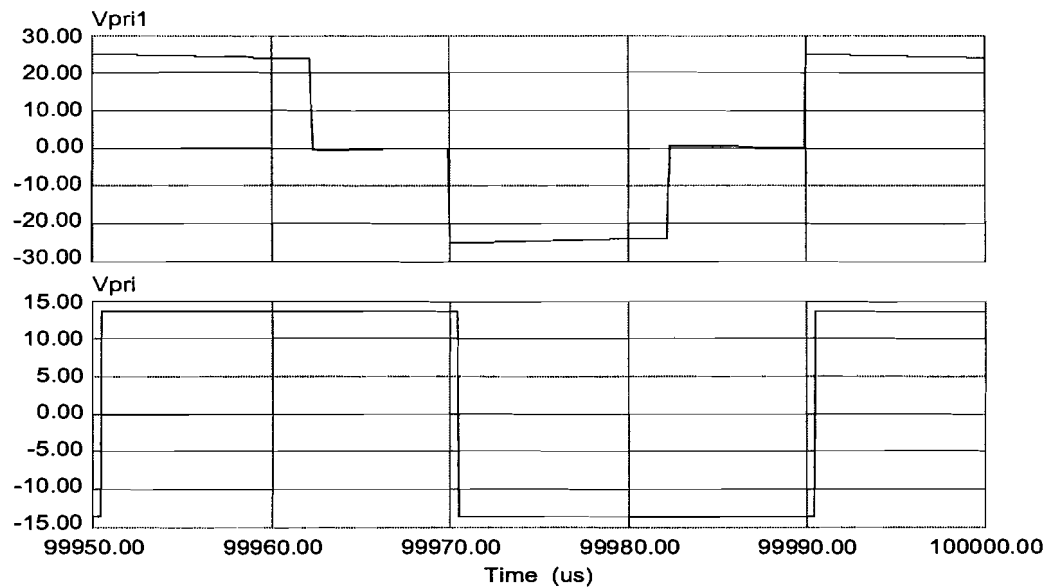


Figure 2.6: 1)Output voltage of the bridge 2)Input voltage of the transformer

Figure 2.7 shows the typical waveforms of the converter. As can be seen, the output power of the front end DC-DC converter is about 1kW.

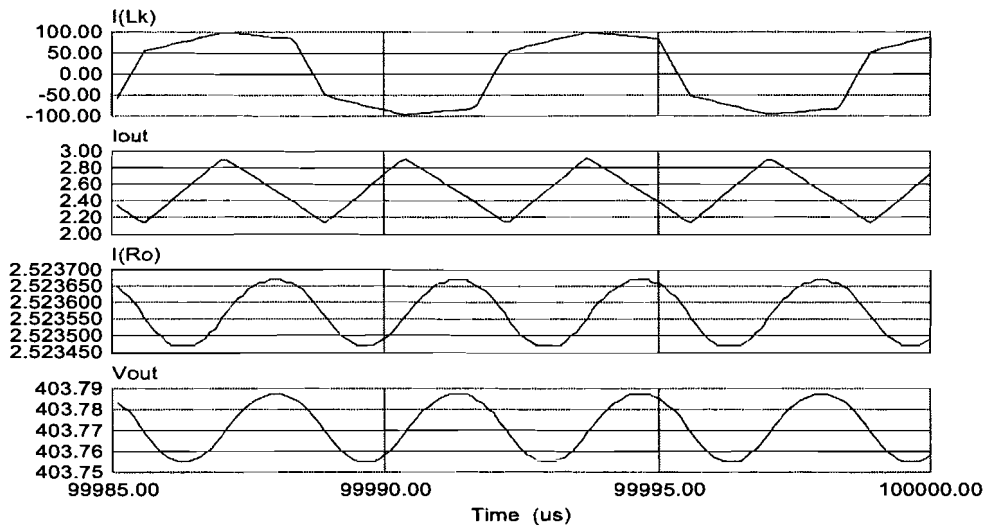


Figure 2.7: 1)Leakage inductance current 2)Converter's output current 3)Load current 4)Output voltage across the load

Figure 2.8 shows the voltage ( $V_{ds}$ ) across one switch and the current through one switch of a converter leg. The same waveforms apply to the remaining switches of the converter with the distinction that they are phase shifted.

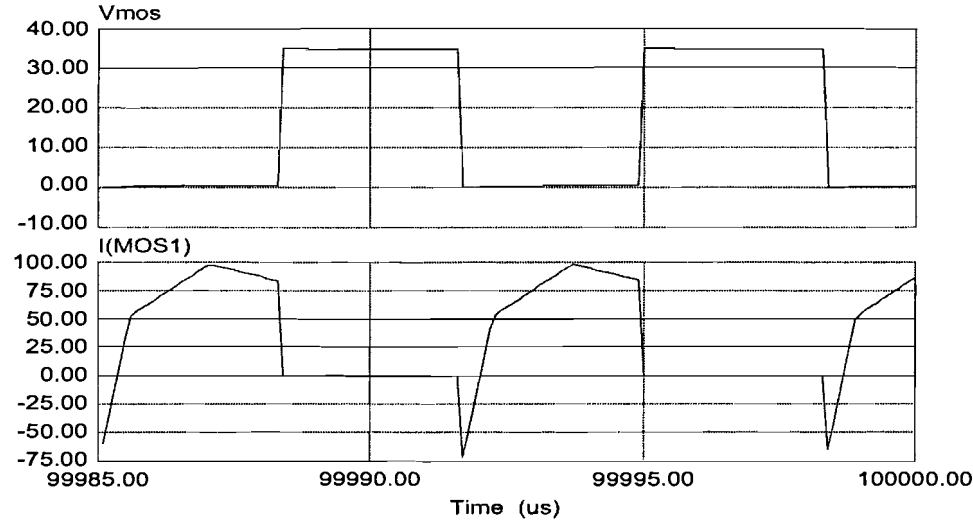


Figure 2.8: 1)Voltage  $V_{ds}$  across one switch of the converter 2)Current through one switch of the converter

# Chapter 3

## Numerical analysis of the ZVS FB DC-DC converter

### 3.1 Introduction

This chapter describes a numerical analysis of the full bridge DC-DC converter that can be used to determine the circuit parameters of the bi-directional DC-DC converter. In order to calculate the required circuit parameters for achieving the desired output power, the full bridge ZVS DC-DC converter in figure 3.1 is considered.

The analysis has been made for a ZVS FB DC-DC converter, however it should be mentioned that the same derivation can be used in the case of a front end DC-DC converter and a bi-directional DC-DC converter with some little adjustments. In case of the bi-directional DC-DC converter in discharging mode that is depicted in figure 3.2, it should be noticed that the same analysis can be made when considering the voltage across the active clamp capacitor  $C_c$  being equal to the input voltage  $V_i$  in figure 3.1. This assumption can be made because  $V_{cc}$  is quite constant.

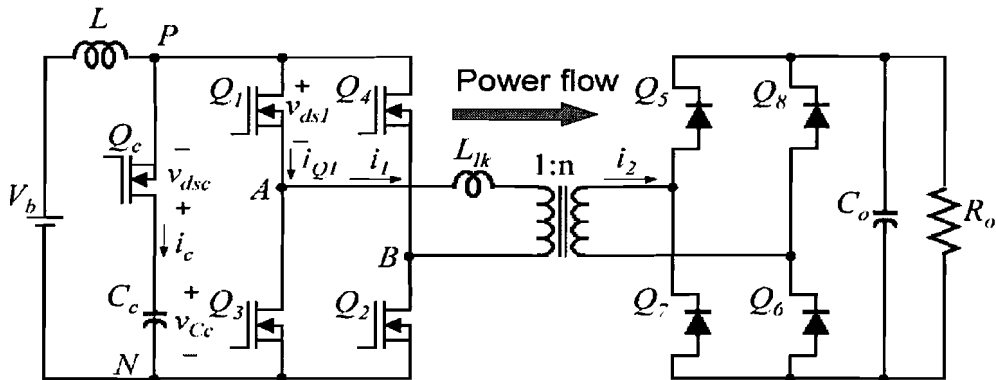


Figure 3.1: Bi-directional DC-DC converter in discharging mode

For a given input voltage and a needed output power the following parameters are then obtained:

- Transformer turns ratio ( $N$ )
- Leakage inductance for achieving ZVS ( $L_k$ )
- The required duty cycle ( $D$ )

To simplify this numerical analysis, all active and passive components are considered as ideal. Furthermore, the output voltage  $V_o$  and the output current  $I_o$  in figure 3.2 will be referred to the primary side, which means that the primary current and voltage are  $I'_o$  and  $V'_o$  respectively.

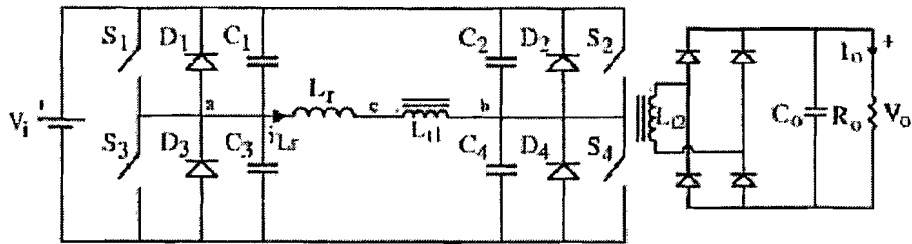


Figure 3.2: FB ZVS DC-DC converter [3]

## 3.2 Key circuit waveforms

The key circuit waveforms of the converter in continuous mode are shown in figure 3.3. Because of the symmetrical waveforms of the converter only one period will be considered in the following section, namely from  $t_3$  to  $t_8$ . As the waveform of the primary side current does not change during the dead time transitions, only three stage will be considered.

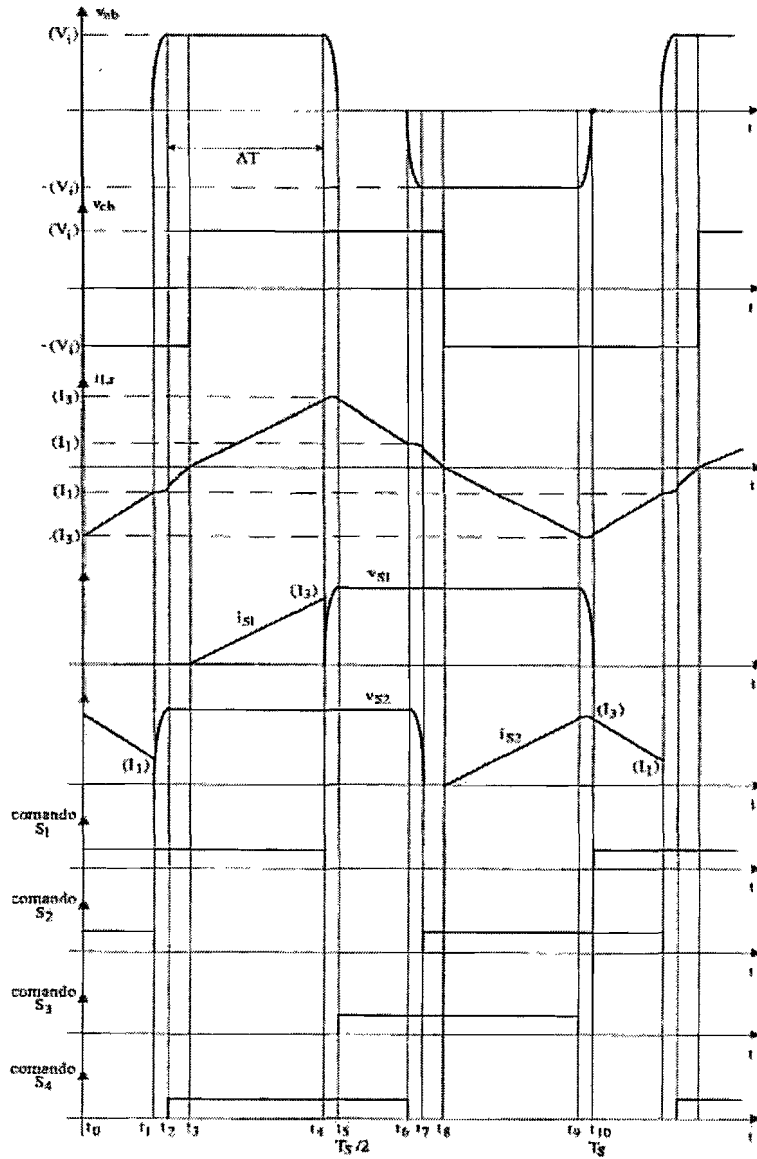


Figure 3.3: Key waveforms of the ZVS FB DC-DC converter

Stage 3 [ $t_2 - t_3$ ]:

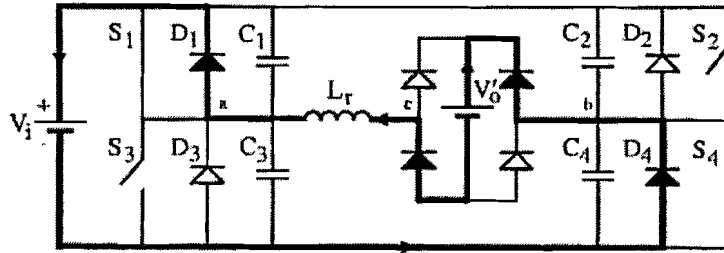


Figure 3.4: Electrical equivalent circuit of stage 3

The electrical equivalent circuit of the third stage leads to the following formula:

$$-(V_i + V'_o) = L_r \frac{di_{Lr}(t)}{dt} \quad (3.1)$$

Integrating this formula from  $t_2$  to  $t_3$  results in:

$$-(V_i + V'_o) \int_{t_2}^{t_3} dt = L_r \int_{I_1}^0 dt \quad (3.2)$$

And this equation on its turn results in:

$$-(V_i + V'_o) \Delta t_{32} = -L_r I_1 \quad (3.3)$$

And after isolating  $I_1$  the following formula is obtained:

$$I_1 = \frac{V_i + V'_o}{L_r} \Delta t_{32} \quad (3.4)$$

Stage 4 [ $t_3 - t_4$ ]:

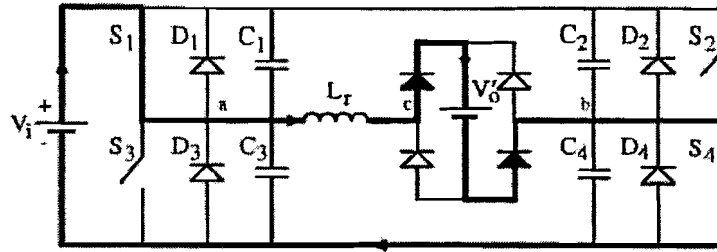


Figure 3.5: Electrical equivalent circuit of stage 4

From the equivalent electrical circuit of this stage we can conclude that:

$$V_i - V_o' = L_r \frac{di_{Lr}(t)}{dt} \quad (3.5)$$

By rewriting this formula and considering the corresponding waveform during this stage, this formula can be written as follows:

$$\frac{V_i - V_o'}{L_r} \Delta t_{43} = I_3 \quad (3.6)$$

This formula gives us an equation for the peak current  $I_3$  through the leakage inductance.

Stage 6 [ $t_5 - t_6$ ]:

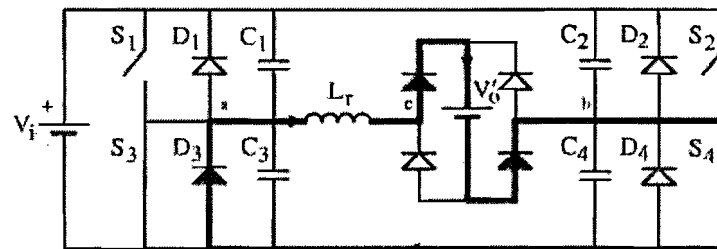


Figure 3.6: Electrical equivalent circuit of stage 6

The electrical equivalent circuit of the sixth stage gives:

$$-V_o' = L_r \frac{di_{Lr}(t)}{dt} \quad (3.7)$$

After integrating this formula from  $t_5$  to  $t_6$  we obtain:

$$\int_{t_5}^{t_6} V'_o dt = -L_r \int_{I_3}^{I_1} di \quad (3.8)$$

Solving this integral gives us the following equation:

$$(t_6 - t_5)V'_o = -L_r(I_1 - I_3) \quad (3.9)$$

And this gives us an equation for the current  $I_1$ :

$$I_1 = I_3 - \frac{V'_o}{L_r} \Delta t_{65} \quad (3.10)$$

From these equations the expressions for the currents  $I_1$  and  $I_3$  are obtained.

### 3.3 Initial conditions

Because of its symmetry, the waveforms of the converter during the following stages can be considered to be equal:

$$\Delta t_{3-2} = \Delta t_{8-7} \quad (3.11)$$

$$\Delta t_{4-3} = \Delta t_{9-8} \quad (3.12)$$

$$\Delta t_{1-0} = \Delta t_{6-5} \quad (3.13)$$

Before deriving the equations for the currents  $I_1$  and  $I_3$  in terms of the converter parameters, first some important parameters are defined:

$\Delta T$  is defined as the time during which the primary side voltage across the transformer is equal to ( $\pm V_i$ ) depending on the direction of the current. From this definition and considering the key waveforms of the circuit we can conclude that:

$$\Delta T = \Delta t_{8-7} + \Delta t_{9-8} \quad (3.14)$$

$$\frac{T_s}{2} \cong \Delta T + \Delta t_{6-5} \quad (3.15)$$

Isolating  $\Delta t_{6-5}$  gives:

$$\Delta t_{6-5} = \frac{T_s}{2} - \Delta T \quad (3.16)$$

Furthermore, the primary-referred voltage gain of the converter, often referred to as the dc conversion ratio, is given by:

$$q = \frac{V'_o}{V_i} = \frac{V_o/n}{V_i} \quad \text{where} \quad n = \frac{N_s}{N_p} \quad (3.17)$$

Finally, the duty cycle of the converter is defined as:

$$D = \frac{2\Delta T}{T_s} \quad (3.18)$$

By substituting the formulas 3.6, 3.3 and 3.16 in 3.10 we obtain:

$$\left( \frac{V_i - V'_o}{L_r} \right) \Delta t_{4-3} = \left( \frac{V_i + V'_o}{L_r} \right) \Delta t_{8-7} + \frac{V'_o}{L_r} \left( \frac{T_s}{2} - \Delta T \right) \quad (3.19)$$

And by substituting 3.14 in 3.19 we obtain:

$$\Delta t_{4-3} = \frac{\Delta T}{2} + \frac{V'_o T_s}{V_i 4} \quad (3.20)$$

Substituting 3.18 in 3.20 and the formula for the switching frequency  $T_s$  lead to the following equation:

$$\frac{\Delta t_{4-3}}{T_s} = \frac{D + q}{4} \quad (3.21)$$

Then 3.21 and 3.18 are substituted in 3.14 giving the following equation:

$$\frac{\Delta t_{8-7}}{T_s} = \frac{D - q}{4} \quad (3.22)$$

Furthermore, the expression 3.21 is substituted in 3.6 which lead to the current  $I_3$ :

$$I_3 = T_s \frac{V_i - V'_o}{L_r} \frac{D + q}{4} \quad (3.23)$$

In order to derive a formula in terms of the duty cycle and the dc conversion ratio, it is necessary to normalize this expression:

$$\boxed{\overline{I}_3 = \frac{I_3 4 f_s L_r}{V_i} = (1 - q)(D + q)} \quad (3.24)$$

To obtain a formula for the current  $I_1$ , 3.22 is substituted in 3.4:

$$I_1 = T_s \frac{V_i + V'_o}{L_r} \frac{D - q}{4} \quad (3.25)$$

Once again this formula has been normalized and lead to the following expression:

$$\boxed{\overline{I}_1 = \frac{I_1 4 f_s L_r}{V_i} = (1 + q)(D - q)} \quad (3.26)$$

### 3.4 Average output current in continuous conduction mode

DC-DC converters can have two distinct modes of operation: Continuous conduction mode (CCM) and discontinuous conduction mode (DCM). In practice, a converter may operate in both modes, which have significantly different characteristics. Therefore, a converter and its control should be designed based on both modes of operation.

The average output current of the converter in continuous conduction mode is depicted in figure 3.7. Again the values of the known currents  $I_1$  and  $I_3$  are used to derive the average output current in CCM.

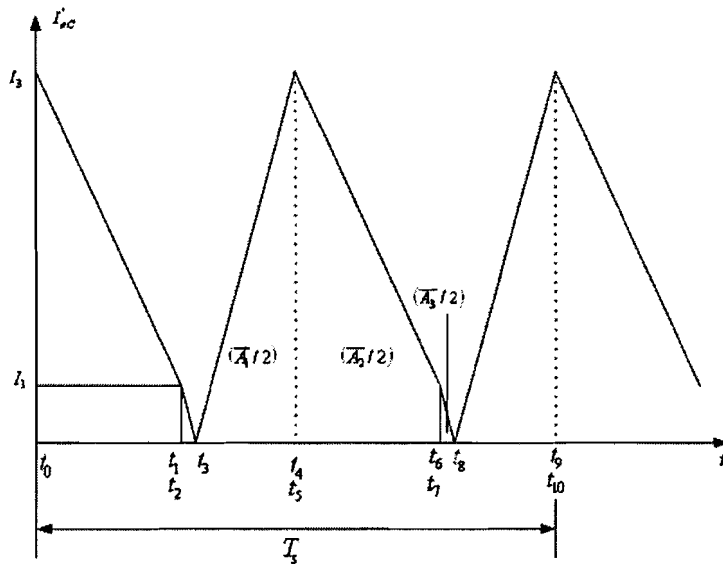


Figure 3.7: Average output current of the converter in CCM

The area  $\overline{A}_1$  is given by the following formula:

$$\overline{A}_1 = \frac{2}{T_s} \frac{I_3 \Delta t_{4-3}}{2} \quad (3.27)$$

After substituting the equations for the current  $I_3$  (3.23) and the time  $\Delta t_{4-3}$  (3.20) the following equation in terms of the converter's parameters is obtained:

$$\overline{A}_1 = \frac{V_i}{16L_r f_s} (1 - q)(D + q)^2$$

(3.28)

The same derivation has been done for area  $\overline{A}_2$  which gives:

$$\overline{A}_2 = \frac{2}{T_s} \frac{(I_1 + I_3) \Delta t_{6-5}}{2} \quad (3.29)$$

After substituting 3.18 in 3.15 the expression for  $t_{6-5}$  is obtained:

$$\Delta t_{6-5} = \frac{T_s}{2} - \Delta T = \frac{T_s}{2}(1 - D) \quad (3.30)$$

And after substituting 3.23, 3.25 and 3.30 in 3.29 we get the formula for the area  $\overline{A}_2$ :

$$\boxed{\overline{A}_2 = \frac{V_i}{8f_sL_r}(1 - D)[(1 + q)(D - q) + (1 - q)(D + q)]} \quad (3.31)$$

The area  $\overline{A}_3$  is given by the following expression:

$$\overline{A}_3 = \frac{2}{T_s} \frac{I_1 \Delta t_{8-7}}{2} \quad (3.32)$$

After substituting 3.25 and 3.22 in 3.32 we obtain:

$$\boxed{\overline{A}_3 = \frac{V_i}{16L_rf_s}(1 + q)(D - q)^2} \quad (3.33)$$

Finally, the average output current is the sum of the three areas  $\overline{A}_1$ ,  $\overline{A}_2$  and  $\overline{A}_3$ , and is as follows:

$$I'_{oCmed} = \frac{V_i}{8f_sL_r} \frac{1}{2} (2D - D^2 - q^2) \quad (3.34)$$

After normalizing this expression we get the average output current of the converter as function of the duty cycle  $D$  and the primary-referred voltage gain of the converter, often referred to as the dc conversion ratio  $q$ :

$$\boxed{\overline{I'_{oCmed}} = \frac{I'_{oCmed}8f_sL_r}{V_i} = D(2 - D) - q^2} \quad (3.35)$$

### 3.5 Average output current in discontinuous conduction mode

Figure 3.10 shows the output current in discontinuous conduction mode. This mode occurs with large inductor current ripple in a converter operating a light load and containing current-unidirectional switches, namely during stage 3 and stage 8.

**Stage 3** [ $t_2 - t_3$ ]:

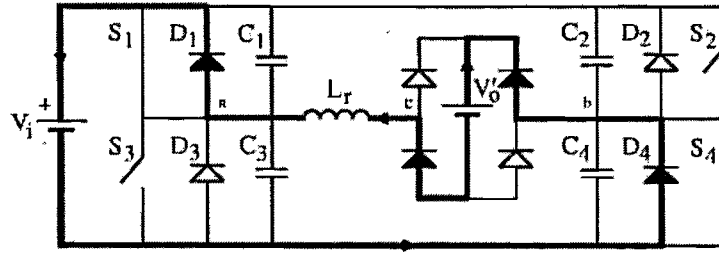


Figure 3.8: Converter operating in DCM during stage 3

**Stage 8** [ $t_7 - t_8$ ]:

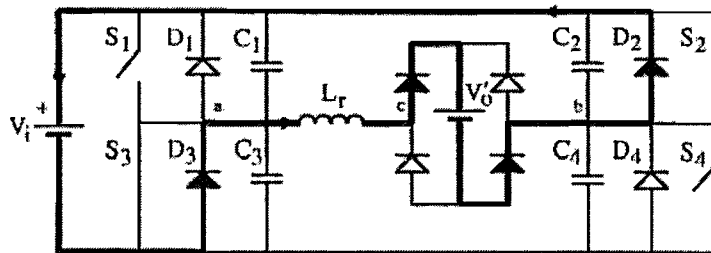


Figure 3.9: Converter operating in DCM during stage 8

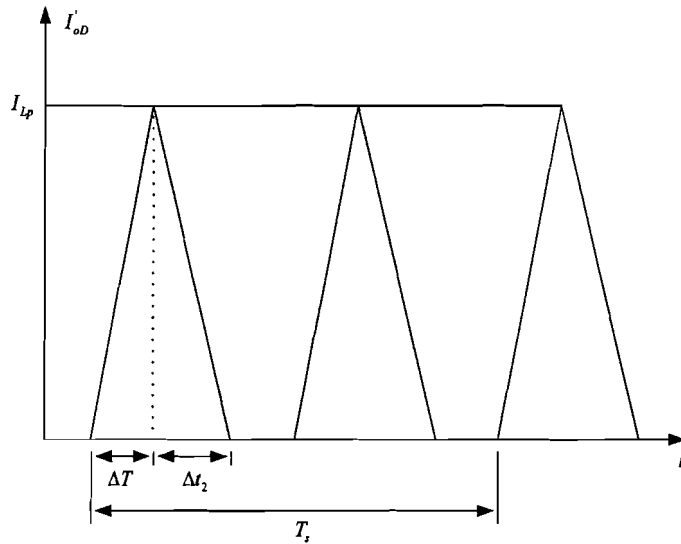


Figure 3.10: Average output current of the converter in DCM

From the electrical equivalent circuits of stage 3 and stage 8 we can derive the expression of the average output current during discontinuous conduction mode. When two switches are conducting we obtain the following expression of the inductor voltage:

$$V_i - V'_o = L_r \frac{di_{Lr}(t)}{dt} = \frac{L_r I_{Lp}}{\Delta T} \quad (3.36)$$

After substituting 3.18 in 3.36 we obtain:

$$I_{Lp} = \frac{V_i - V'_o}{L_r} \frac{DT_s}{2} \quad (3.37)$$

When a switch and a diode are conducting the following equation is obtained:

$$V'_o = -L_r \frac{di_{Lr}(t)}{dt} = -L_r \frac{-I_{Lp}}{\Delta t_2} \quad (3.38)$$

After isolating  $I_{Lp}$  we obtain:

$$I_{Lp} = \frac{V'_o \Delta t_2}{L_r} \quad (3.39)$$

Equalizing the two expressions for  $I_{lp}$  (3.37 and 3.39) leads to:

$$I_{Lp} = \frac{V'_o \Delta t_2}{L_r} = \frac{V_i - V'_o}{L_r} \Delta T \quad (3.40)$$

After substituting 3.37 in 3.39 and using the equation for  $\Delta t_2$  ( $\Delta t_2 = \frac{1-q}{q} \frac{DT_s}{2}$ ) we get the expression for the average output current in discontinuous conduction mode:

$$I'_{oDmed} = \frac{2}{T_s} \left[ \frac{I_{Lp} \Delta T}{2} + \frac{I_{Lp} \Delta t_2}{2} \right] \quad (3.41)$$

Substituting 3.41 in 3.42 gives the following:

$$I'_{oDmed} = \frac{1-q}{q} \frac{V_i}{L_r} \frac{D^2}{4f_s} \quad (3.42)$$

And again this expression has been normalized:

$$\overline{I'_{oDmed}} = \frac{I'_{oDmed} 8 L_r f_s}{V_i} = 2 D^2 \left( \frac{1-q}{q} \right) \quad (3.43)$$

In discontinuous mode we know that:

$$\frac{\Delta t_{8-7}}{T_s} = \frac{D-q}{4} = 0 \quad (3.44)$$

This means the following:

$$D = q \quad (3.45)$$

After substituting 3.45 in 3.43 we obtain an expression that represents the boundary between the CCM and DCM:

$$q^2 - q + \frac{\overline{I'_{oDmed}}}{2} = 0$$

(3.46)

Figure 3.11 shows the relationship between the normalized average output current of the converter ( $I_{o,med}$ ) and the DC conversion ratio ( $q$ ) as function of the duty cycle ( $D$ ) for CCM and DCM.

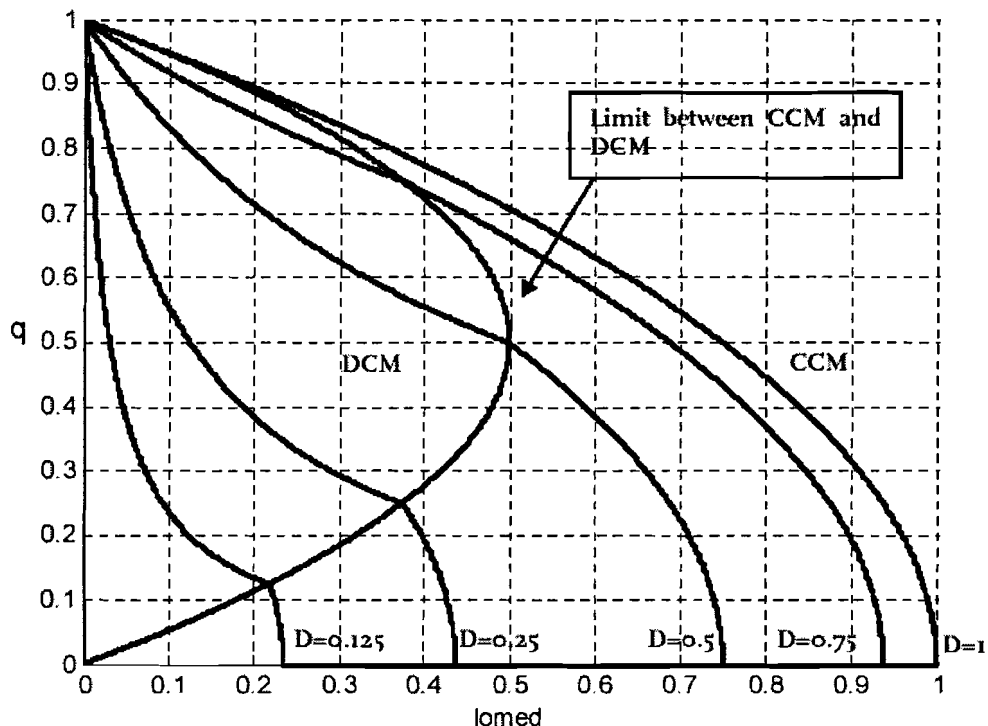


Figure 3.11: Relation between average output current and the DC conversion ratio as function of the duty cycle

The Matlab files that are written to calculate the relation between the average output current of the converter and the DC conversion ratio as function of the duty cycle, and to derive the converter parameters are included in appendix A and appendix B.

# Chapter 4

## Bi-directional DC-DC converter

### 4.1 Introduction

This chapter presents the chosen bi-directional DC-DC converter for the Fuel Cell energy management system. First of all, the topology evaluation for a bi-directional DC-DC converter will be discussed. Then, the working of the converter in discharging mode operation and charging mode operation will be described. These sections will be followed by the simulation results that are obtained by using the power electronics simulation program PSIM.

### 4.2 Topology evaluation for Bi-directional DC-DC converter

In theory, several different types of circuit topologies can be used to realize a bi-directional DC-DC converter, namely single-stage buck/boost type or a full-bridge type as a typical one. The Full-bridge type topology has the following merits compared to the single-stage buck-boost type topology:

- Electrical isolation between input and output is guaranteed
- Higher boost ratio can be implemented
- System protection is possible when output stage short take place

For these reasons a full bridge type topology has been chosen for the bi-directional DC-DC converter as is shown in figure 4.1.

To avoid the need for a high leakage inductance transformer, it is necessary to place either current-fed or voltage-fed on either low-voltage (LV) or high-voltage (HV) side. After literature research, taking into account the component usage and efficiency among half-bridge, push-pull, and full-bridge converters, it was concluded that putting current-fed on the battery side makes more sense [4].

Placing a current-fed converter on the battery side gains a significant advantage in charging-mode efficiency and is the preferred choice.

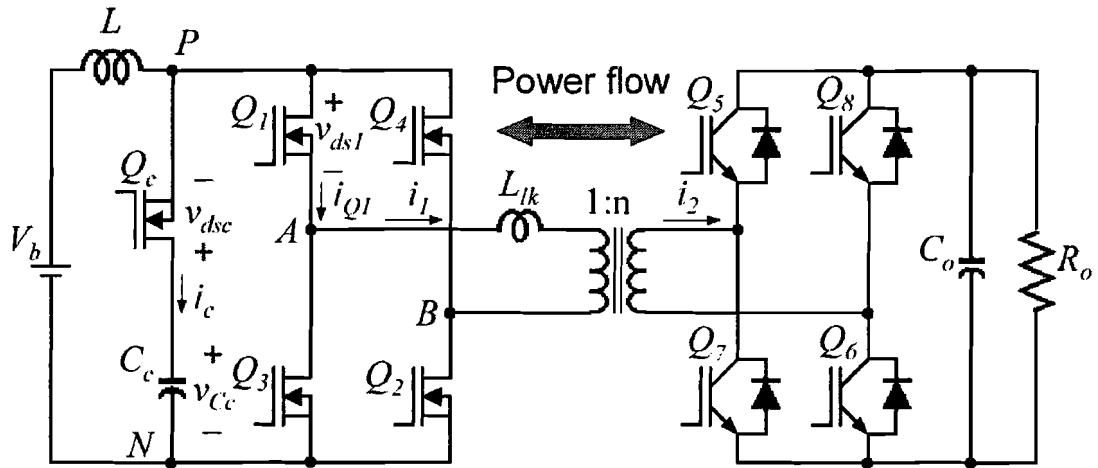


Figure 4.1: Low-side full-bridge current-fed with active clamp and high-side full-bridge voltage-fed converter

This converter has two active switch bridges on both sides of an isolation transformer.

- The bridge on the high voltage side fed by a voltage source (referred to as voltage fed full-bridge).
- The bridge on the low voltage side fed by a current source (referred to as current-fed full bridge).

An active clamp branch placed across the current-fed bridge is used to achieve ZVZCS for the voltage-fed bridge switches in buck mode, and clamp the transient voltage on the current-fed bridge. This active clamp branch consists of an active switch and an energy storage capacitor.

For the primary side switches, MOSFET's are selected because of the low voltage and high current rate. Whereas IGBT's are preferable to MOSFET's for the high side switches because of the voltage rating. However, the choice of IGBT's for the high side switches is not obvious in case of a switching frequency of 100kHz or higher.

In the high-power bi-directional DC-DC converter, the isolated full-bridge converter with an active clamp has been a good choice due to its effectiveness to limit the overshoot of bridge switch's turn off voltage and to enable the energy stored in the transformer leakage inductance to be used for zero voltage switching [4].

## 4.3 Discharging mode operation (Boost mode)

### 4.3.1 Principle of operation

Figure 4.2 shows the proposed full-bridge isolated current-fed converter with an active clamp during the boost mode operation (discharging mode). During this mode the battery voltage of 48V will be converted to a voltage of 400V on the DC link bus.

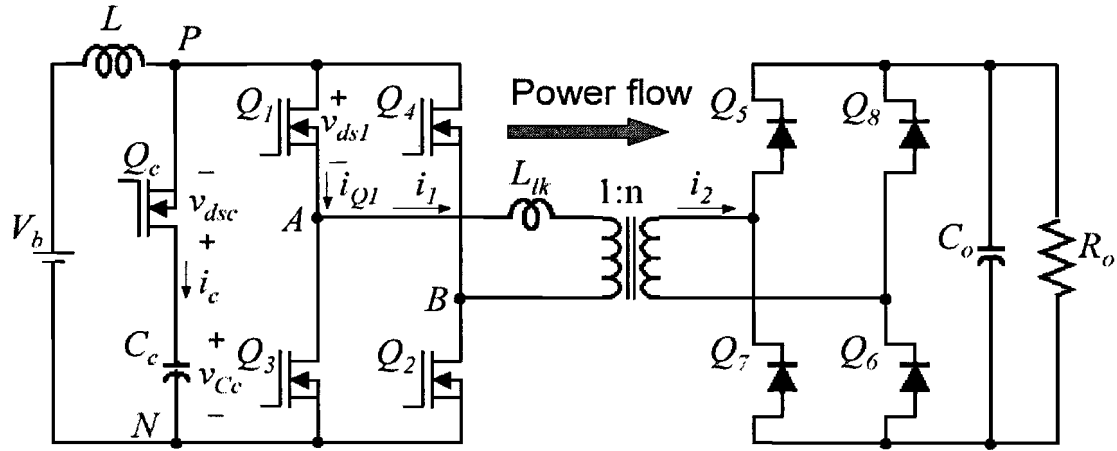


Figure 4.2: Bi-directional DC-DC converter in discharging mode

The timing diagram and the key waveforms of the converter are depicted in figure 4.3. Because of the symmetry of the converter only one period will be described.

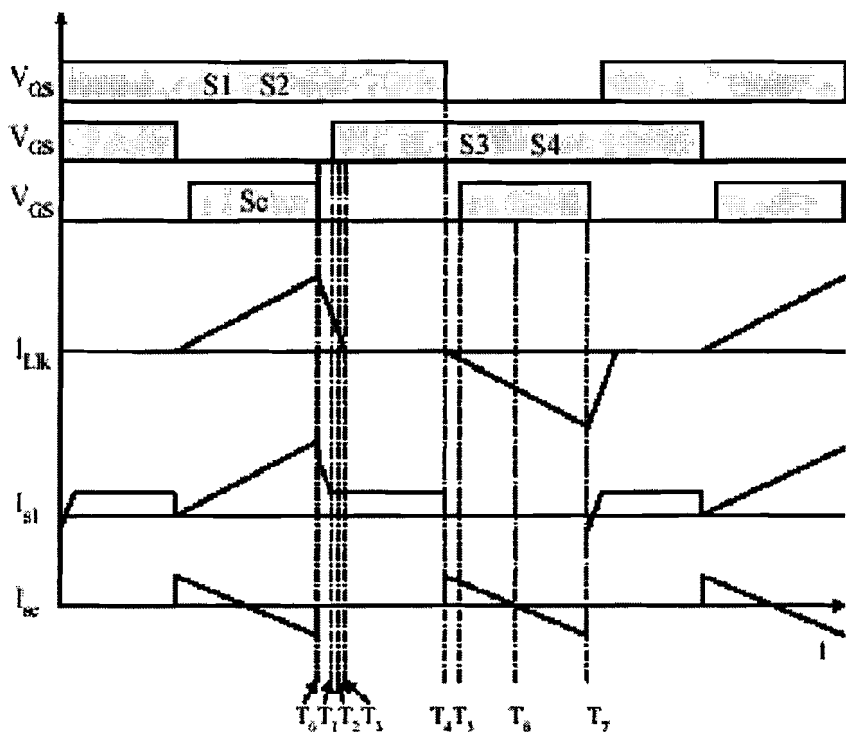


Figure 4.3: Typical waveforms of the Bi-directional DC-DC converter in discharging mode

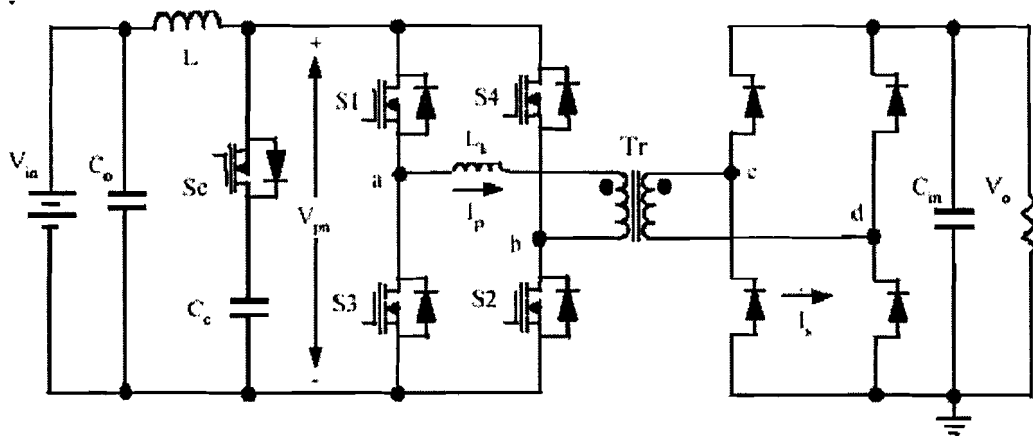


Figure 4.4: Bi-directional DC-DC converter with the corresponding currents and voltages

**Stage 1:**

When the converter is operating in the steady state, the bridge switch pairs in diagonal positions conduct with a duty cycle larger than 0.5. As a consequence, the boost inductor is charged during the overlapping interval when all four of the bridge switches are on ( $T_1 - T_4$ ) and discharged when one diagonal switch pair is switched off and the clamp switch is turned on ( $T_5 - T_7$ ).

**Stage 2:**

At  $T_4$ , the active clamp switch  $S_c$  turns on under zero voltage switching condition because  $I_{sc}$  goes through the diode of  $S_c$  first.

**Stage 3:**

During the time interval from  $T_5$  to  $T_7$ , the voltage difference between the clamp capacitor and the reflected output voltage is exerted on the leakage inductor of the transformer.

The clamp capacitor current  $I_c$  shows symmetrical charge and discharge allowing the dc bus voltage,  $V_{pn}$  to be properly clamped.

Thus, the transformer current increases at a rate of  $-(V_c - V_o)/L_k$ . From  $T_5$  to  $T_6$ , the surplus inductor current runs into the clamp branch, and from  $T_6$  to  $T_7$ , the clamp capacitor supplies the deficient current to the transformer leakage current.

**4.3.2 Design of the energy storage capacitor  $C_c$ :**

The design of  $C_c$  is based on the resonant tank formed by  $C_c$  and  $L_k$ . The resonance between these two components occurs during the off stage of boost mode operation. So its maximum span must exceed about  $T_s/2$ . The criterion is to select  $C_c$  such that the resonant period is larger than  $T_s/2$  which means the following:

$$C_c \geq \frac{(T_s/4\pi)^2}{L_k} \quad (4.1)$$

Where:  $L_k = L_{lk}/n^2$ , the transformer leakage inductance reflected to the current-fed side (primary side) and  $T_s$  is the period of the driving signal for each bridge switch.

From the numerical analysis treated in chapter 3, the required leakage inductance ( $L_k$ ) of the transformer should be  $2.10\mu H$  in order to achieve softswitching of the converter

Mosfets. Substituting the value of  $L_k$  in formula 4.1 leads to the following value for the energy storage capacitor  $C_c$ :

$$C_c \geq 8\mu F \quad (4.2)$$

Finally, as part of the active clamp branch, an energy storage capacitor of  $C_c = 20\mu F$  has been selected.

### 4.3.3 Voltage across the active clamp branch:

In order to treat the active clamp bi-directional DC-DC converter as a normal full bridge DC-DC converter, the expression for  $V_{cc}$  should be determined first. Under the condition that  $V_i = V_{cc}$ , the numerical analysis that is treated in chapter 3 can then be applied to the bi-directional DC-DC converter.

The active clamp branch in combination with the input inductor can be considered as an up converter. As mentioned earlier, the boost inductor ( $L$ ) is charged during the overlapping interval when all four of the bridge switches are on ( $T_1 - T_4$ ) and discharged when one diagonal switch pair is switched off and the clamp switch is turned on ( $T_5 - T_7$ ).

The voltage across the input inductor,  $L$  will be considered. For steady state conditions, the voltage  $\times$  time product applied to the inductance over a complete cycle must equal zero. When  $S_1, S_2$  are on and  $S_3, S_4$  are off the following expressions are obtained:

$$V_l = V_{bat} - V_{cc} \quad or \quad \frac{di_l}{dt} = \frac{1}{L}(V_{bat} - V_{cc}) \quad (4.3)$$

When  $S_1, S_2, S_3$ , and  $S_4$  are on, the above expressions become as follows:

$$V_l = V_{bat} \quad or \quad \frac{di_l}{dt} = \frac{V_{bat}}{L} \quad (4.4)$$

As the voltage across the inductor is equal to zero after one period of time the following equation can be written as follows:

$$(V_{bat} - V_{cc})D = -V_{bat}(1 - D) \quad (4.5)$$

Where the duty cycle  $D$  is defined as:  $D = \frac{2\Delta T}{T_s}$

This leads to the following expression for the voltage across the clamp capacitor as function of the duty cycle:

$$V_{cc} = \frac{V_{bat}}{D} \quad (4.6)$$

#### 4.3.4 Input inductor design

When the battery is being charged or discharged, the ripple component in the current should be restricted by the input inductor that is depicted in figure 4.2. However, as the maximum battery discharge current is much larger than the maximum battery charge, the magnetic components should be designed based on the discharging mode.

As the maximum discharging current is assumed to be  $22A$ , the allowed ripple is about 10 per cent of the maximum discharging current. That means that  $\Delta i_L = 2.2A$ . To allow such a current ripple, the input inductor should be as follows:

$$\Delta i_L = \frac{1}{L} (|V_{bat} - V_{cc}|) (1 - D) \frac{1}{T_s} \quad (4.7)$$

That means that:

$$L = \frac{(|V_{bat} - V_{cc}|) (1 - D)}{T_s \Delta i_L} \quad (4.8)$$

After substituting the values in equation 4.8, the inductor value should be  $102\mu H$ . However, designing this inductor for a current rating of about  $25A$  leads to a huge component. In order to decrease the inductor value and to keep the allowable current ripple equal to  $2.2A$  the following configuration has been used:

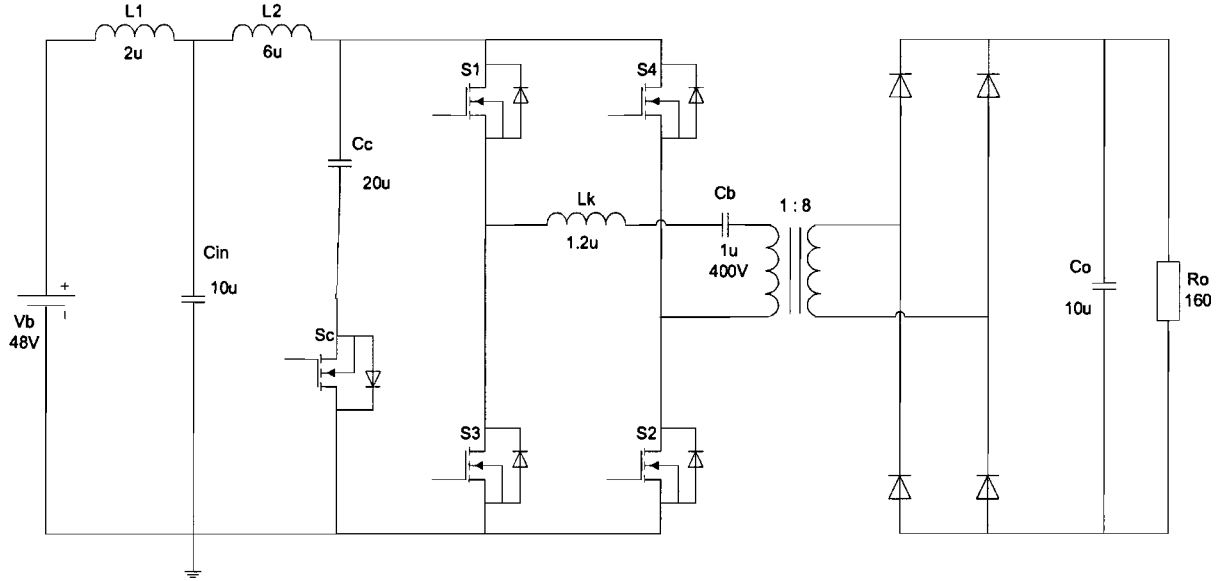


Figure 4.5: Bi-directional DC-DC converter in discharging mode with modification of input inductor

The principle is as follows, by adding an extra inductor  $L_2$  in combination with an input capacitor  $C_{in}$ , it is possible to protect the battery and to obtain a small input inductor with the desired current ripple of about  $2.2A$ .

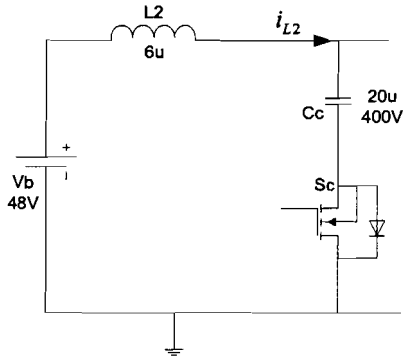


Figure 4.6: Design configuration  $L_2$

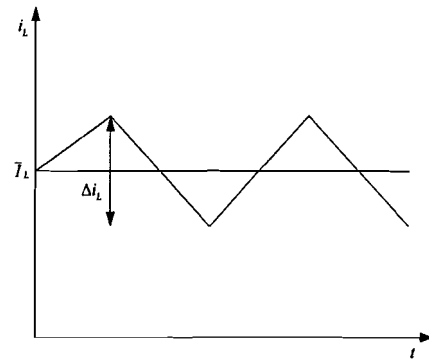


Figure 4.7: Illustration of current ripple

Let's consider the design of  $L_2$  in figure 4.6. After choosing an acceptable value for  $L_2$ , namely  $6\mu H$ , the ripple of  $i_{L2}$  can be determined as follows:

$$\Delta i_{L2} = \frac{1}{L} (|V_{bat} - V_{cc}|) (1 - D) \frac{1}{T_s} \quad (4.9)$$

That leads to a current ripple of  $\Delta i_{L2} = 21A$ .

Furthermore,  $L_1$  has chosen to be  $2\mu H$ . From the  $LC$  combination depicted in figure 4.8 the current ripple of  $L_1$  and  $C_{in}$  can be determined.

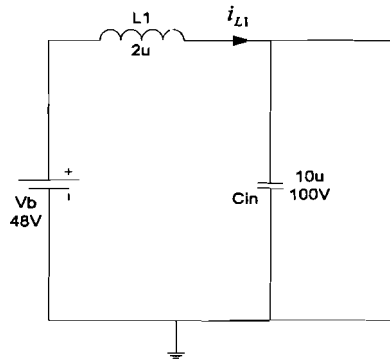


Figure 4.8: Design configuration  $L_1$

The impedances of  $L_1$  and  $C_{in}$  are as follows:

$$X_{L1} = 2\pi f_s L = 2\pi 100 \cdot 10^3 2 \cdot 10^{-6} = 1.26\Omega \quad (4.10)$$

$$X_{Cin} = \frac{1}{2\pi f_s C_{in}} = \frac{1}{2\pi 100 \cdot 10^3 10 \cdot 10^{-6}} = 0.159\Omega \quad (4.11)$$

With the aid of the impedances the ripple of the current through  $L_1$  and  $C_{in}$  can be calculated as follows:

$$\Delta i_{L1} = \frac{X_{Cin}}{X_{L1} + X_{Cin}} \Delta i_{L2} \quad (4.12)$$

That gives  $\Delta i_{L1} = 2.35A$ .

$$\Delta i_{Cin} = \frac{X_{L1}}{X_{Cin} + X_{L1}} \Delta i_{L2} \quad (4.13)$$

That gives  $\Delta i_{Cin} = 18.64A$ .

As can be seen, a very small battery current ripple is achieved with a much smaller inductor value. That means that most of the ripple is taken on by the capacitor  $C_{in}$  and the inductor  $L_2$  to protect the battery. In order to handle such a high current through the electrolytic capacitor  $C_{in}$ , a plastic capacitor is connected in parallel with  $C_{in}$ .

## 4.4 Simulation results

The bi-directional DC-DC converter has been simulated and the simulation circuit is depicted in figure 4.9. It consists of an active clamp full bridge DC-DC converter with the corresponding dead time and phase shift control. The phase shift has been chosen to be  $180^\circ$ . Furthermore, the simulations are performed with the following system parameters:

Input voltage (battery)	$V_{bat} = 48V$
Output voltage	$V_o = 400V$
Output power	$P_o = 1kW$
Transformer turns ratio	$N_p : N_s = 1 : 8$
Duty cycle	$D = 0.6$
Leakage inductance	$L_k = 2.10\mu H$
Active clamp capacitor	$C_c = 20\mu F$
Switching frequency	$F_s = 100kHz$

Table 4.1: System parameters of the Bi-directional DC-DC Converter

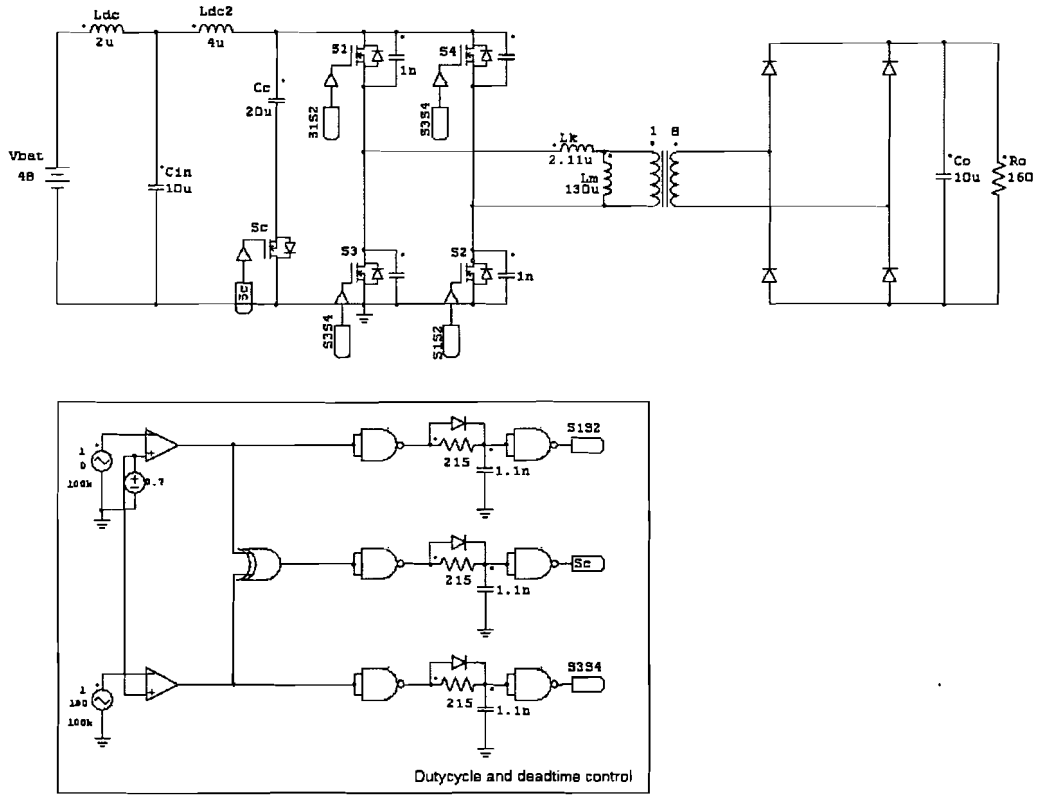


Figure 4.9: Simulation circuit of the Bi-directional DC-DC converter in discharging mode

The switching patterns are depicted in the figure below. As can be seen, the active clamp switch is activated when one of the diagonal switch pairs is turned off.

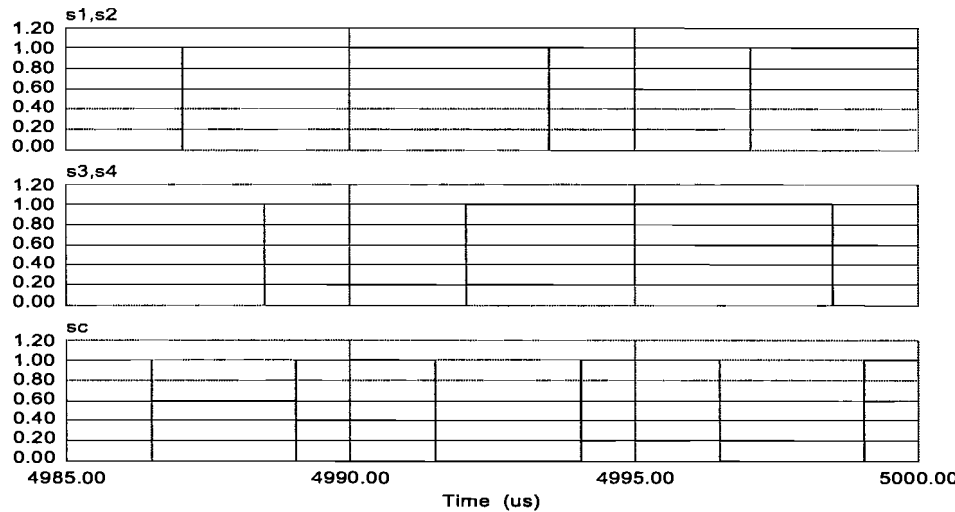


Figure 4.10: Switching patterns of the MOSFET's

Figure 4.11 shows the output voltage of the converter bridge and the input voltage of the transformer. As can be seen in figure 4.11 and 4.12, the output voltage of the bridge is properly clamped by the clamp capacitor.

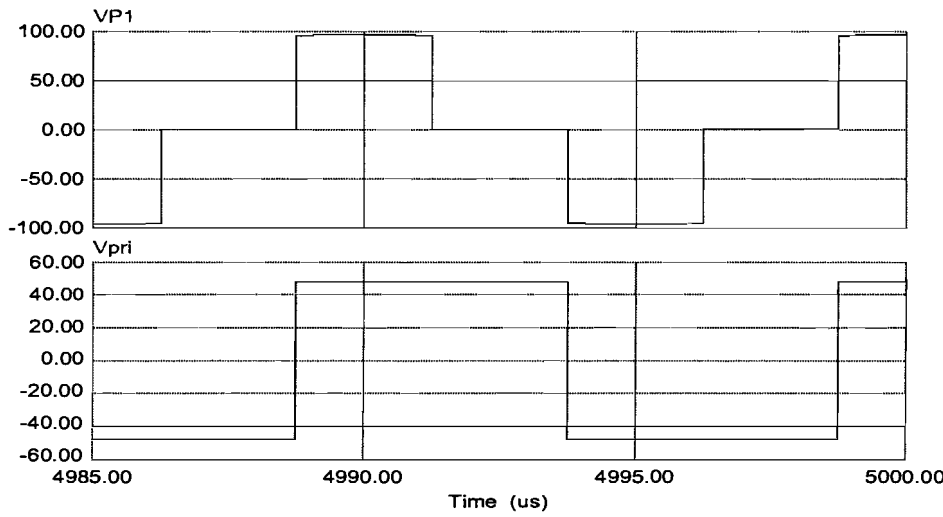


Figure 4.11: 1) Output voltage of the bridge 2) Input voltage of the transformer

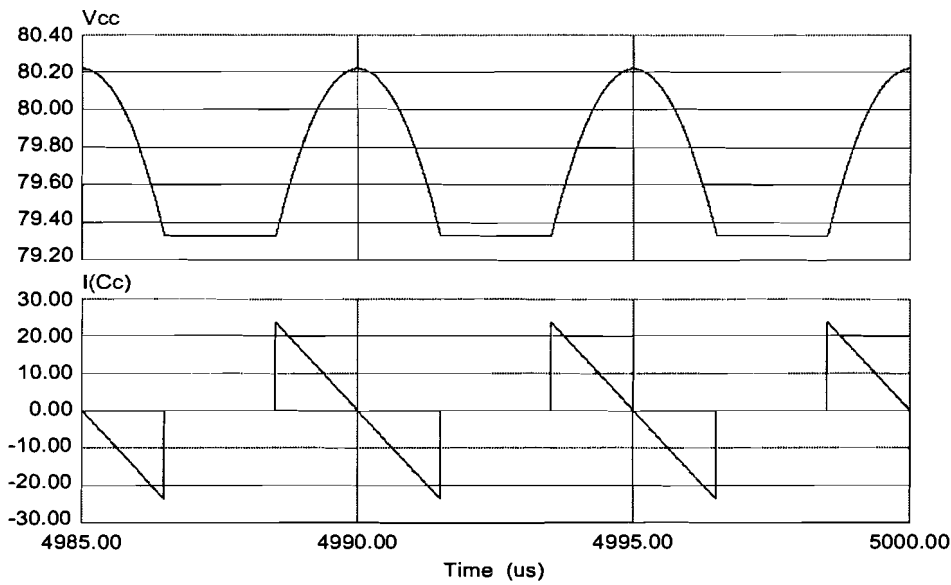


Figure 4.12: 1) Voltage across the clamp capacitor 2) Current through the clamp capacitor

The voltage ( $V_{ds}$ ) across the active clamp switch  $S_c$  and the current through this switch are shown by the figure below.

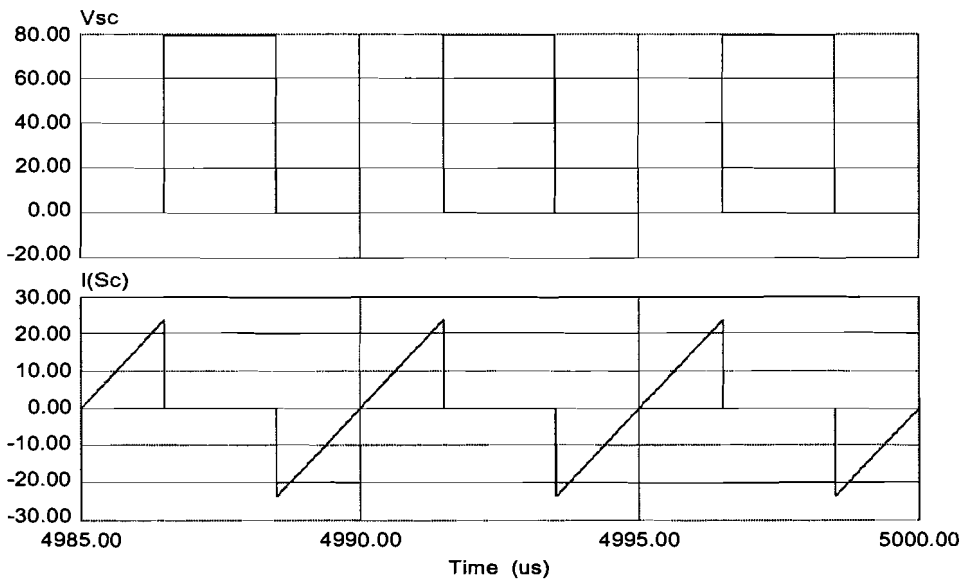


Figure 4.13: 1) Voltage across  $S_c$  2) Current through  $S_c$

The current through the leakage inductance and the average output current are depicted in figure 4.10.

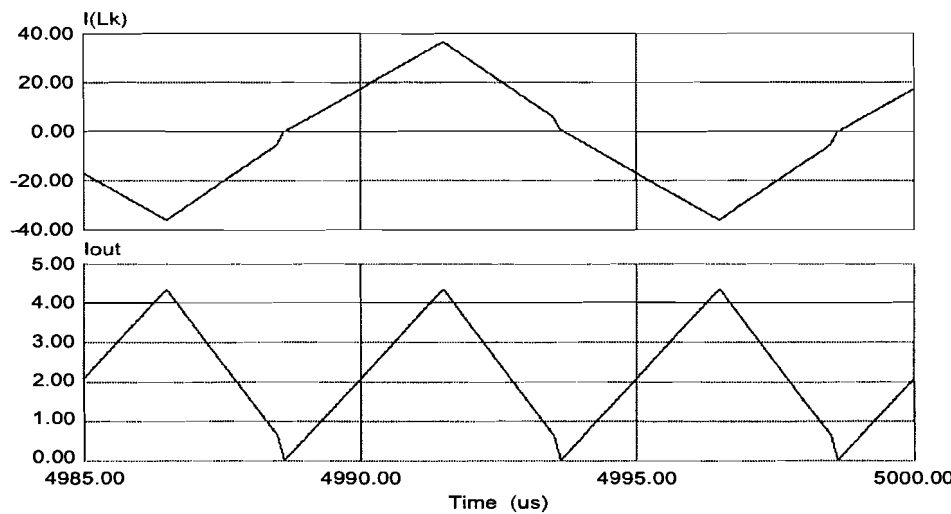


Figure 4.14: 1) Leakage inductance current 2) Average output current

Figure 4.15 shows the voltage ( $V_{ds}$ ) across one switch of a converter leg and the corresponding current through the same switch.

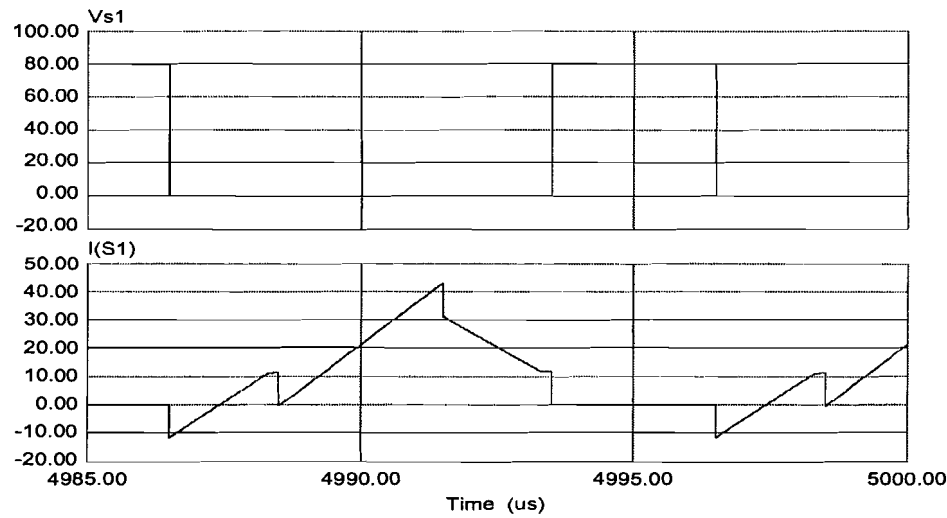


Figure 4.15: 1) Voltage across  $S_1$  2) Current through  $S_1$

Finally, the load voltage and load current of the bi-directional DC-DC converter in discharging mode are shown in figure 4.16.

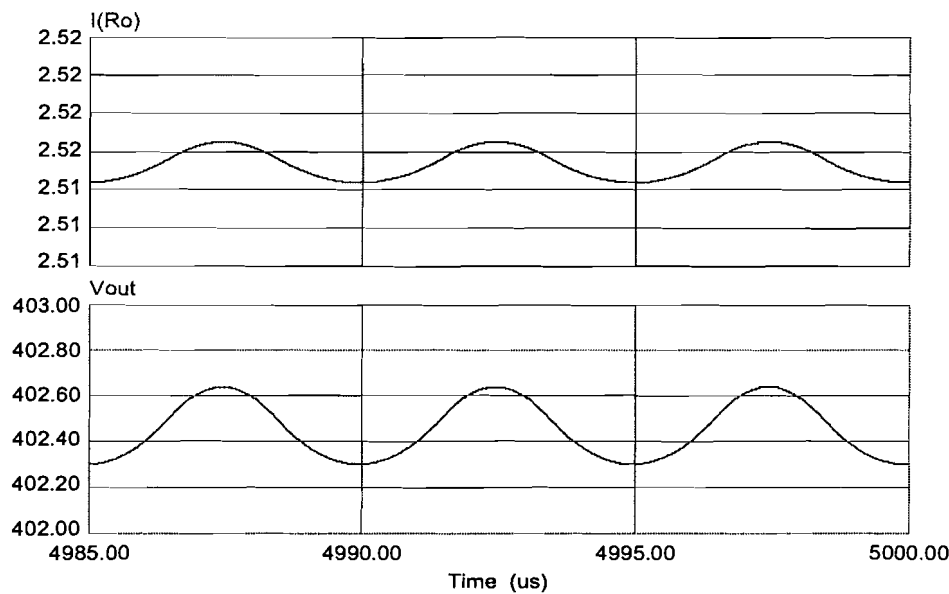


Figure 4.16: 1) Load current 2)Load voltage

## 4.5 Charging mode operation (Buck mode)

### 4.5.1 Charging mode operation without synchronous rectification

The bi-directional DC-DC converter during buck mode operation (charging mode) is depicted in figure 4.17. In this operation mode of the bi-directional DC-DC converter, the converter can be implemented with hybrid zero-voltage and zero-current switching (ZVZCS) for the full-bridge converter on the low side. However, the full-bridge converter with active clamp can achieve ZVZCS handily with the existing clamp switch using a control timing modified from what was proposed in [5].

Synchronous rectification can also be used for the current-fed side (boost mode side) switches to reduce the conduction loss. With the active clamp circuit, the activation of the clamp switch,  $S_c$ , can reset the free-wheeling current, and at the same time, realize zero-current-switching (ZCS) for one pair of switches, namely the so-called lagging leg switches,  $S_8$  and  $S_6$ .

It should be mentioned that the concept to achieve ZVZCS with the help of an active clamp branch on the current-fed side was first introduced in [5].

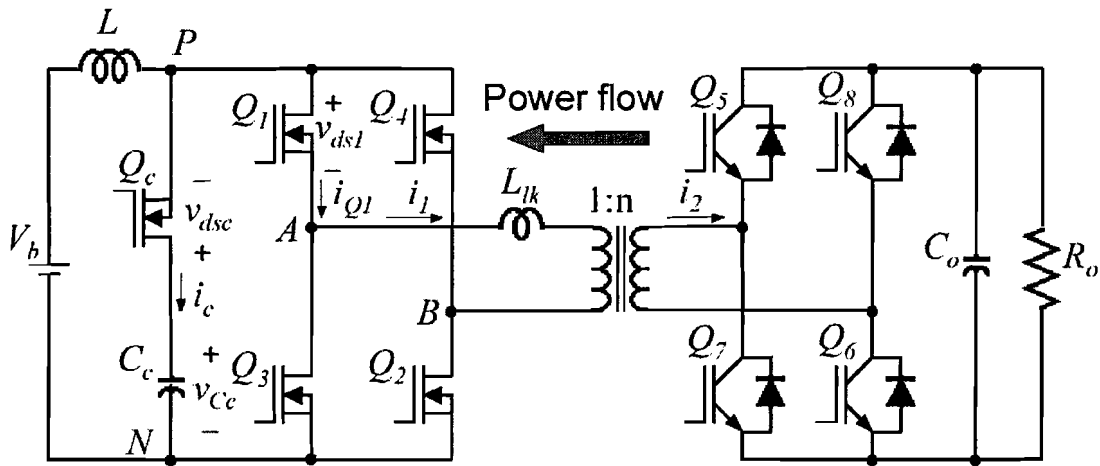


Figure 4.17: Bi-directional DC-DC converter in charging mode

The timing diagram and the key circuit waveforms are shown in figure 4.19. The operation without synchronous rectification, i.e. without activation of  $S_1$ ,  $S_2$ ,  $S_3$ , and  $S_4$  will be discussed first.

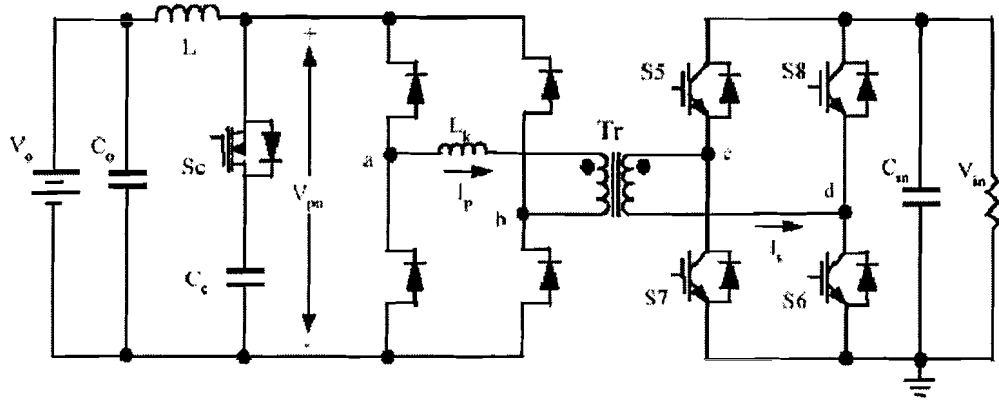


Figure 4.18: Bi-directional DC-DC converter in charging mode with corresponding currents and voltages

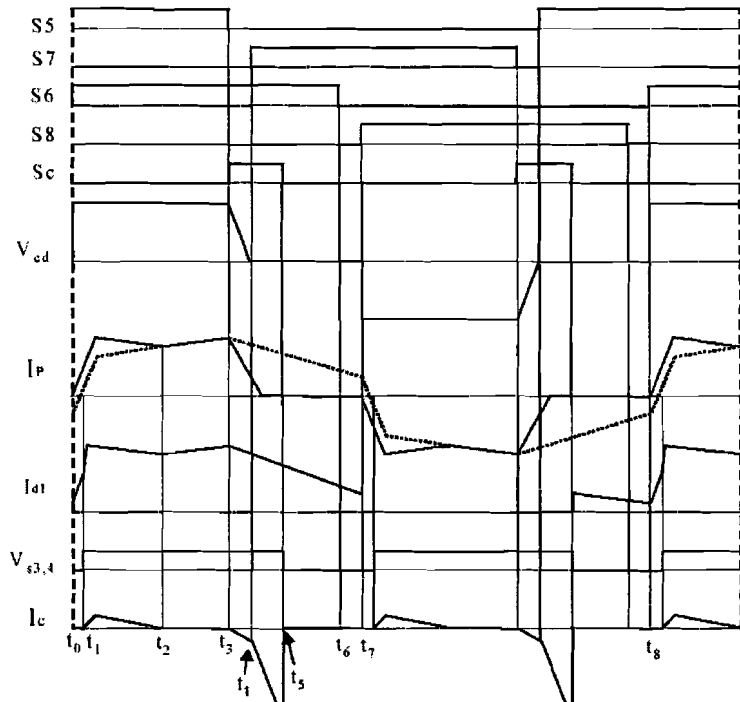


Figure 4.19: Typical waveforms of the Bi-directional DC-DC converter

**Stage 1** [ $t_0 - t_1$ ]:

Before time  $t_0$  the high side switch  $S_5$  was already on, whereas the low voltage side switches are taking the freewheeling load current. At time  $t_0$ ,  $S_6$  is turned on and the voltage  $V_{in}$  (battery voltage) is applied on the high side transformer winding, and  $V_{cd}$  becomes positive. At this time  $V_{cd}$  is only seen by the transformer leakage inductance that is reflected on the high side,  $L_k$ . The current through the high side transformer winding rises quickly with the slope of:

$$\frac{V_{in}}{L_k} \quad (4.14)$$

When the high side transformer current increases to the reflected load current level at  $t_1$  the freewheeling current will be taken only by the body diodes of  $S_1$  and  $S_2$ . The transformer secondary side voltage  $V_{ab}$  also becomes positive and changes to the reflected voltage from the high side, i.e.:

$$\frac{V_{in}}{n} \quad (4.15)$$

Where:  $n$  is the transformer turns ratio.

The body diodes in switch  $S_3$  and  $S_4$  are turned off during this moment. The diode reverse recovery problem happens at the turn-off moment, which shows up as voltage spikes on the voltage waveform.

**Stage 2** [ $t_1 - t_2$ ]:

At time  $t_1$  the transformer current reaches the load current level and  $V_{pn}$  is equal to the reflected voltage  $\frac{V_{in}}{n}$ . The leakage inductor  $L_k$  and the clamp capacitor  $C_c$  form a  $LC$  resonant tank. The resonant cycle begins when the clamp capacitor is charged by the current that goes through the diode of the active clamp switch. This process ends at  $t_2$  when the clamp capacitor is going to discharge but blocked by the clamp switch  $S_c$ .

**Stage 3** [ $t_2 - t_3$ ]:

After time  $t_2$ , the circuit goes on to run the normal phase shift. The output side (high voltage side) choke continues to be charged with the rising slope of:

$$\frac{V_{in}/n - V_o}{L} \quad (4.16)$$

**Stage 4** [ $t_3 - t_4$ ]:

At time  $t_3$ , one phase shift duty cycle ends with the turn-off of  $S_5$ . The load current on the secondary side will charge the parasitic capacitance of  $S_5$  and discharge the parasitic capacitance of  $S_7$ . The anti-parallel diode of  $S_7$  will take the freewheeling leakage current.

On the other side at the same time,  $S_c$ , is turned on, and the clamp capacitor  $C_c$  will hold the bus voltage  $V_{pn}$  high. This voltage is reflected to the transformer secondary side between node  $c$  and  $d$  and applied on the leakage inductance and reset the freewheeling current.

**Stage 5** [ $t_4 - t_5$ ]:

During stage 5,  $S_7$  can be turned on with ZVS because its anti-parallel diode is conducting. And the freewheeling current on the high side continues to reduce until zero. Then the anti-parallel diode of  $S_1$  and  $S_2$  starts to block. At the same time, the output load current is increasing and is provided by the clamp branch.

**Stage 6** [ $t_5 - t_6$ ]:

At time  $t_5$ ,  $S_c$  is turned off.  $V_{pn}$  drops to zero and the freewheeling cycle on the low voltage side is initiated. The output inductor freewheels through all low voltage side switches. Comparing with the normal phase shift circuit, the difference is that there is no freewheeling current in the high voltage side. As a result the conduction loss is saved.

**Stage 7** [ $t_6 - t_7$ ]:

At time  $t_6$ ,  $S_6$  is turned off under ZCS condition because the leakage current was already reset to zero.

**Stage 8** [ $t_7 - t_8$ ]:

At time  $t_7$ ,  $S_8$  is turned on and the circuit begins another half cycle which is the same as described earlier. The only difference is that the voltage on the transformer reverses polarity and the active switches changes to the other diagonal pair.

In the current waveform  $I_p$  in figure 4.19, the dotted lines represent the current waveform under normal phase shift operation i.e. without activation of the voltage clamp switch. It can be seen that the high freewheeling current is reset effectively.

The benefits of the ZVZCS discussed in this section are as follows:

- The conduction loss during the freewheeling cycle is eliminated on the high voltage side switches.
- The turn-off loss on the high voltage side full-bridge is reduced by shifting the leakage current to the primary side. The unsecured ZVS turn-on of  $S_6$  and  $S_8$  is replaced by the ZCS turn-off.

### 4.5.2 Simulation results

The bi-directional dc-dc converter in charging mode operation has been simulated and the simulation circuit is depicted in figure 4.20. The simulations have been performed with the following system parameters:

Input voltage (high side DC bus)	$V_{in} = 400V$
Output voltage (battery)	$V_o = 48V$
Output power	$P_o = 100W$
Transformer turns ratio	$N_p : N_s = 1 : 8$
Duty cycle	$D = 0.5$
Leakage inductance	$L_k = 2.10\mu H$
Active clamp capacitor	$C_c = 20\mu F$
Switching frequency	$F_s = 100kHz$

Table 4.2: System parameters for the simulation

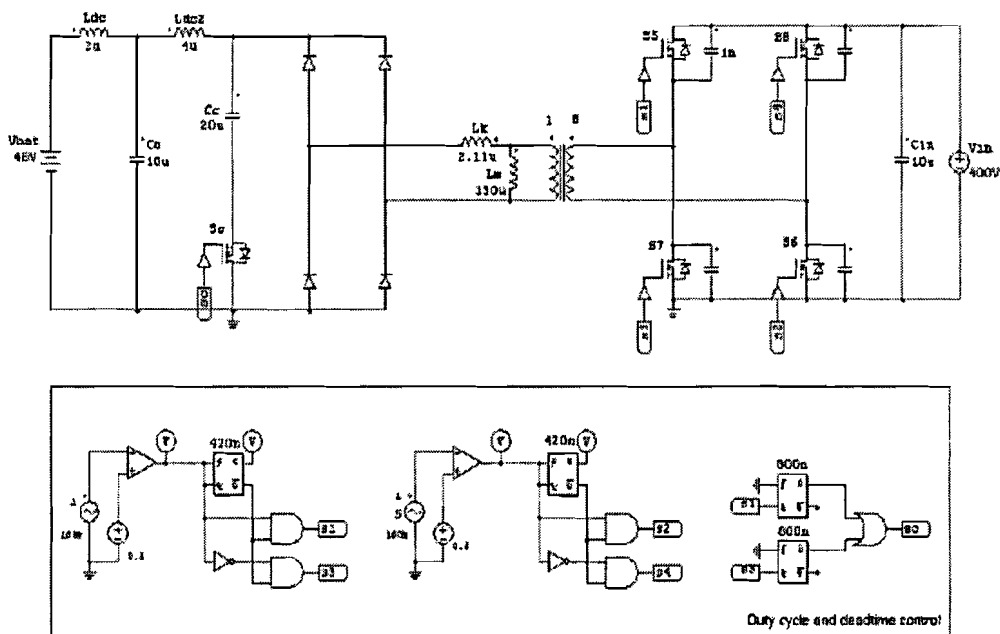


Figure 4.20: Simulation circuit of the Bi-directional DC-DC converter in charging mode

The switching patterns of the switches of the converter are depicted in figure 4.21.

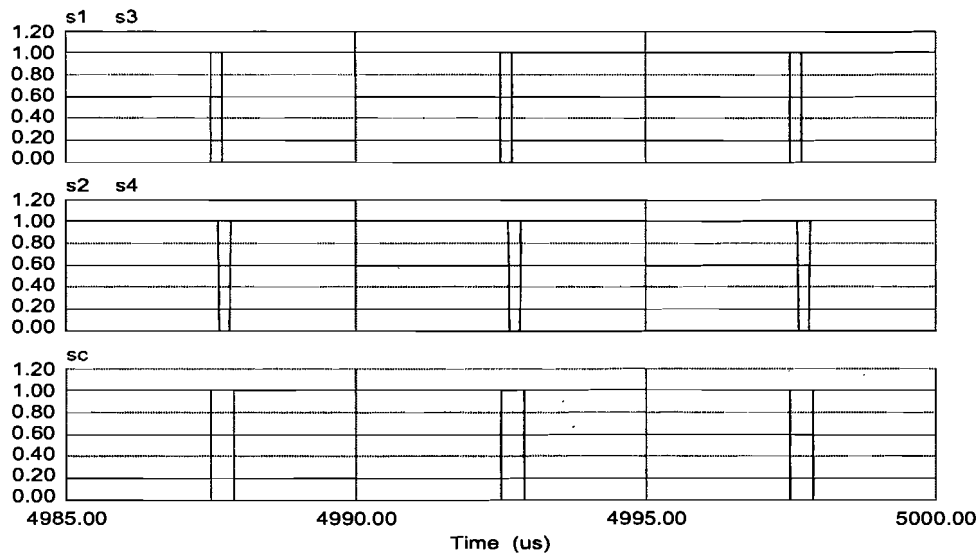


Figure 4.21: Switching patterns of the switches

Figure 4.22 shows the output voltage of the converter bridge and the voltage across the secondary side of the transformer.

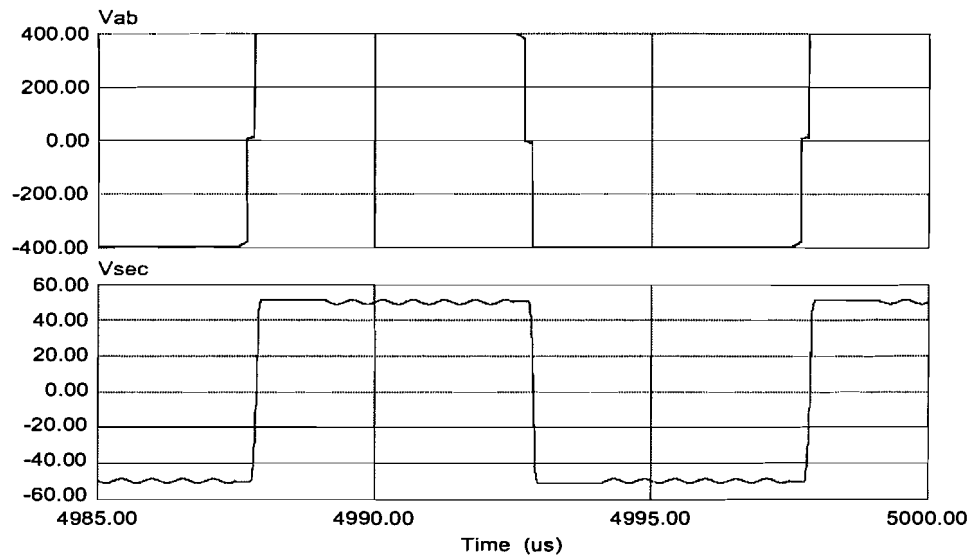


Figure 4.22: 1) Output voltage of converter bridge 2) Voltage across secondary side of transformer

The remaining key waveforms are depicted in figure 4.23.

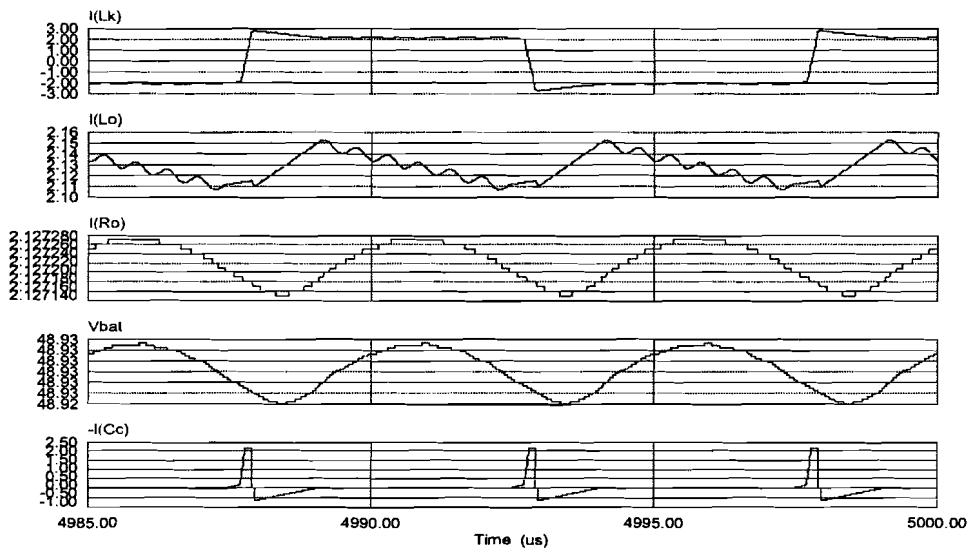


Figure 4.23: 1) Leakage inductance current 2) Current through output inductor 3) Charging current to battery 4) Battery voltage 5) Current through active clamp capacitor

Finally, the voltage across and the current through one switch of a converter leg is shown in figure 4.24.

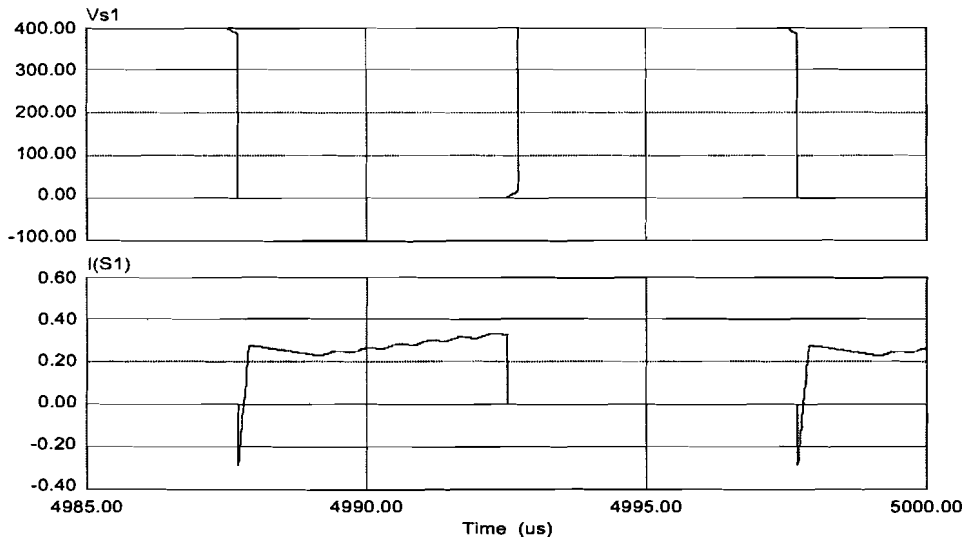


Figure 4.24: 1) Voltage ( $V_{ds}$ ) across  $S_5$  2) Current through  $S_5$

## 4.6 Charging mode operation with synchronous rectification

Because the low voltage side switches are implemented with Mosfets with low on resistance, synchronous rectification can be used to reduce the conduction loss with little effort.

For the synchronous rectification operation,  $S_1$  and  $S_2$  are always on simultaneously activated during the positive duty cycle ( $V_{ab} > 0$ ) while  $S_3$  and  $S_4$  are simultaneously activated during the negative duty cycle ( $V_{ab} < 0$ ). During the off duty cycle, all bridge switches are on to reduce the conduction loss. All bridge switches need to be turned off when  $S_c$  is on. This is important to prevent shoot through of the bridge switches. The control logic expression to realize the synchronous rectification is as follows:

$$S_1, S_2 = (S_5 + S_6) \bullet \overline{S_c} \quad (4.17)$$

$$S_3, S_4 = (S_7 + S_8) \bullet \overline{S_c} \quad (4.18)$$

In the real circuit, a dead time is needed between the turn-off of  $S_c$  and turn-on of  $S_1$  through  $S_4$ , which can prevent the shoot through problem. The timing of  $S_1, S_2$  is shown in figure 4.25. The current flowing through the Mosfet is also illustrated in figure 4.25 i.e.  $I_{s1}$ . It is assumed that when the Mosfet is on, all the current will flow through the Mosfet instead of its anti-parallel diode.

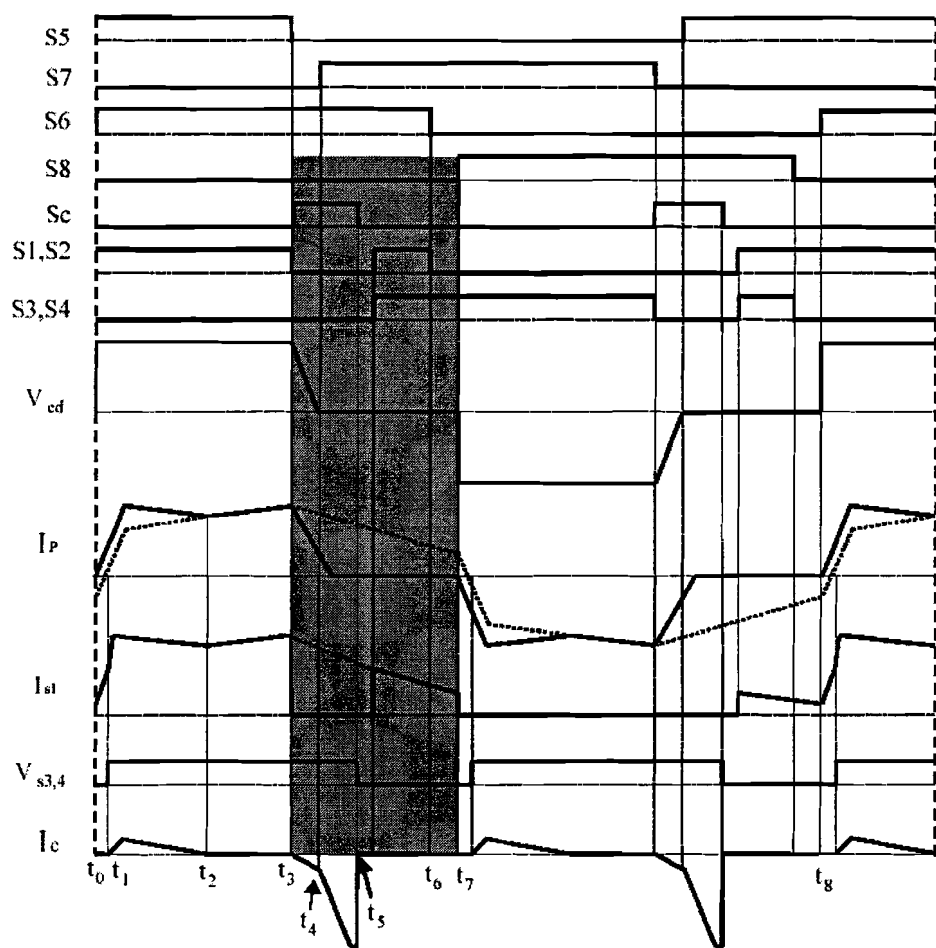


Figure 4.25: Typical waveforms of the converter with synchronous rectification

# Chapter 5

## Power stage design

### 5.1 Introduction

This chapter presents the power stage design of the bi-directional DC-DC converter in both discharging mode and charging mode.

First of all, the design of the magnetic components will be described. The maximum battery discharge current is much larger than the maximum battery charge current. Therefore, the ratings of the magnetic components of the bi-directional DC-DC converter will be determined based on the discharging mode of operation at full load, namely  $1kW$ .

Furthermore, the power ratings of the components both in discharging mode and charging mode are determined after which the required components are selected.

### 5.2 Magnetic design

#### 5.2.1 Magnetic design using Magtool

For designing magnetic components there are several guidelines available in literature. One of these design guidelines is described in [7]. With the aid of certain formulas, design parameters for the magnetic components could be derived.

Besides the general design guideline given in [7] there was the possibility of using the numerical software program Magtool. Magtool is a computer program for designing magnetic components.

#### 5.2.2 Transformer design using Magtool

The transformer provides galvanic isolation between the battery side and the load side of the converter. It manages all the power transferred between the battery and the high side link. The transformer should be designed for the maximum power required to the load, namely  $1kW$ .

Before starting using Magtool, the magnetizing inductance ( $L_m$ ) and the transformer ratio  $n = N_p/N_s$  should be known. Furthermore, the worst-case current for the transformer using PSIM is depicted in figure 5.1.

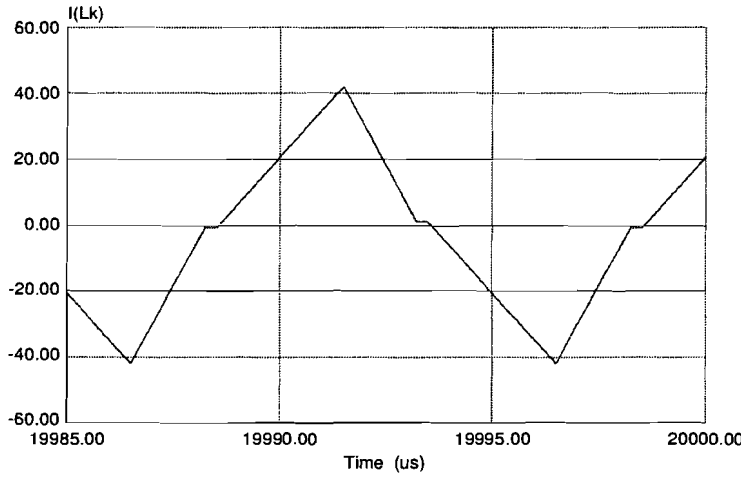


Figure 5.1: Current through primary side of transformer

Since the converter operates at a frequency of  $F_s = 100\text{kHz}$ , the transformer is optimized for this operating frequency. The high operating frequency requires the choice of a proper magnetic material, whose frequency related losses are acceptable at the operating frequency.

The area product approach is used to choose the size of the transformer core. The result of the area product approach is a reference criterion for the core choice. This approach uses some reference material data that are obtained from the following considerations:

- Input voltage: the primary side input is a square-wave with maximum voltage equal to  $V = 80V$  (boosted battery voltage). The frequency of the square-wave is  $100\text{kHz}$  and the duty cycle is assumed to be  $D = 0.6$ .
- Thermal matters limit the utilization of materials. For a first analysis, the copper current density in the windings is assumed cautiously equal to  $200\text{A/cm}^2$ . The saturation flux density of most of the regular ferrites doesn't exceed  $0.5T$  at room temperature. Wishing to operate in the linear section of the B-H curve and foreseeing an operating temperature higher than room temperature, a cautious maximum value of the flux density equal to  $B_M = 0.2T$  is assumed.
- According to figure 5.1, the primary windings are to be designed to carry a  $48\text{A}$  current whereas the secondary windings are to be designed to carry  $6\text{A}$  current.
- Constructive parameters: the geometrical parameter  $K_u$ , equal to the ratio of copper area and winding area, accounts for the copper-filling factor. This parameter is cautiously assumed to be equal to 0.3.

In order to estimate the size of the core, a formula for the  $K_g$  factor from [7] has been used. Instead of  $R_{dc}$  an estimate for the copper losses has been made.

$$K_g \geq \frac{\rho L_m^2 I_{max}^2 I_{rms}^2}{B_{max}^2 K_u P_{cu}} \quad (5.1)$$

With  $\rho = 2.208 \cdot 10^{-8}$ ,  $B_{max} \leq 200mT$ ,  $K_u = 0.3$ , and  $P_{cu} = 1W$ .

After considering above parameters and taken the availability of materials into account, the PQ50/50 appeared to be the best choice for the application. Furthermore the 3C94 has been chosen as core material.

The wire choice has been litz wire. The design has been optimized by using more wires in parallel. Table 5.1 below lists the design parameters that are used for the core design.

$L_m$	$I_{max}$	$I_{rms}$	$n_p$	$n_s$	$K_g$	Core	Core material
$200\mu H$	48A	28A	6	48	0.13	PQ50/50	3C94

Table 5.1: Design parameters transformer core

The design results for the transformer that are obtained by using Magtool are given in table 5.2. The complete results from Magtool are included in Appendix C.

$L_m$	200 $\mu H$
$N_p/N_s$	0.125
Core	PQ50/50
Airgap1	0.037mm
Airgap2	0.037mm
Number of turns $L_p$	6
Number of turns $L_s$	48
Wire $L_p$	160 * 0.071mm 5 in parallel.
Wire $L_s$	250 * 0.071mm
$P_{tot}$	9.946W
$B_{sat}$	382mT

Table 5.2: Magtool design results of transformer

The transformer has been designed and the magnetizing inductance and the leakage inductance turned out to be as follows:

- $L_m = 130\mu H$
- $L_k = 900nH$

That means that a lumped inductor of  $L_k = 1.2\mu H$  is needed in series with the primary side of the transformer.

### 5.2.3 Inductor design using Magtool

Before getting started with designing an inductor using Magtool, the value of the inductor should be known first. Then, in order to design the magnetic components in an efficient way, the worst case current waveforms, i.e. the maximum currents, and the maximum switching frequency should be determined.

After doing so, an initial core size selection could be made based on the following formula in [7]:

$$K_g = \frac{L^2 I_{max}^2 \rho}{B_{max}^2 R_{dc} K_u} \quad (5.2)$$

With:

$$R_{dc} = \rho \frac{nMLT}{A_w} \quad (5.3)$$

Where:  $L$  the inductor value,  $I_{max}$  the peak current through the inductor,  $\rho$  the resistivity of the inductor,  $B_{max} < B_{sat}$  the maximum tolerable flux density,  $K_u < 1$  the fill factor,  $N$  the number of turns,  $MLT$  the mean length per turn, and  $A_w$  the cross sectional area of the inductor.

After deriving the required  $K_g$  factor, Appendix D of [7] can be applied to select the corresponding core that can be chosen for the design. During this process, also the core material has to be selected. It should be noticed that the core material depends on the working frequency.

After choosing the core size and the core material, the next step is to design the winding layout. By setting the core and the core material in Magtool, this program calculates the available winding area after which the minimum and maximum number of turns is given.

The minimum number of turns is dependent on the  $B_{max}$  of the selected core whereas the maximum number of turns is dependent on the maximum airgap possible according to the following formulas:

$$nI_{max} = B_{max} \frac{l_{gap}}{\mu_0} \quad (5.4)$$

$$BA_e n = LI_{max} \quad (5.5)$$

From these two formulas an expression for the inductor,  $L$  can be derived and is as follows:

$$L = \frac{n^2 \mu_0 A_e}{l_{gap}} \quad (5.6)$$

As can be seen, by adjusting the airgap (the bigger the airgap, the smaller the inductor), the desired inductor value can be obtained.

Finally, the wire type should be chosen after which Magtool calculates the design parameters such as the flux density in the core, the winding area, the airgap, the temperature rise and the losses. After this process, the design can be optimized further.

### 5.2.4 Inductor design

Now that the inductor design using Magtool has been described, the inductors will be designed based on the ideal inductor values together with the worst case currents. The ideal inductor values are derived in paragraph 4.3.4 and are as follows:

- $L_1 = 2\mu H$
- $L_2 = 6\mu H$
- $L_k = 1.2\mu H$

The worst-case currents through the inductors are simulated with PSIM and are given in the figures below.

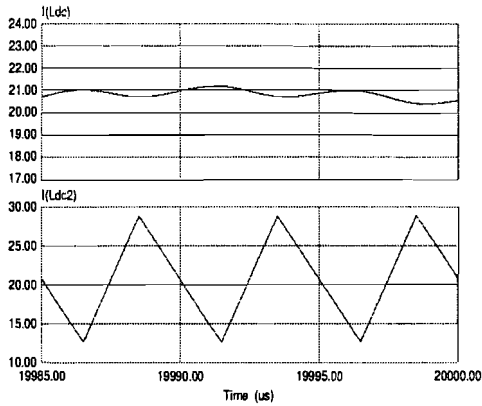


Figure 5.2: Current through  $L_1$ ,  $L_2$  respectively

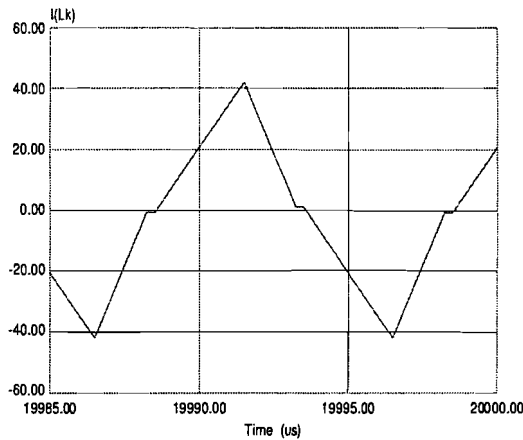


Figure 5.3: Current through  $L_k$

The inductors are designed with the aid of the design procedure described in section 5.2.3. In order to estimate the core sizes, the following formula in [2] has been used. And again, since  $R_{dc}$  is not known a priori, an estimate has been made for the copper losses.

$$K_g = \frac{L^2 I_{max}^2 \rho}{B_{max}^2 R_{dc} K_u} \quad (5.7)$$

With  $\rho = 2.208 \cdot 10^{-8}$ ,  $B_{max} \leq 300mT$ ,  $K_u = 0.3$ , and  $P_{cu} = 1W$ .

Table 5.3 lists the design parameters that are used for the core design.

$L$	$I_{max}$	$I_{rms}$	$K_g$	Core	Core material
$L_1 = 2\mu H$	24A	24A	0.0035	PQ20/16	3C96
$L_2 = 6\mu H$	30A	22A	0.028	PQ26/20	3C96
$L_k = 1.2\mu H$	45A	28A	0.0040	PQ20/16	3C96

Table 5.3: Design parameters for the inductor's cores

After designing the inductors with Magtool, there was the possibility of using different types of cores. However, because of the availability of the PQ-type series the choice was quite obvious. Furthermore, the choice of the core material 3C96 for a switching frequency of 100kHz is quite common. Table 5.4 shows the design results for the inductors using Magtool. The complete Magtool results are included in Appendix D, E and F.

Inductor	$L_1 = 2\mu H$	$L_2 = 6\mu H$	$L_k = 1.2\mu H$
Core	PQ20/16	PQ26/20	PQ20/16
Core material	3C96	3C96	3C96
Airgap	0.878mm	1.802mm	0.839mm
Number of turns	4	7	3
Wire	300 * 0.071mm	250 * 0.071mm	300 * 0.071mm
$P_{tot}$	3.907W	9.908W	5.916W
$B_{max}$	242.2mT	248.0mT	281.9mT
$B_{sat}$	417.0mT	381.0mT	407.0mT

Table 5.4: Magtool design results of inductors

Now that the design of the magnetic components has been described, the power component design of the bi-directional DC-DC converter in both discharging mode and charging mode will be described in the next paragraphs.

## 5.3 Power component design

### 5.3.1 Discharging mode

The power components in this section are designed with the following system parameters:

DC link power	$P_{dc} = 1kW$
Switching frequency	$F_s = 100kHz$
Input voltage (battery)	$V_{bat} = 48V$
DC link voltage	$V_{dc} = 400V$
Transformer turns ratio	$N_p : N_s = 1 : 8$

Table 5.5: System parameters in discharging mode

The power stage design for the active-clamp boost converter (discharging mode) is shown in Figure 5.4. The choice of the components will be described in the following sections.

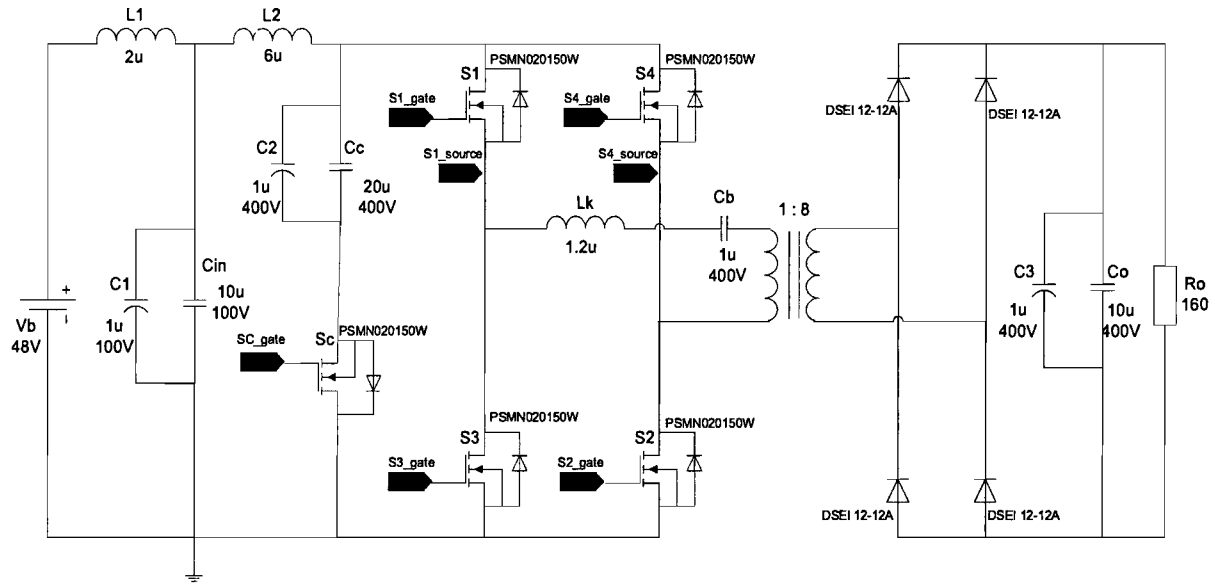


Figure 5.4: Power stage component selection

The voltage and current ratings of the Mosfets and diodes are determined based on the worst case scenario. That means that these ratings are calculated on the moment at which the converter is operating at full load, i.e.  $1\text{ kW}$ .

### Diodes

When the battery voltage is  $48V$ , the output voltage is  $400V$ . As the secondary winding voltage becomes  $400V$ , the peak voltage of a rectifier diode is  $400V$  as well. Considering ringing phenomenon's at the secondary side of the high frequency transformer a diode with a higher voltage rating has to be chosen.

Furthermore, an ultra-fast recovery diode need to be chosen to decrease the switching loss caused by the high switching frequency. The maximum current at the DC link is  $5A$  (peak value). As the diode always conducts half of a switching cycle, the average current rating of the diode can be obtained as follows:

$$I_{D,av} = \frac{1}{2} I_{dc} = 2.5A \quad (5.8)$$

The peak current of the diode is equal to the peak value of the output current and is as follows:

$$I_{D,peak} = I_{dc,peak} = 5A \quad (5.9)$$

Therefore, an ultra-fast recovery diode with a rating of  $1200V$ ,  $11A$  was selected.

### Mosfets

Since the switches in discharging mode should operate at low voltage and high current, power Mosfets with high current rating and low on-state resistance are selected.

When the battery voltage is  $48V$ , the up converter consisting of the input inductor and active clamp branch boosts this input voltage. In case of a duty cycle of  $D = 0.6$ , the voltage across the active clamp switch  $S_c$  and the four bridge switches  $S_1 - S_4$  becomes:

$$V_{mosfet} = \frac{V_{bat}}{D} \quad (5.10)$$

This results in:

$$V_{mosfet} = \frac{V_{bat}}{D} = 80V \quad (5.11)$$

Considering a safety margin due to voltage spikes and the possibility to decrease the duty cycle, a device voltage rating of  $150V$  should be acceptable.

The average and peak value of the Mosfets current are about  $20A$  en  $40A$  respectively and were calculated by multiplying the average and peak value of the diodes by the transformer's turns ratio.

The current rating of the active clamp switch  $S_c$  is much lower than the bridge switches, however, a Mosfet with the same ratings has been used because of the availability. For the sake of completeness, table 5.6 below shows the selected power switches with the corresponding ratings.

Component	Current rating	Voltage rating	Selected device
NMosfet ( $5\times$ )	$73A$	$150V$	Philips,PSMN020-150W, $R_{ds(on)} = 20m\Omega$
Diode ( $4\times$ )	$11A$	$1200V$	Ixys,Dsei12-12A, $t_{rr} = 50ns$

Table 5.6: Voltage and current ratings of the selected power switches

The choice of the active clamp capacitor  $C_c$  of  $20\mu F$  and the input capacitor  $C_{in}$  of  $10\mu F$  has been determined in chapter 4. The  $10\mu F$  electrolytic capacitor forms the output bulk capacitor  $C_o$ . In order to make use of electrolytic capacitors with high capacitor values, it is necessary to place plastic capacitors in parallel with the electrolytic capacitors. Plastic capacitors are able to handle higher currents, which are common in this application. For this reason,  $1\mu F$  plastic capacitors are placed in parallel with the elco's. Furthermore, the DC-blocking capacitor has chosen to be  $400V$ ,  $1\mu F$ .

### 5.3.2 Charging mode

Since all components, except for the Mosfets, should be equal in discharging mode as well as in charging mode, in this section only the selection of the Mosfets will be described. These components are designed with the following system parameters:

Battery charging power	$P_{bat} = \pm 100W$
Switching frequency	$F_s = 100kHz$
DC link voltage	$V_{dc} = 400V$
Battery voltage	$V_{bat} = 48V$
Transformer turns ratio	$N_p : N_s = 1 : 8$

Table 5.7: System parameters in charging mode

The power stage design for the phase shifted buck converter (charging mode) is shown in Figure 5.5. The choice of the components will be described in the following sections. As the power in charging mode is only about 100W, the benefits of using the secondary active clamp are negligible. That means that the active-clamp Mosfet  $S_c$  is permanently turned on during charging mode in this application. The advantages of using the secondary active clamp that are described in paragraph 4.5 are especially attractive for high power applications ( $\geq 1kW$ ).

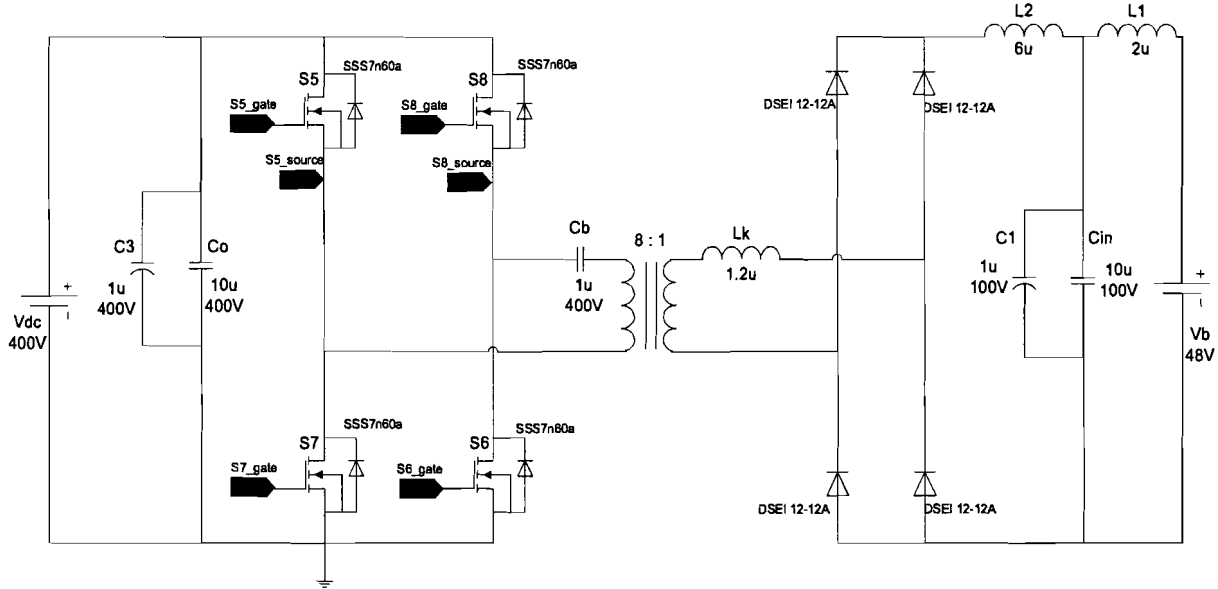


Figure 5.5: Power stage component selection

### Mosfets

The switches in charging mode should operate at high voltage and low current, therefore power Mosfets with high voltage rating and an acceptable on-state resistance are selected. When the DC-link voltage is at a maximum voltage of  $400V$ , the voltage across the Mosfets  $S_5 - S_8$  becomes  $400V$ . Furthermore, as the power transfer is only  $100W$  the current through the Mosfets is very small. Considering a safety margin due to voltage spikes a device voltage rating of  $600V$  should be acceptable. Table 5.8 lists the power switches used in charging mode with their corresponding ratings.

Component	Current rating	Voltage rating	Selected device
NMosfet ( $4 \times$ )	$4A$	$600V$	Samsung,SSS7n60a, $R_{ds(on)} = 1\Omega$
Diode ( $4 \times$ )	$11A$	$1200V$	Ixys,Dsei12-12A, $t_{rr} = 50ns$

Table 5.8: Voltage and current ratings of the selected power switches

# Chapter 6

## Design of open loop control circuit

### 6.1 Introduction

This chapter describes the open loop control of the bi-directional DC-DC converter in both discharging mode and charging mode. For the sake of completeness, the power circuits of the bi-directional DC-DC converter in chapter 5 and the control circuits that will be described in this chapter are included in Appendix G and H.

### 6.2 Discharging mode

#### 6.2.1 Control signals

There are several options for creating a Pulse Width Modulation (PWM) signal to be used for the control circuit. After a study, the LM3524 has been chosen to generate the PWM signals used for the Mosfets.

Figure 6.1 shows the circuit used for this application. The LM3524 provides two dependent,  $180^\circ$  phase shifted PWM signals that are suitable for the bi-directional DC-DC converter in discharging mode.

Setting the switching frequency of the Mosfets occurs by means of the integrated oscillator. By varying  $R_t$  and  $C_t$  the switching frequency can be regulated and is as follows:

$$f_s = \frac{1}{R_t C_t} \quad (6.1)$$

A potentiometer of  $5k\Omega$  and a capacitor of  $2.2nF$  set the switching frequency of  $100kHz$ . Furthermore, the duty cycle of the output PWM signals is set by the potentiometer  $R_{comp}$  of  $5kHz$ .

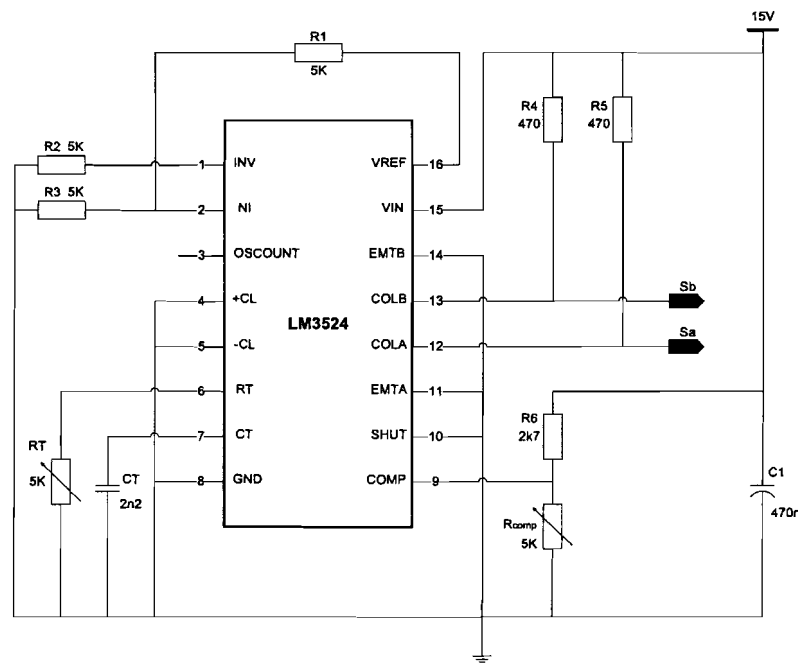


Figure 6.1: Circuit used for implementing PWM signals

The output signals of the above circuit are depicted in figure 6.2.

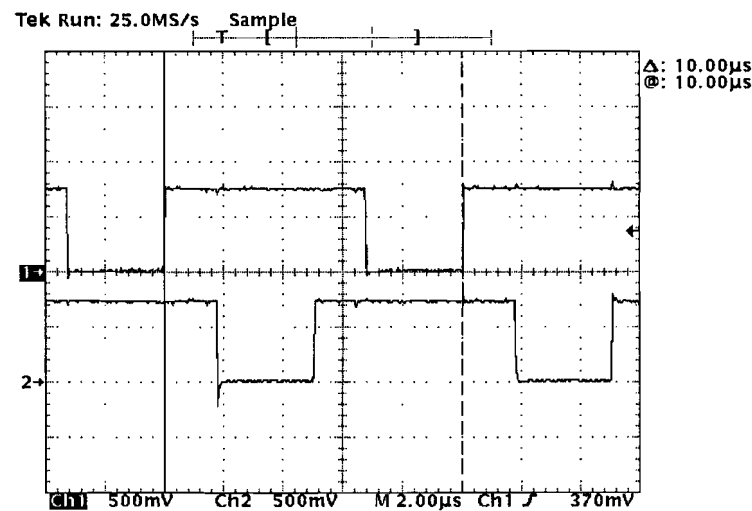


Figure 6.2: Ch1: S<sub>a</sub> 10V/div. Ch2: S<sub>b</sub> 10V/div.

The control signal of the active clamp  $S_c$  switch is provided by the circuit that is depicted in figure 6.3. As the active clamp switch  $S_c$  is turned on when one of the switch pair diagonals is off, its PWM signal is implemented by using a XOR port, the HEF4030BP. The inputs of the XOR port are  $S_a$  and  $S_b$ .

Furthermore, a deadtime generator block consisting of  $RC$  networks with NAND ports is implemented to introduce deadtimes between the signals to avoid short-circuiting in the converter.

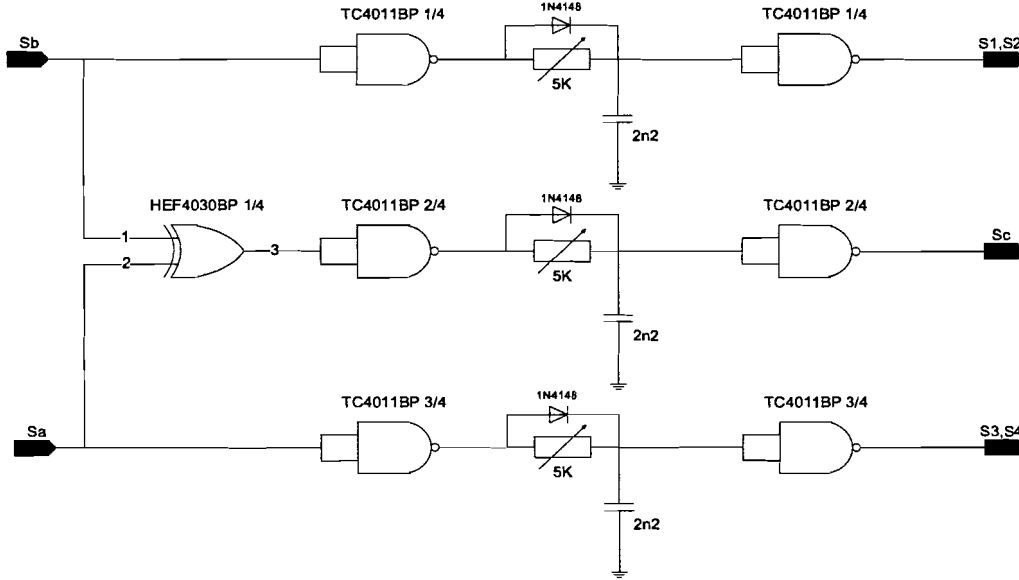


Figure 6.3: Control circuit of  $S_c$  including deadtime circuit

The control signal for the active clamp switch is depicted in figure 6.4. It should be noticed that the switching frequency of this signal is twice that of the bridge switches, namely  $200\text{kHz}$ .

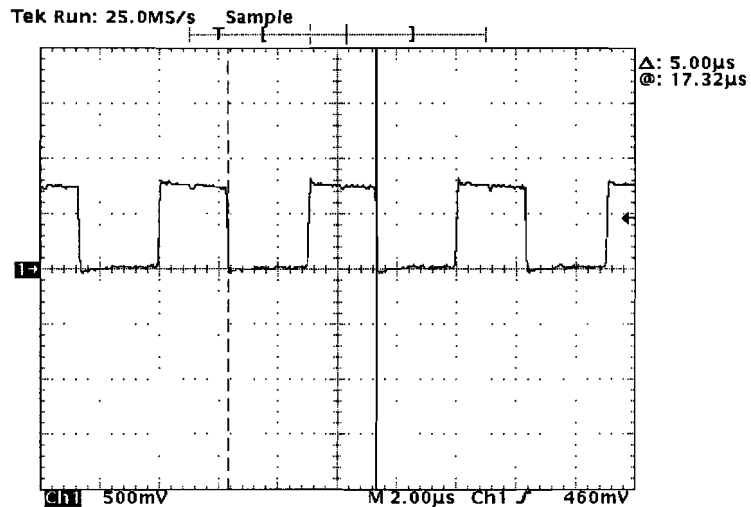


Figure 6.4: Ch1:  $S_c$  10V/div.

### 6.2.2 Power Mosfet driver

Figure 6.5 shows the driver circuit that is used to drive the Mosfets  $S_1$  and  $S_2$  whereas the Mosfet driver circuit of  $S_3$  and  $S_4$  is depicted in figure 6.6.

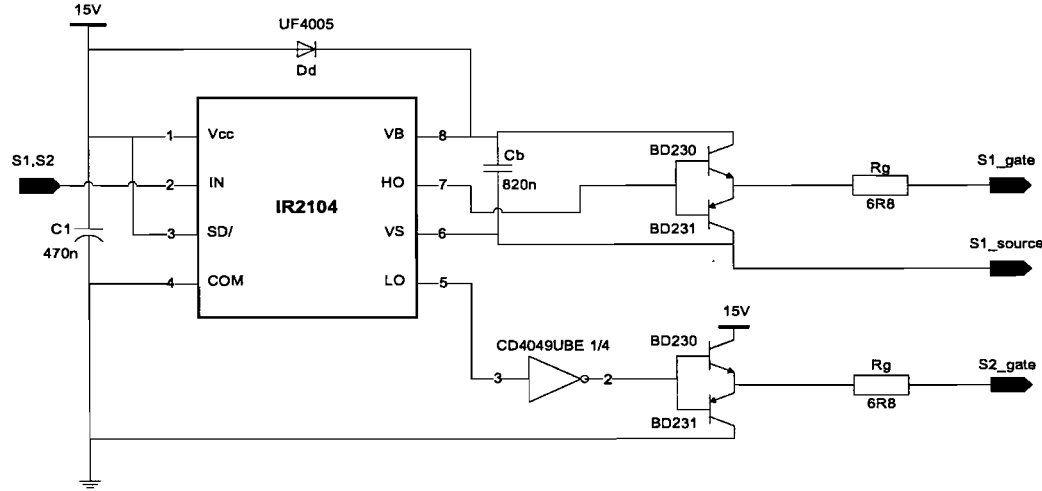


Figure 6.5: Mosfet driver circuit of  $S_1$  and  $S_2$

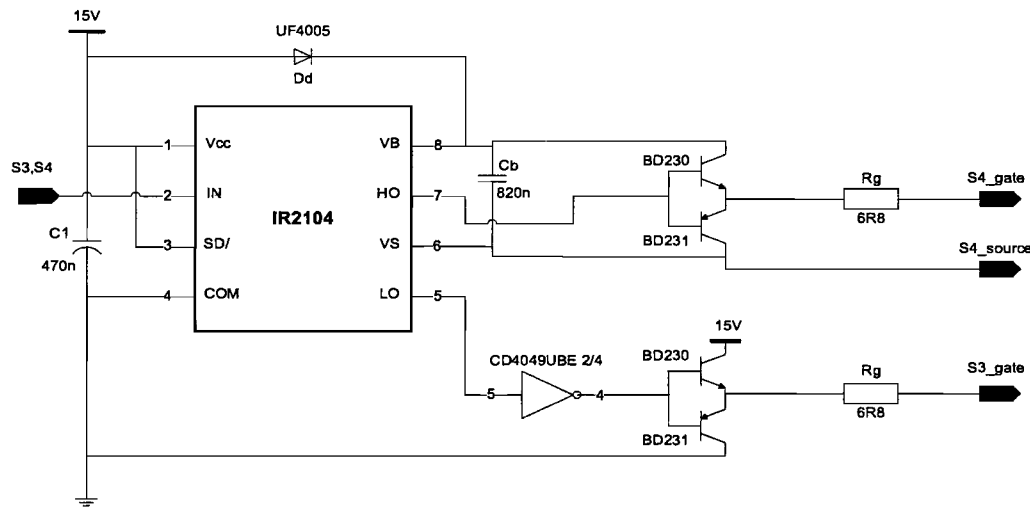


Figure 6.6: Mosfet driver circuit of  $S_3$  and  $S_4$

The IR2104 is a half-bridge driver with dependent high and low side referenced output channels that can be used as high voltage, high speed power Mosfet driver. The floating

channel can be used to drive an N-channel power Mosfet in the high side configuration, which operates up to 600V.

The IR2104 consists of one input to which the output of the LM3524 is connected and two outputs that drive the half-bridge Mosfets in turn with  $V_{gs} = V_{cc}$  (on) and  $V_{gs} = 0$  (out). The deadtime between the turn-on of one switch and the turn-off of the other switch is about 520ns. The deadtime is necessary to prevent short-circuit.

The low side Mosfet ( $ML$ ) of the bridge is driven by output  $LO$  (pin 5). Since the low side Mosfet is directly connected to ground, a direct connection can be made to the source of the power device for the return of the gate drive current.

The high side Mosfet ( $MH$ ) on the other hand, is either connected to ground or to the high voltage side,  $V_{dc}$ . When the Mosfet is connected to ground no special facilities are needed. However, when the high side Mosfet is connected to  $V_{dc}$ , the gate voltage would have to be 10V – 15V higher than the rail voltage ( $V_{dc}$ ), which is frequently the highest voltage available in the system. The gate voltage must be controllable from the logic, which is normally referenced to ground. Thus, the control signals have to be level-shifted to the source of the high side power device, which in most applications swings between two rails.

In the past this process has been realized by applying a floating  $V_{gs}$ . However, this solution requires a special galvanic separated supply, which is quite expensive. This IC (IR2104) provides an alternative solution.

The gate charge for the high side Mosfet is provided by the bootstrap capacitor that is charged by the 15V supply through the bootstrap diode during the time when the device is off (assuming that  $V_s$  swings to ground during that time, as it does in most applications).

The bootstrap diode and capacitor are the only external components strictly required for operation in a standard PWM application. The local decoupling capacitor placed between the supply  $V_{cc}$  and the ground  $COM$  is useful in practice to compensate for the inductance of the supply lines.

## Selection of Bootstrap components

### Bootstrap capacitor

The voltage seen by the bootstrap capacitor is the  $V_{cc}$  supply only. This capacitor should be large enough to charge the gate capacitor while sustaining a certain voltage level. This means the following:

$$i_g = C_{bs} \frac{dV}{dt} \quad (6.2)$$

$$C_{gs} \leq C_{bs} \frac{0.01 \cdot 15}{dt} \quad (6.3)$$

That means that:

$$C_{bs} \geq 100C_{gs} \quad (6.4)$$

From the specifications stated in the datasheet of the PSMN020-150W it was concluded that  $C_{gs} \approx 7nF$ . Therefore,  $C_{bs}$  was chosen to be  $820nF$ .

### Bootstrap diode

The bootstrap diode must be able to block the full voltage in the specific circuit. This occurs when the high side Mosfet is on and is about equal to the voltage across the power rail. The current rating of the diode is the product of gate charge times the switching frequency. The high temperature leakage characteristic of this diode can be an important parameter in those applications where the capacitor has to hold the charge for a prolonged period of time. For this reason it is important that this diode be ultrafast recovery to reduce the amount of charge that is fed back from the bootstrap capacitor into the supply.

As ultrafast recovery diode that meets these requirements, a UF4005 with a voltage according to the bridge voltage has been chosen.

The gate of a Mosfet appears purely capacitive, so no gate drive current is needed in the steady state, unlike transistors. However, a high current low impedance drive circuit is needed to inject or remove current from the gate and slew  $V_{gs}$  in order to switch the device rapidly. The gate drive, although small, can require significant charge as the drain voltage slews (the Miller effect )[6].

If the required gate current of the Mosfet,  $I_g$  is less than the  $I_g$  (peak) rating of the driver (IR2104) then, the gate driver output current is adequate for the application. If not, we must either accept higher losses (which would occur due to longer transition times of the Mosfet) or, we must buffer the output of the gate driver for example using a totem pole configuration to provide sufficient current to drive the Mosfet.

From the datasheet of the IR2104 it was concluded that the gate driver output current is about  $200mA$ . The time in which the gate of the Mosfet is charged is derived as follows:

$$I_g = C_{gs} \frac{dV}{dt} \quad (6.5)$$

$$dt = \frac{6.5 \cdot 10^{-9} \cdot 15}{0.2} \approx 490ns \quad (6.6)$$

From the datasheet of the PSMN020-150W one can conclude that the turn-on delay time is about  $50ns$ . Therefore, a totem pole configuration has been chosen to avoid high losses:

$$I_g = C_{gs} \frac{dV}{dt} \quad (6.7)$$

$$I_g = \frac{6.5 \cdot 10^{-9} \cdot 15}{50 \cdot 10^{-9}} \approx 2A \quad (6.8)$$

Thus, the resistor  $R_g$  can be determined as follows:

$$R_g = \frac{15}{2} = 7.5\Omega \quad (6.9)$$

For the Mosfet driver circuit a resistor of  $6.8\Omega$  has been selected.

The isolated gate drive of the active clamp Mosfet,  $S_c$  is provided by the circuit depicted in figure 6.7.

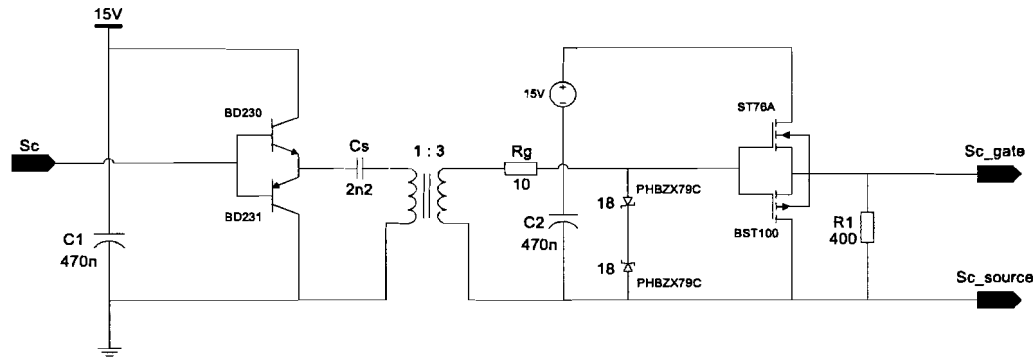


Figure 6.7: Mosfet driver of  $S_c$

The most common method of isolating the Mosfet gate from the driving control circuit is making use of a pulse transformer. Furthermore, a DC-blocking capacitor is usually placed in series with the primary side of the transformer.

The simple addition of a zener diodes on the secondary can be used to restore the correct DC offset on the signal. As mentioned earlier, to provide sufficient current to drive the Mosfet, a totem pole consisting of two small Mosfets has been chosen. As the on state resistance of the totem pole Mosfets is about  $7\Omega$ , no additional gate resistor has been added. Finally, a galvanic separated supply has been used to provide  $15V$ .

The gate source voltages of the Mosfets are measured on the PCB and are depicted in figure 6.8. In order to compare the patterns, the same signals are shifted up and shown in figure 6.9.

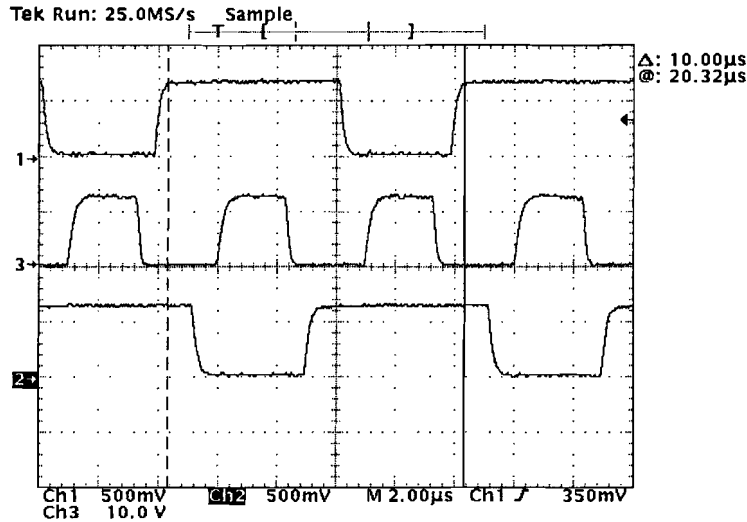


Figure 6.8: **Ch1:**  $V_{gs}$  of  $S_1$ ,  $S_2$  10V/div **Ch2:**  $V_{gs}$  of  $S_2$ ,  $S_4$  10V/div **Ch3:**  $V_{gs}$  of  $S_c$  10V/div

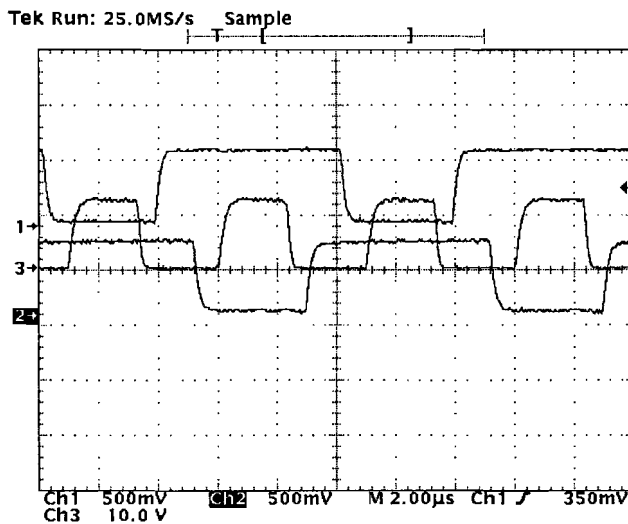


Figure 6.9: **Ch1:**  $V_{gs}$  of  $S_1$ ,  $S_2$  10V/div **Ch2:**  $V_{gs}$  of  $S_2$ ,  $S_4$  10V/div **Ch3:**  $V_{gs}$  of  $S_c$  10V/div

## 6.3 Charging mode

### 6.3.1 Control signals

The open loop control of the phase shifted converter is provided by the control circuits that are depicted in figure 6.10 and figure 6.11. Each circuit allows the phase shift control of one converter leg providing a maximum phase shift of  $180^\circ$  between the two converter legs. By applying a saw tooth signal from an external function generator and a reference voltage ( $V_{comp}$ ) to the comparators and adding the output voltage of the comparator to the D-flip flop latches, phase shifted square wave signals are obtained.

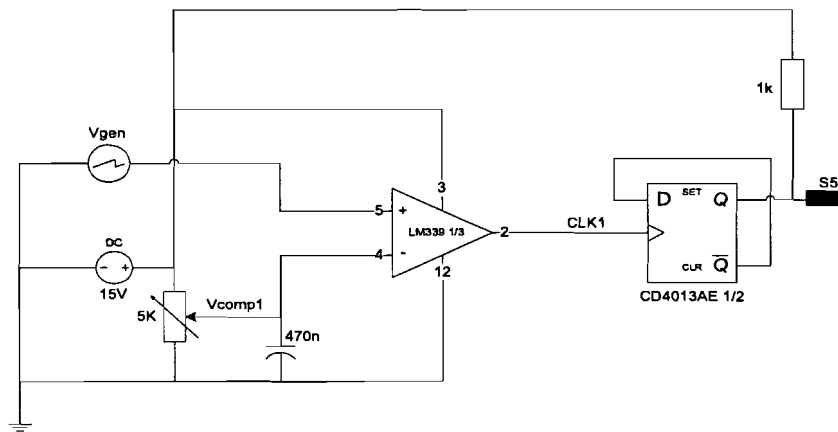


Figure 6.10: Phase shift control of converter leg 1

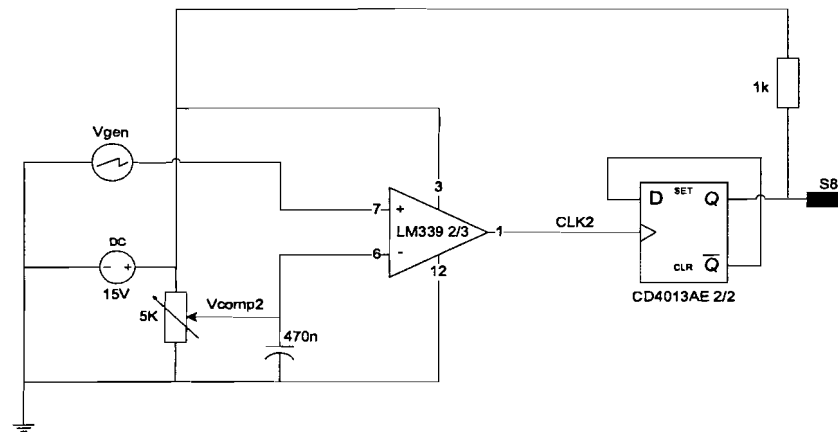


Figure 6.11: Phase shift control of converter leg 2

In order to illustrate this principle, the typical waveforms of the above circuits are shown in figure 6.12. By adjusting the values of the reference signals  $V_{comp1}$  and  $V_{comp2}$  the desired phase-shift between the two converter bridges can be obtained.

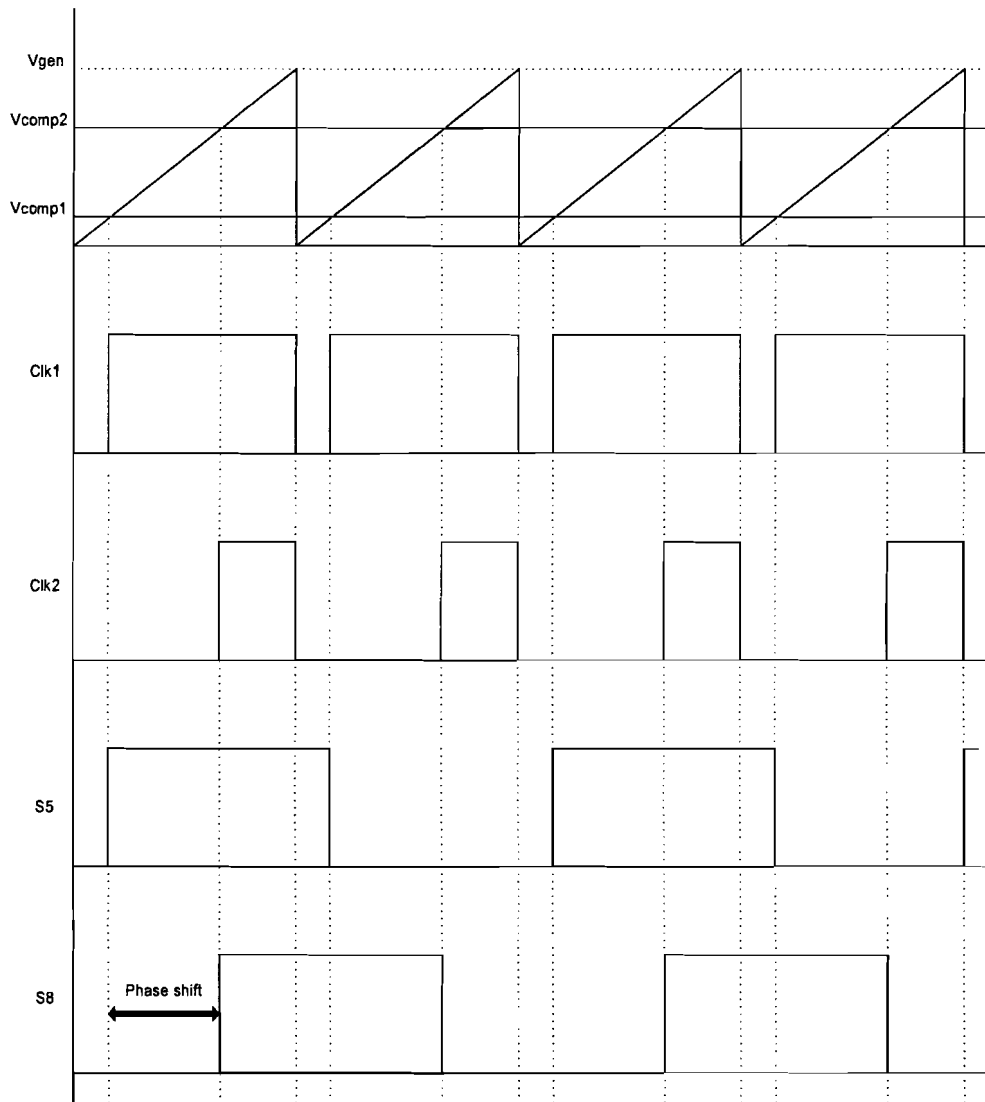


Figure 6.12: Signal waveforms of phaseshift generator

### 6.3.2 Power Mosfet driver

The Mosfets in the charging mode circuit are driven on the same way as described earlier in section 6.2.2. The main difference is that the gate source capacitance,  $C_{gs}$  of the SSS7n60a is much smaller. That leads to a smaller bootstrap capacitor  $C_{bs}$ , namely  $560nF$ . The Mosfet gate driver circuits are depicted in the figures below.

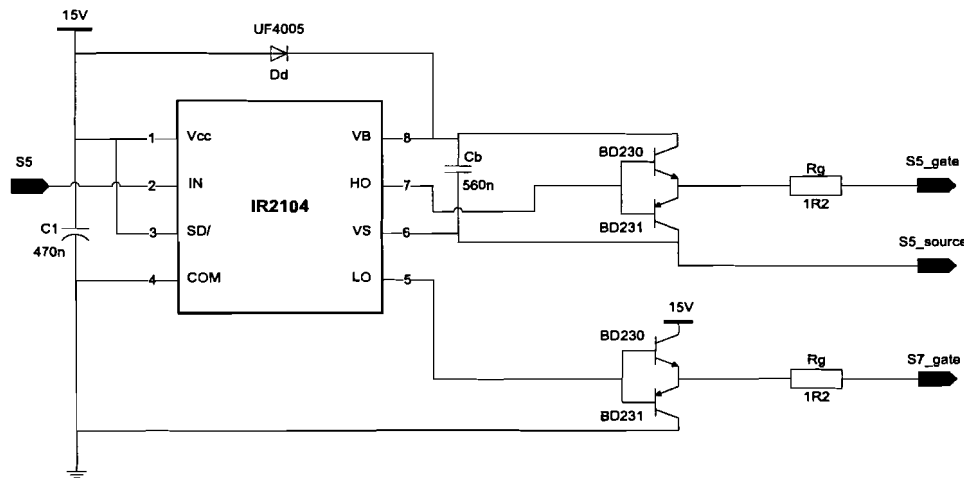


Figure 6.13: Mosfet driver circuit of  $S_5$  and  $S_7$

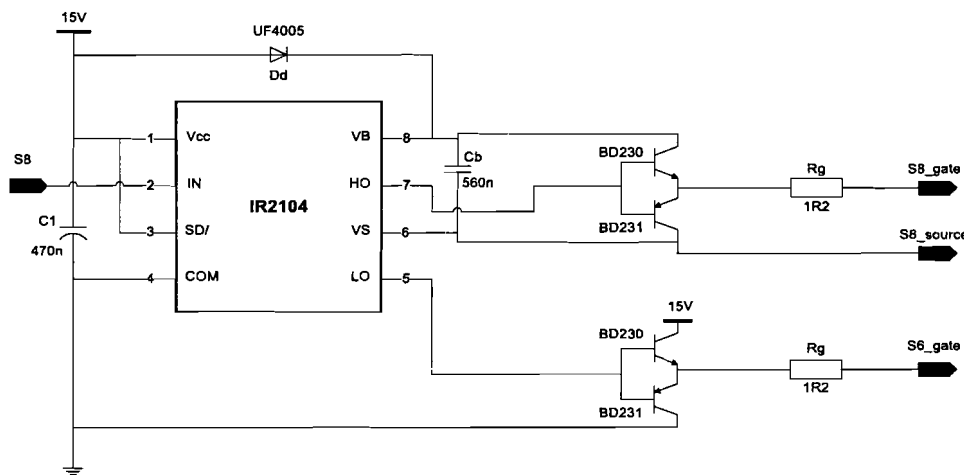


Figure 6.14: Mosfet driver circuit of  $S_8$  and  $S_6$

Figure 6.15 shows the complementary gate source signals ( $V_{gs}$ ) with deadtime of the two switches of one converter leg, whereas the phase shifted signals of the two converter bridges are depicted in figure 6.16.

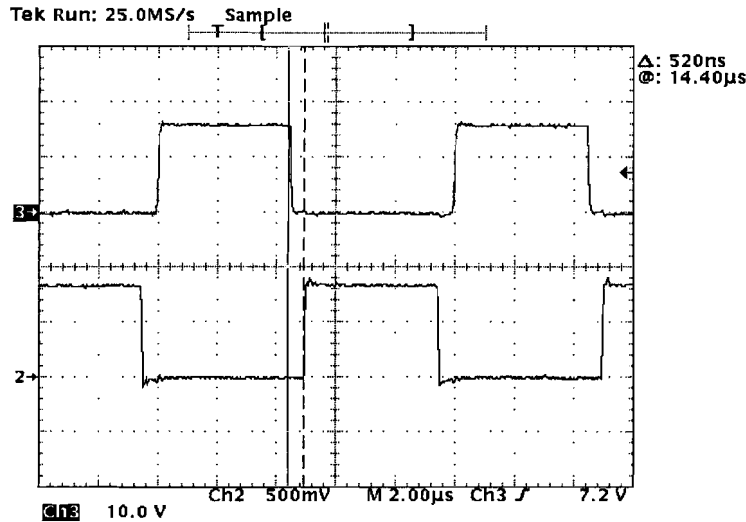


Figure 6.15: Control signals of one converter leg with dead time; **Ch2:**  $V_{gs}$  of  $S_5$  10V/div, **Ch3:**  $V_{gs}$  of  $S_7$  10V/div

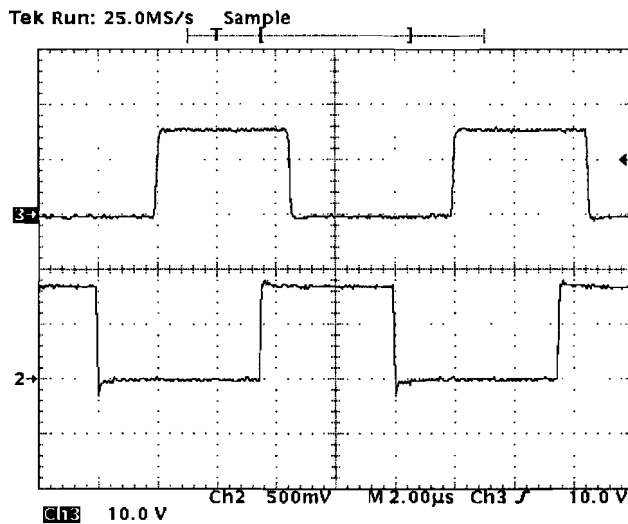


Figure 6.16: Phase shifted signals of the converter; **Ch2:**  $V_{gs}$  of  $S_5$  10V/div, **Ch3:**  $V_{gs}$  of  $S_8$  10V/div

# Chapter 7

## Experimental results

### 7.1 Introduction

This chapter presents the practical results of the bi-directional DC-DC converter. To provide experimental verification of the bi-directional DC-DC converter in discharging mode and charging mode, two PCB's were constructed. The Pcad schematic files of these PCB's are included in Appendix I and J.

### 7.2 Discharging mode

#### 7.2.1 Experimental waveforms

Figure 7.1 shows the bi-directional DC-DC converter in discharging mode. The important test points that are used to obtain the experimental waveforms that will be presented in this section are also shown in this figure.

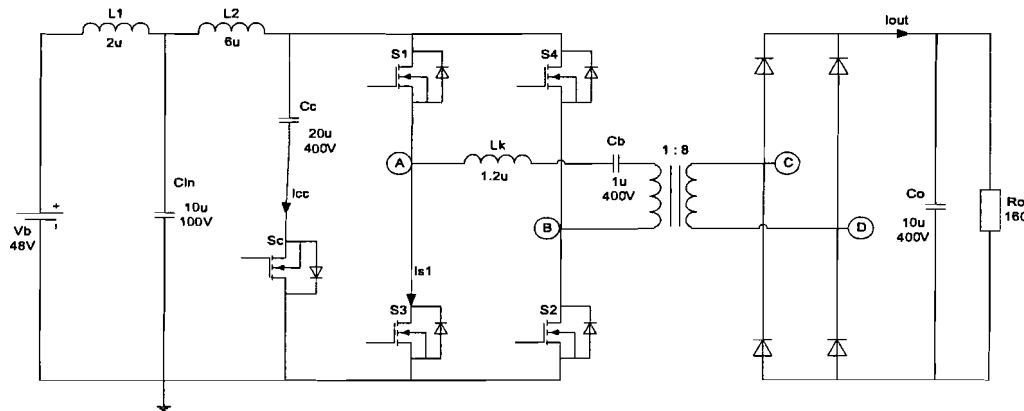


Figure 7.1: Converter in discharging mode with test points

The figures in the following section summarize the fundamental waveforms of the converter. Figure 7.2 shows the switching patterns of one bridge switch and the active clamp switch and the output voltage of the converter bridge.

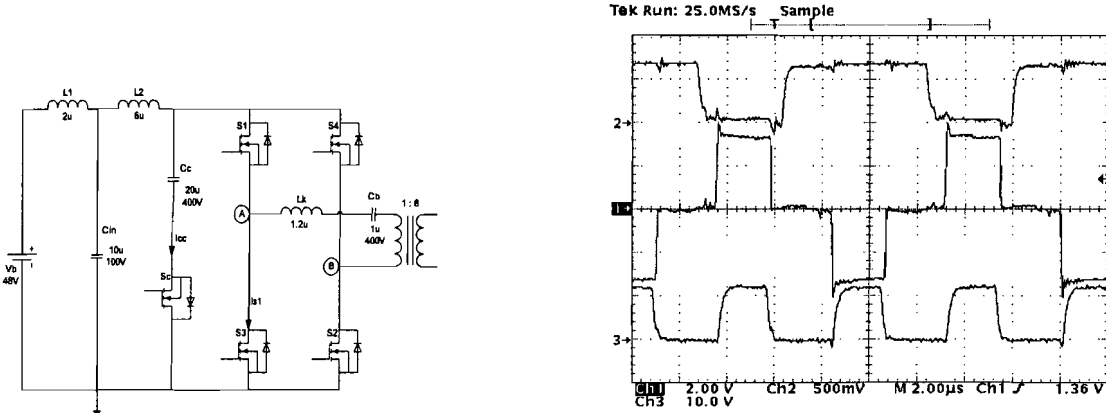


Figure 7.2: Ch1:  $V_{\text{bridge}}$  ( $V_{AB}$ ) 50V/div., Ch2:  $V_{gs}$  of  $S_1$  10V/div., Ch3:  $V_{gs}$  of  $S_c$  10V/div

The output voltage of the bridge is depicted in figure 7.3. As can be seen, the maximum value of  $V_{AB}$  is about 80V. It corresponds to the voltage across the active clamp branch. As the duty cycle  $D = 0.6$  and the input voltage  $V_{bat} = 48V$ , this value can be obtained as follows:

$$V_{AB} = \frac{V_{bat}}{D} \quad (7.1)$$

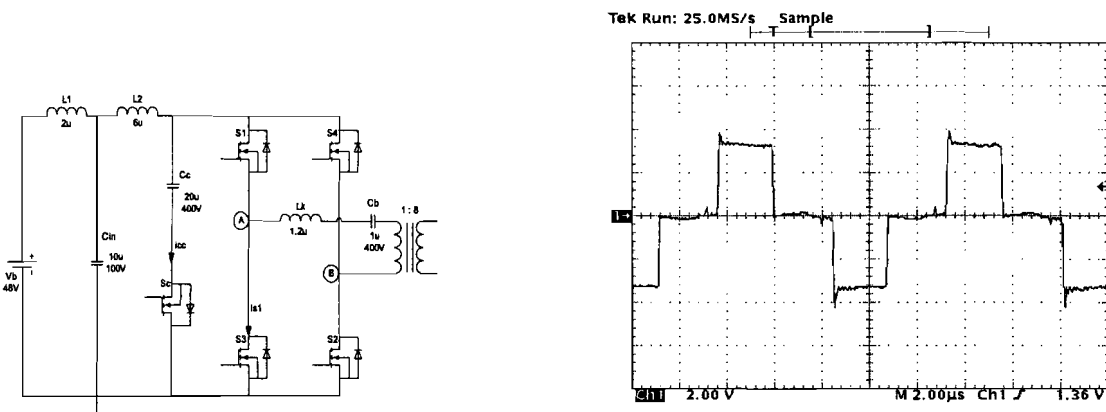


Figure 7.3: Ch1:  $V_{\text{bridge}}$  ( $V_{AB}$ ) 50V/div.

The gate source voltage  $V_{gs}$  and the drain source voltage  $V_{ds}$  of one switch of the converter are depicted in figure 7.4 and 7.5.

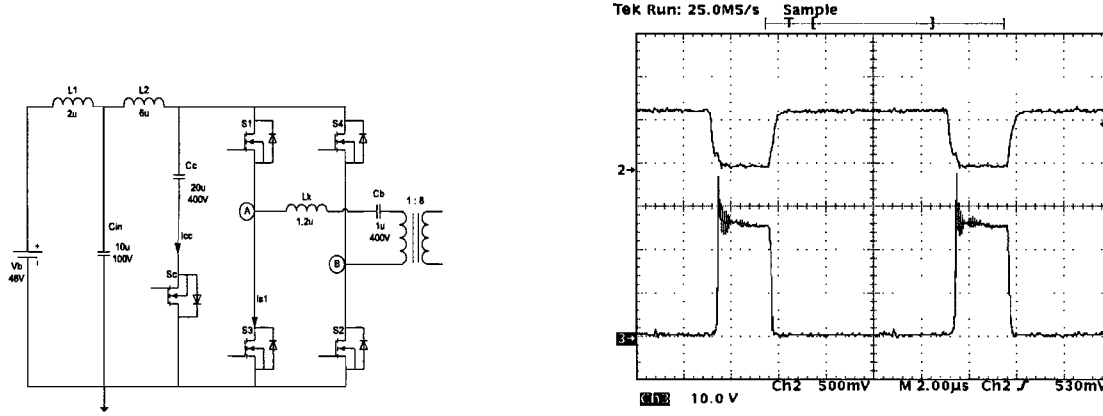


Figure 7.4: Ch2:  $V_{gs}$  of  $S_4$  10V/div., Ch3:  $V_{ds}$  of  $S_4$  20V/div.

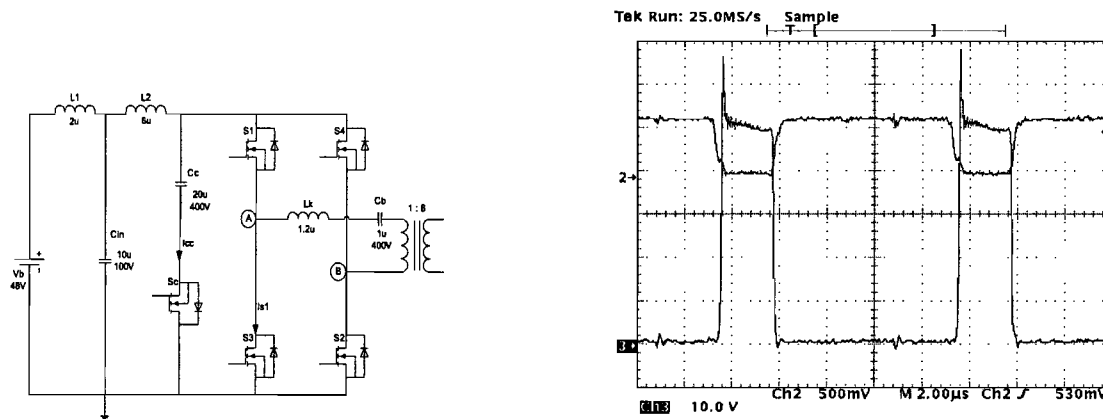


Figure 7.5: Ch2:  $V_{gs}$  of  $S_4$  10V/div., Ch3:  $V_{ds}$  of  $S_4$  20V/div. for  $P_{in} = 1kW$

The clamp capacitor current  $I_{cc}$  in figure 7.6 shows symmetrical charge and discharge allowing the dc bus voltage  $V_{AB}$  properly clamped.

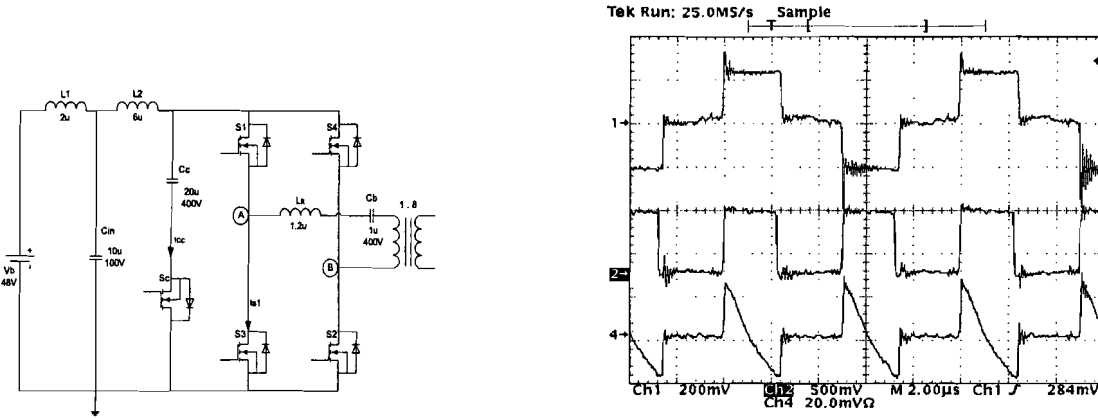


Figure 7.6: Ch1:  $V_{bridge}$  ( $V_{AB}$ ) 40V/div., Ch2:  $V_{gs}$  of  $S_c$  10V/div., Ch3:  $I_{cc}$  10A/div.

The current through one switch, in this case  $S_1$ , and the drain source voltage  $V_{ds1}$  are shown in figure 7.7 and 7.8. As can be seen the switch is operating under soft switching. Because of practical considerations only the current through one switch was measured. However, the same waveforms can be applied to the other switches.

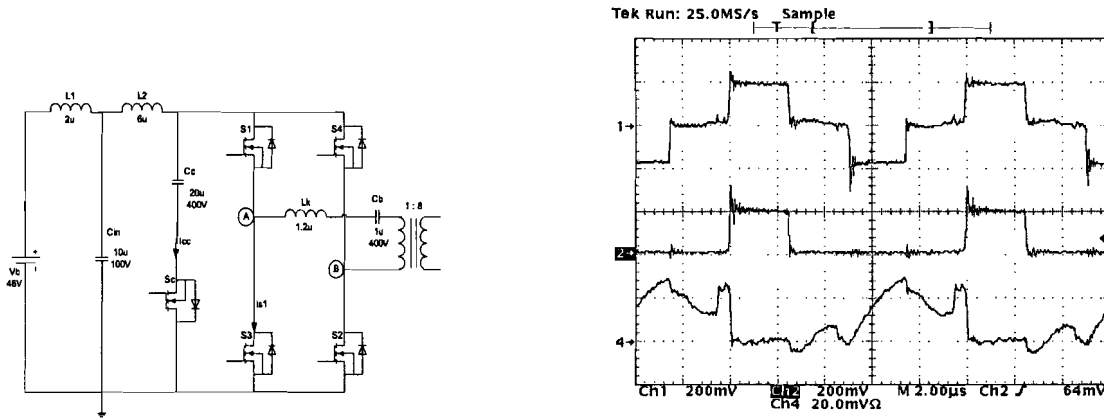


Figure 7.7: Ch1:  $V_{bridge}$  ( $V_{AB}$ ) 40V/div., Ch2:  $V_{ds}$  of  $S_1$  40V/div., Ch4:  $I_{s1}$  10A/div.

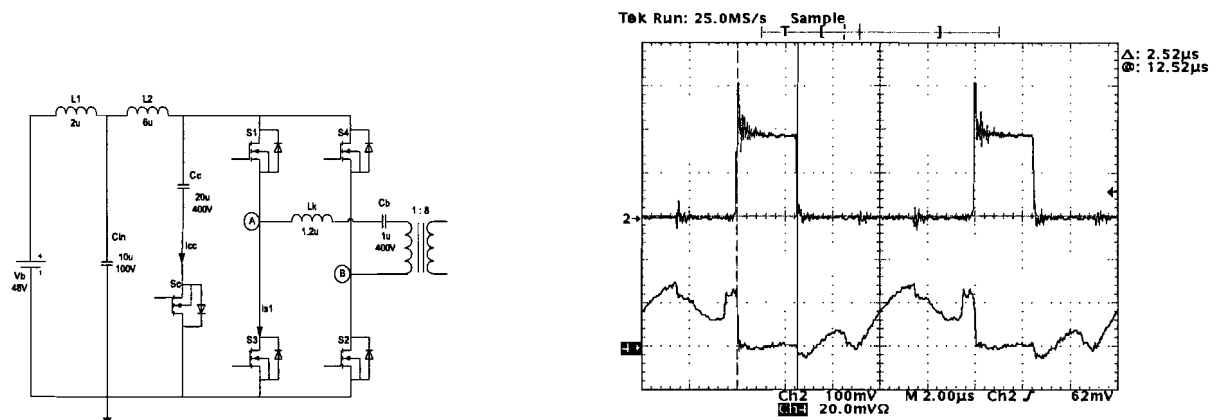


Figure 7.8: Ch2:  $V_{ds}$  of  $S_1$  40V/div., Ch4:  $i_{s1}$  25A/div.

The current through the leakage inductor,  $I_{Lk}$ , is given in figure 7.9. In the same figure, also the voltage across the active clamp capacitor  $V_{cc}$  is shown. It can be seen that the active clamp capacitor clamps well the converter bridge.

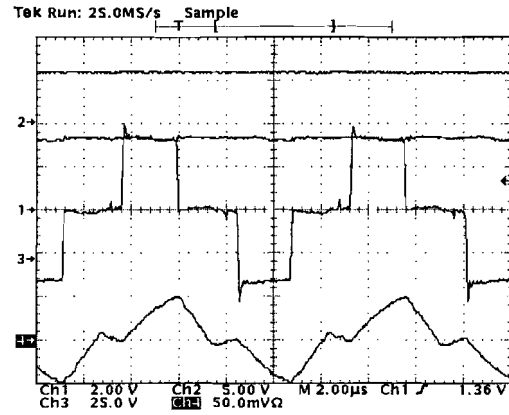
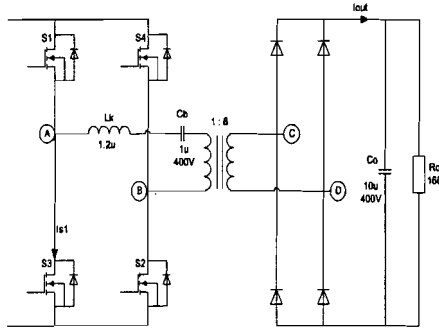


Figure 7.9: Ch1:  $V_{bridge}$  ( $V_{AB}$ ) 40V/div., Ch2:  $V_{out}$  400V/div., Ch3:  $V_{cc}$  25V/div., Ch4:  $I_{Lk}$  25A/div.

Figure 7.10 shows the secondary voltage,  $V_{CD}$  that is about 400V and the output current of the converter  $I_{out}$ .

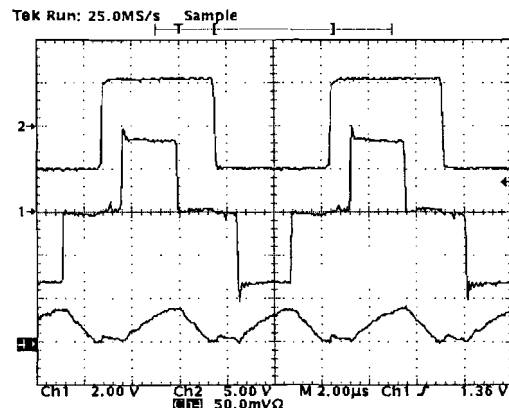
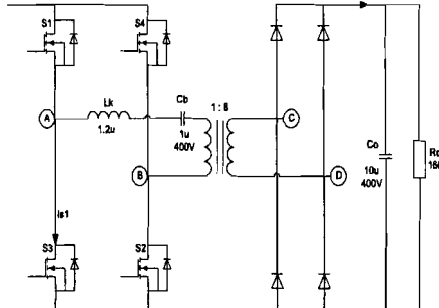


Figure 7.10: Ch1:  $V_{bridge}$  ( $V_{AB}$ ) 40V/div., Ch2:  $V_{secondary}$  ( $V_{CD}$ ) 400V/div., Ch4:  $I_{out}$  5A/div.

Finally, the primary side current,  $I_{Lk}$  and the output current,  $I_{out}$  together with the converter bridge voltage for full power are depicted in figure 7.11 and 7.12.

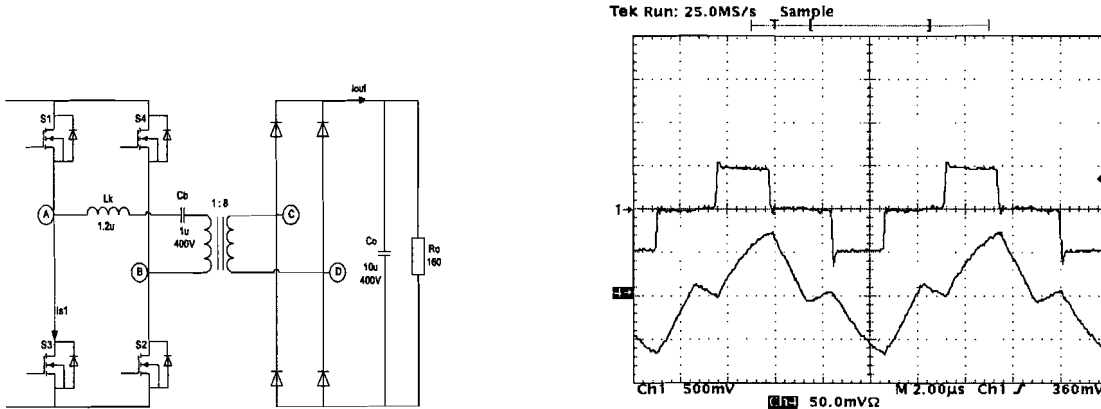


Figure 7.11: Ch1:  $V_{bridge}$  ( $V_{AB}$ ) 100V/div., Ch4:  $I_{Lk}$  25A/div. for  $P_{in} = 1kW$

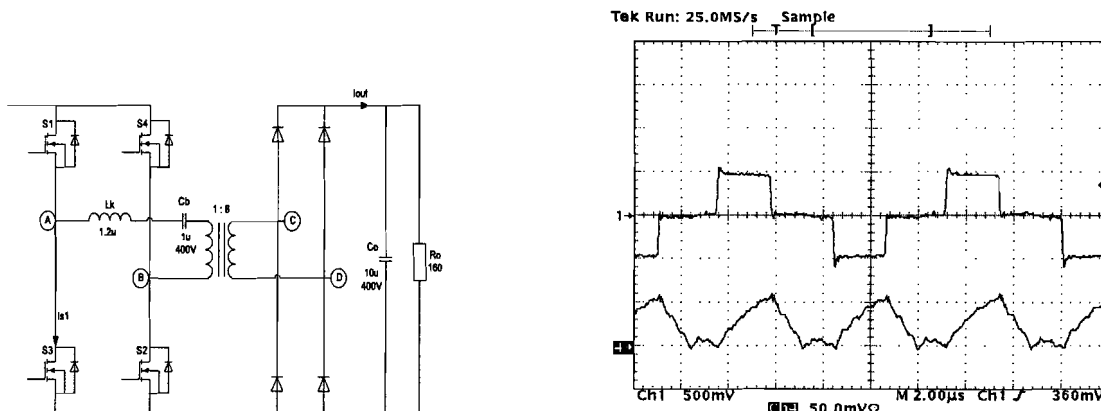


Figure 7.12: Ch1:  $V_{bridge}$  ( $V_{AB}$ ) 100V/div., Ch4:  $I_{out}$  5A/div. for  $P_{in} = 1kW$

### 7.2.2 Efficiency evaluation

The 1kW prototype converter that is shown in figure 7.13 was tested in the lab for different values of load. Furthermore, various measurements have been carried out to determine the efficiency of the converter in discharging mode.

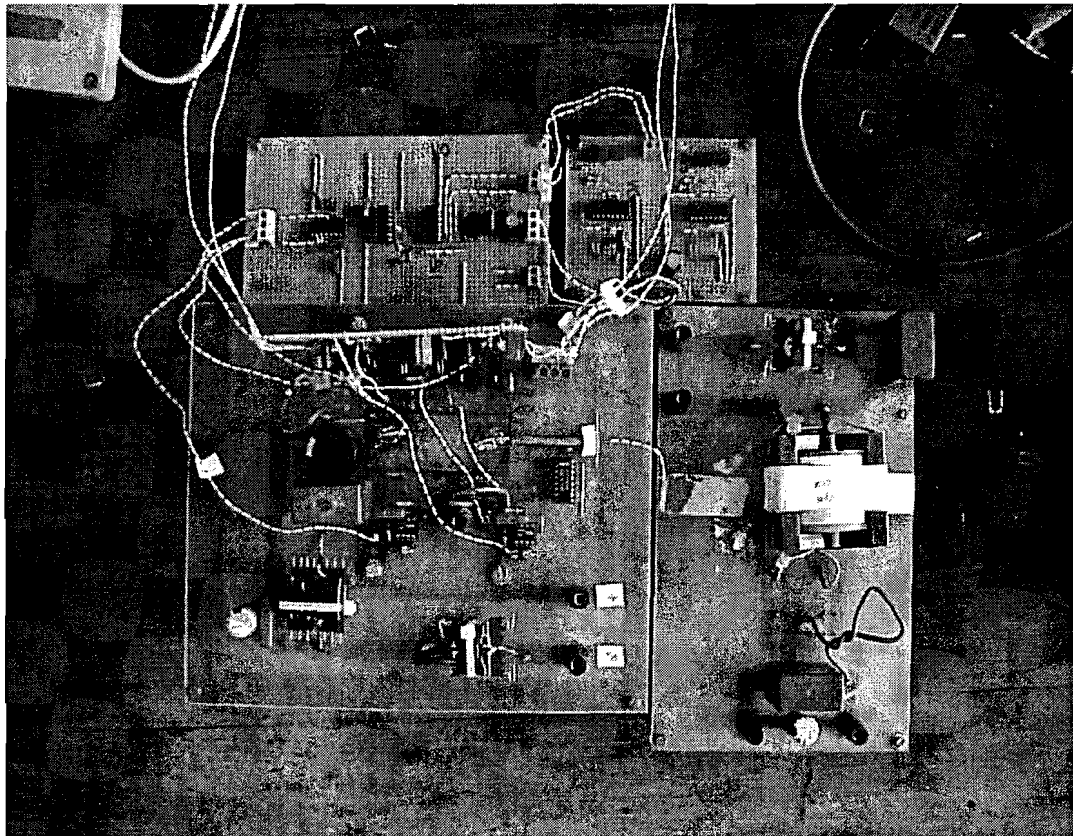


Figure 7.13: Photograph of converter

Table 7.1 on the next page shows the test results of the full-bridge current fed converter operating under discharging (boost) mode condition. The test was done at a constant input voltage of 48V and a switching frequency of 100kHz for a few different load conditions.

For example, it can be seen that an input power of  $P_{in} = 1036.8W$  results in an output power of  $P_{out} = 852.6W$ . That means that at full input power the efficiency is about 82%. It should be noticed that this percentage tends to increase after treating the power loss calculation in paragraph 7.2.3.

$V_{in}(V)$	$I_{in}(A)$	$P_{in}(W)$	$V_{out}(V)$	$I_{out}(A)$	$P_{out}(W)$	$\eta = \frac{P_{out}}{P_{in}} \cdot 100$
48.0	17.1	820.8	450.0	1.52	684.0	83.3
48.0	18.0	864.0	446.0	1.60	713.6	82.6
48.0	19.2	921.6	442.5	1.73	765.5	83.1
48.0	20.5	984.0	440.0	1.84	809.6	82.3
48.0	21.6	1036.8	435	1.96	852.6	82.2

Table 7.1: Measurement results of converter in discharging mode at  $F_s = 100kHz$  with varying load

Finally, measurements have been made for three different switching frequencies namely  $80kHz$ ,  $100kHz$ , and  $120kHz$  at different load conditions. From figure 7.14 it can be concluded that the converter shows better efficiency for a lower switching frequency, namely  $80kHz$ . The complete measurements data of these efficiency profiles are included in Appendix K, L, and M.

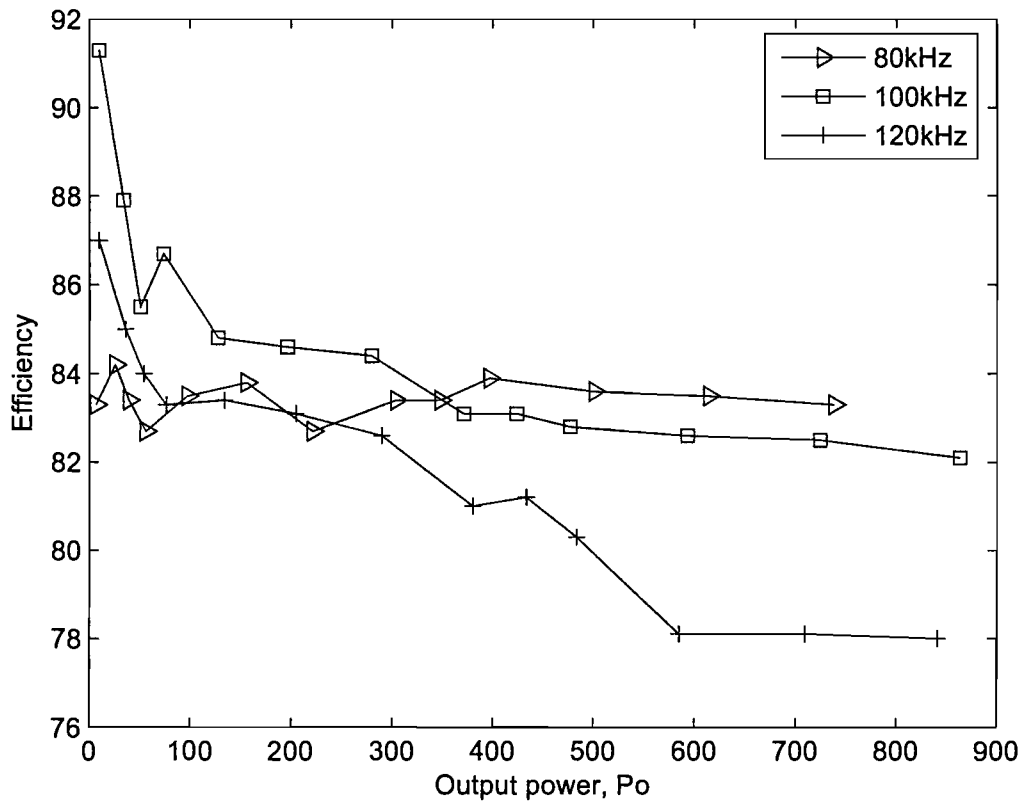


Figure 7.14: Efficiency profile for different switching frequencies

### 7.2.3 Power loss calculation

The power loss calculation in this section has been carried out for  $P_{in} = 1kW$ ,  $F_s = 100kHz$  and an efficiency of 82%. That means that there is a power loss of about 180W that should be explained. Figure 7.15 shows a photograph and figure 7.16 gives an illustration of the test setup that was used during the measurements. The use of cables between the units have also played a role in the overall power losses.

In the following section, the power loss in all components of the converter and the cables as well will be determined, after which the power losses will be explained. As is well known, in case of power loss calculation, the RMS value of the current through the components should be determined. Therefore, the RMS value of the current through the components will be calculated first after which the power loss in the components will be determined.

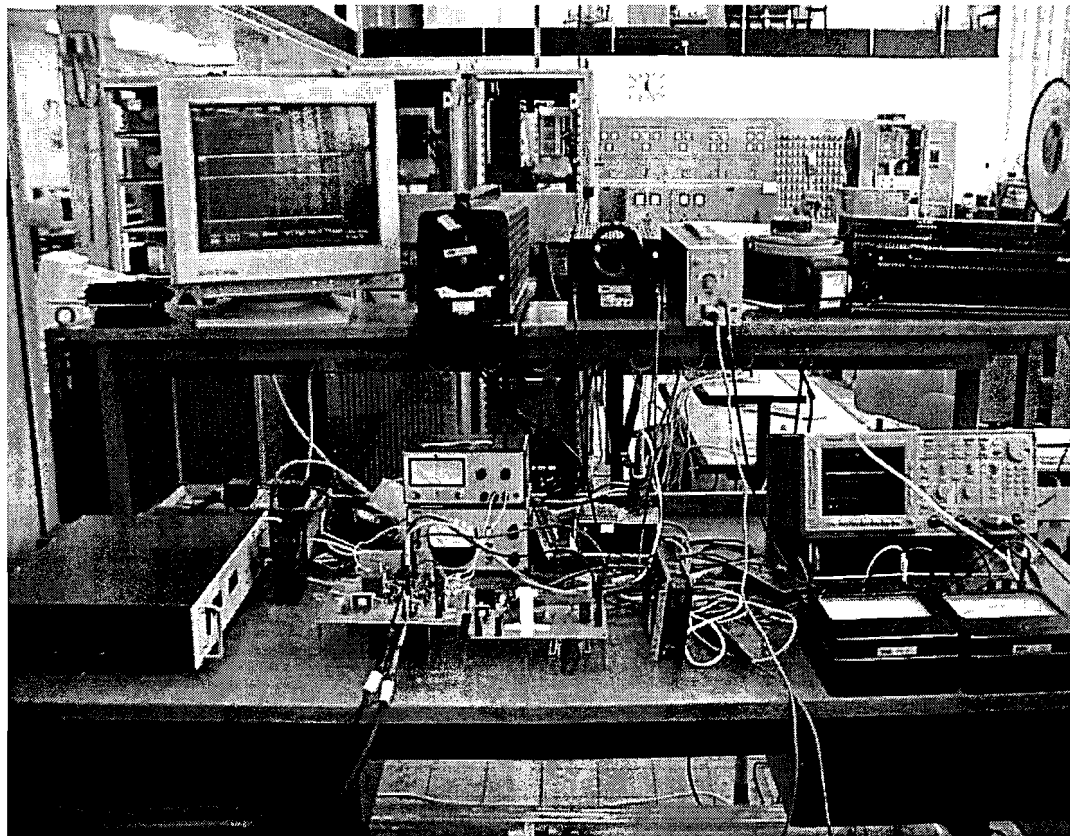


Figure 7.15: Photograph of test setup

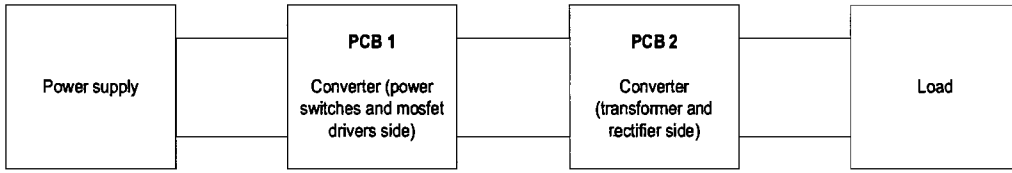


Figure 7.16: Illustration of test setup

### Cables from power supply to converter

At maximum power, the RMS value of the current from the power supply to the converter is  $I_{rms} = 22A$ . This current flows through a distance of  $l = 1.7m$ . The cross section area of the cable is  $A = 4mm^2$  and the resistivity of copper is  $\rho = 17.8\Omega^{-9}/m$ . The cable impedance can be calculated by the following expression:

$$R = \frac{\rho l}{A} = 7.6m\Omega \quad (7.2)$$

The power loss in the two cables can be obtained as follows:

$$P_{loss} = 2RI_{rms}^2 = 2 \cdot 7.6 \cdot 10^{-3} \cdot 22^2 = 7.4W \quad (7.3)$$

### Mosfets ( $S_1 - S_4$ )

As the Mosfets of the converter are operating under ZVS, the dissipated power in the Mosfet is only due to on state losses and can be calculated with the following equation:

$$P_{con} = I_{SW(RMS)}^2 R_{DS(on)} \frac{t_{on}}{T_s} \quad (7.4)$$

Where the on state resistance of the Mosfet  $R_{DS(on)} = 20m\Omega$ ,  $t_{on} = 7\mu s$ , and the switching frequency  $T_s = 10\mu s$ . By means of an estimation and verification of the RMS value of the current through the Mosfet, this value turned out to be  $28.6A$  at full power. The dissipated power in the four Mosfets is then:

$$P_{con} = 4 \cdot I_{SW(RMS)}^2 R_{DS(on)} \frac{t_{on}}{T_s} = 45.8W \quad (7.5)$$

### Active clamp branch

In order to determine the resistance of the active clamp capacitors, they have been considered as a black box as can be seen in figure 7.17. Then, the current through and the voltage across the capacitors have been measured. The obtained resistance value is as follows:

$$r = \frac{\hat{v}}{\hat{i}} = \frac{0.5V}{4.0A} = 125m\Omega \quad (7.6)$$

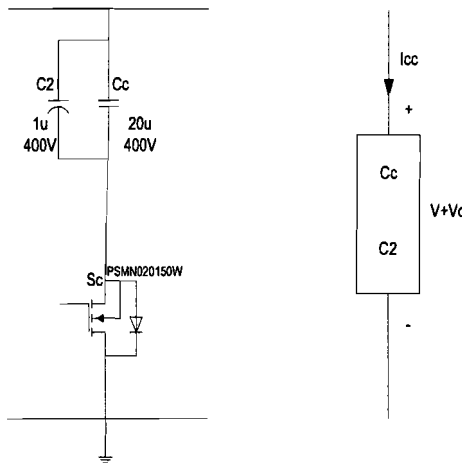


Figure 7.17: Active clamp branch

From the current waveform of the active clamp capacitor that is given in paragraph 4.4 the following expression for the current has been derived:

$$i = \frac{\hat{I}_{cc}}{2.5\mu s} \cdot t \quad (7.7)$$

The RMS value of the current through the active clamp capacitors is then as follows:

$$I_{RMS} = \sqrt{\frac{1}{T_s} \int_0^t i^2 dt} = 0.2\hat{I}_{cc} \quad (7.8)$$

The dissipated power in the active clamp capacitors for the maximum value of  $\hat{I}_{cc} = 22A$  is given by:

$$P_{acb} = 5 \cdot 10^{-3} \cdot \hat{I}_{cc}^2 = 2.42W \quad (7.9)$$

**Active clamp Mosfet  $S_c$** 

The dissipated power in the active clamp Mosfet  $S_c$  is calculated as follows:

$$P_{con} = I_{SW(RMS)}^2 R_{DS(on)} \frac{t_{on}}{T_s} \quad (7.10)$$

Where the on state resistance of the Mosfet  $R_{DS(on)} = 20m\Omega$ ,  $t_{on} = 1.5\mu s$ , and the switching frequency  $T_s = 5\mu s$ . The RMS value of the current through the Mosfet is  $I_{RMS} = 0.2\hat{I}_{cc}$ . The dissipated power in the Mosfets is then:

$$P_{con} = 0.2W \quad (7.11)$$

**Cables from PCB1 to PCB2**

The output of the converter bridge, i.e. PCB1 is connected to the transformer and rectifier side, i.e PCB2 by means of cables through a distance of  $l = 0.5m$ . The cross section area of the cable  $A = 0.75mm^2$  and the resistivity of copper is  $\rho = 17.8\Omega^{-9}/m$ . The current through the cables concerns the primary side current of the transformer  $I_{Lk}$ . The RMS value of  $I_{Lk}$  has been calculated and is given by the following equation:

$$I_{RMS} = 0.58\hat{I}_{Lk} \quad (7.12)$$

The cable impedance is then:

$$R = \frac{\rho l}{A} = 12m\Omega \quad (7.13)$$

The power loss in the two cables is as follows:

$$P_{loss} = 2RI_{rms}^2 = 2 \cdot 12 \cdot 10^{-3} \cdot 20.3^2 = 10W \quad (7.14)$$

### Power dissipation in PCB tracks

As the power dissipation in PCB tracks plays a significant role at such high currents, the power losses in the important tracks are determined. The biggest track on the PCB is the track from the power supply through the input inductors with  $l = 0.7m$ ,  $w = 0.01m$ , and  $d = 35 \cdot 10^{-6}m$ . That means that the resistance of this track is as follows:

$$R = \frac{\rho l}{A} = \frac{17.8 \cdot 10^{-9} \cdot 0.7}{35 \cdot 10^{-6} \cdot 1 \cdot 10^{-2}} = 35.6m\Omega \quad (7.15)$$

The RMS value of the current through this track is  $I_{RMS} = 22A$  and that leads to the following power dissipation:

$$P_{diss} = 35.6 \cdot 10^{-3} \cdot 22^2 = 17.2W \quad (7.16)$$

The second important track on the PCB is the one between the converter bridge and the primary side of the transformer with  $l = 0.4m$ ,  $w = 0.01m$ , and  $d = 35 \cdot 10^{-6}m$ . The resistance of this track is given by:

$$R = \frac{\rho l}{A} = \frac{17.8 \cdot 10^{-9} \cdot 0.4}{35 \cdot 10^{-6} \cdot 1 \cdot 10^{-2}} = 20.4m\Omega \quad (7.17)$$

The RMS value of the current through this track is  $I_{RMS} = 0.58\hat{I}_{Lk}$  and that means that the power dissipation in this track is:

$$P_{diss} = 20.4 \cdot 10^{-3} \cdot 20.3^2 = 8.4W \quad (7.18)$$

The final important tracks on the PCB are conducting the current through the four Mosfets ( $S_1 - S_4$ ) with  $l = 0.2m$ ,  $w = 0.004m$ , and  $d = 35 \cdot 10^{-6}m$ . The RMS value of the current through the Mosfets at full power is  $I_{RMS} = 28.6A$ . The resistance of this track is obtained as follows:

$$R = \frac{\rho l}{A} = \frac{17.8 \cdot 10^{-9} \cdot 0.2}{35 \cdot 10^{-6} \cdot 0.4 \cdot 10^{-2}} = 25.4m\Omega \quad (7.19)$$

The power dissipation in this track is calculated by the following equation:

$$P_{diss} = 25.4 \cdot 10^{-3} \cdot 28.6^2 = 20.8W \quad (7.20)$$

### Control circuit

The power dissipation in the control circuit and the power Mosfet drivers has been determined with the aid of the power supply of the control circuit and was about  $8W$ .

### Rectifier diodes

From the datasheet of the Ixys Dsei 12-12A the following expression has been derived from the 'forward current versus voltage drop' characteristic at a junction temperature of  $100^\circ$  corresponding to the diode that is depicted in figure 7.18.

$$V_{ak} = V_t + I_D R_{ak} = 1.5 + 0.1 I_D \quad (7.21)$$

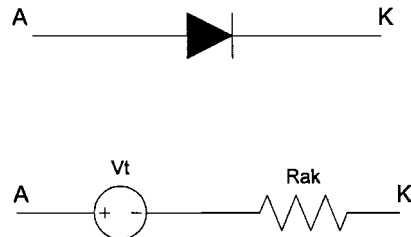


Figure 7.18: Diode

The power dissipation in the four diodes has been calculated with the following expression:

$$P_{dissD} = 4 \cdot \frac{1}{T_s} \int_0^{T_s} v_{ak} \cdot i_d dt \quad (7.22)$$

The peak value of the diode current is  $\hat{i}_d = 5A$ , that leads to the following power dissipation in the diodes:

$$P_{dissD} = 4 \cdot \frac{\hat{i}_d}{2} (1.5 + 0.1 \hat{i}_d) = 20W \quad (7.23)$$

### Magnetic components

By measuring the resistances of the magnetic components, determining the RMS value of the current through the components, and making use of Magtool the power dissipation in each magnetic can be given:

- $L_1$ :  $P_{L1} = 8.7W$
- $L_2$ :  $P_{L2} = 9.2W$
- $L_k$ :  $P_{Lk} = 7.5W$
- Transformer:  $P_{Traf} = 10W$

Table 7.2 below summarizes the power dissipation of the devices of the bi-directional DC-DC converter in discharging mode. As can be seen, most of the 180W power loss has been explained. The remaining 5W can be caused by the remaining smaller PCB tracks. From the power loss calculation we can conclude that the overall efficiency of the converter can be improved when using shorter cables. In that case an overall efficiency of about 85% can be achieved.

Power dissipation in the devices used	
Device or section	Power dissipation (W)
Cables from power supply to converter	7.4
Mosfets ( $S_1 - S_4$ )	45.8
Active clamp branch	2.42
Active clamp Mosfet ( $S_c$ )	0.2
Cables from PCB1 to PCB 2	10
PCB tracks	46.5
Control circuit	8
Rectifier diodes	20
Inductor $L_1$	8.7
Inductor $L_2$	9.2
Inductor $L_k$	7.5
Transformer	10
<b>Total losses</b>	<b>175.7</b>

Table 7.2: Power dissipation in the devices used

## 7.3 Charging mode

### 7.3.1 Experimental waveforms

A photograph of the bi-directional DC-DC converter in charging mode is shown in Figure 7.19. The phase shift converter in charging mode has been tested for an input voltage of  $V_{in} = 400V$  and a battery voltage  $V_{bat}$  of about 50V. As mentioned earlier, the battery power  $P_{bat}$  should be 10% of full power of Fuel Cell energy management system during steady operation, namely 100W. As the current of the converter in charging mode is very small, the overall efficiency is higher than 90%.

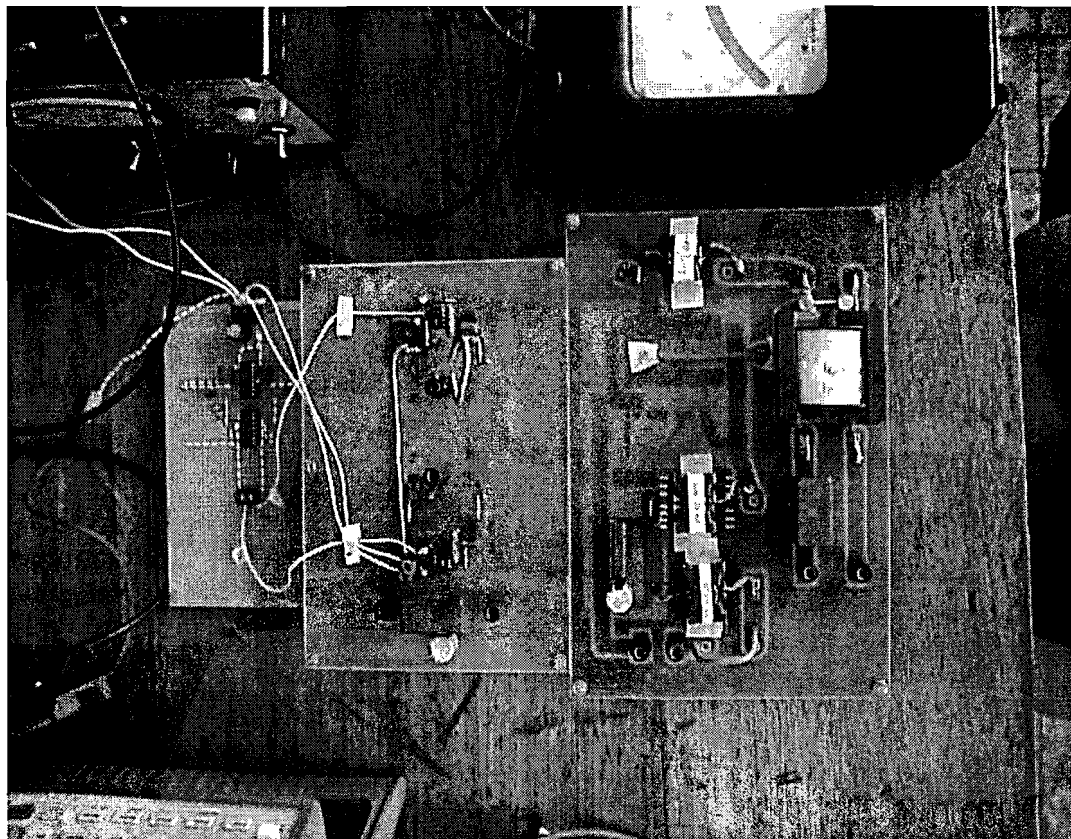


Figure 7.19: Photograph of converter in charging mode

The power circuit of the bi-directional DC-DC converter in charging with the test points that are used during the measurements is depicted in figure 7.20.

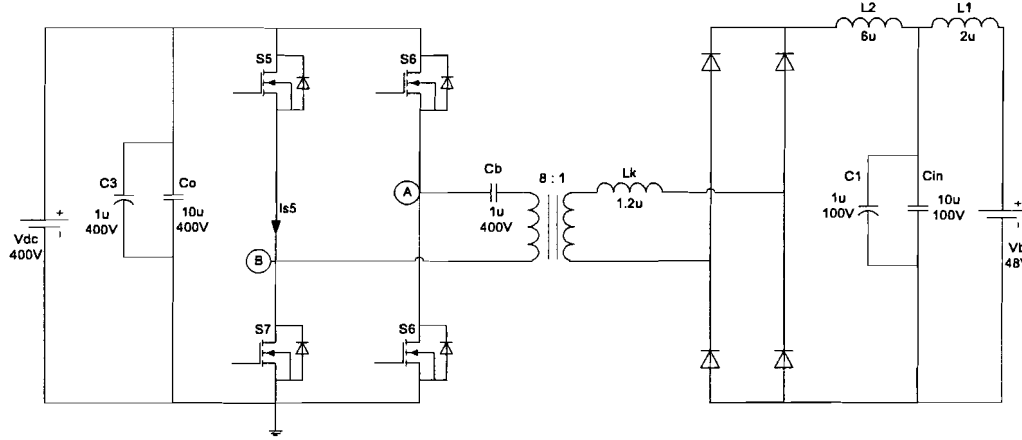


Figure 7.20: Converter in charging mode with test points

The phase shifted gate source signals  $S_5$  and  $S_8$  of the converter are depicted in figure 7.21.

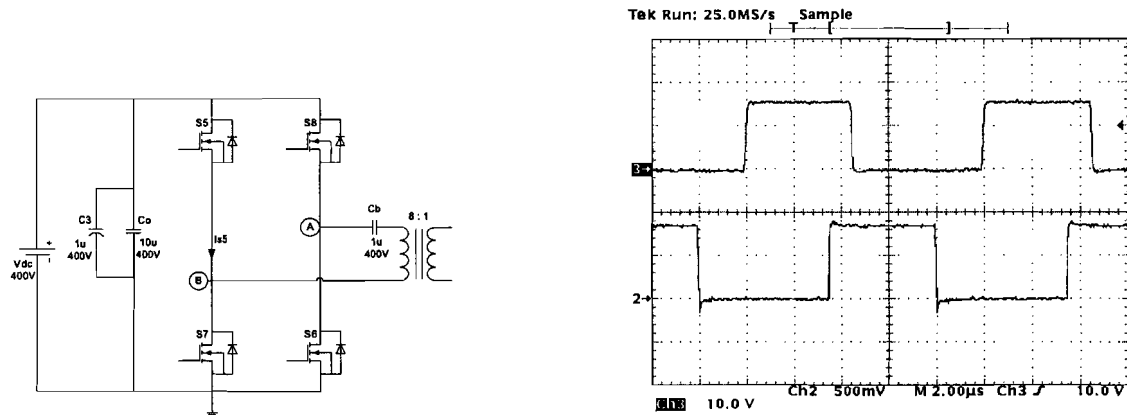


Figure 7.21: Ch2:  $V_{gs}$  of  $S_8$ , 10V/div., Ch3:  $V_{gs}$  of  $S_5$ , 10V/div.

Figure 7.22 shows the gate source signals of the two Mosfets,  $S_5$  and  $S_7$  of one converter leg. It shows the deadtime of  $520\text{ns}$  between the two signals that corresponds to the deadtime that is introduced by the power Mosfet driver IR2104. The converter bridge voltage  $V_{AB}$  with a peak value of  $400\text{V}$  is given in figure 7.23.

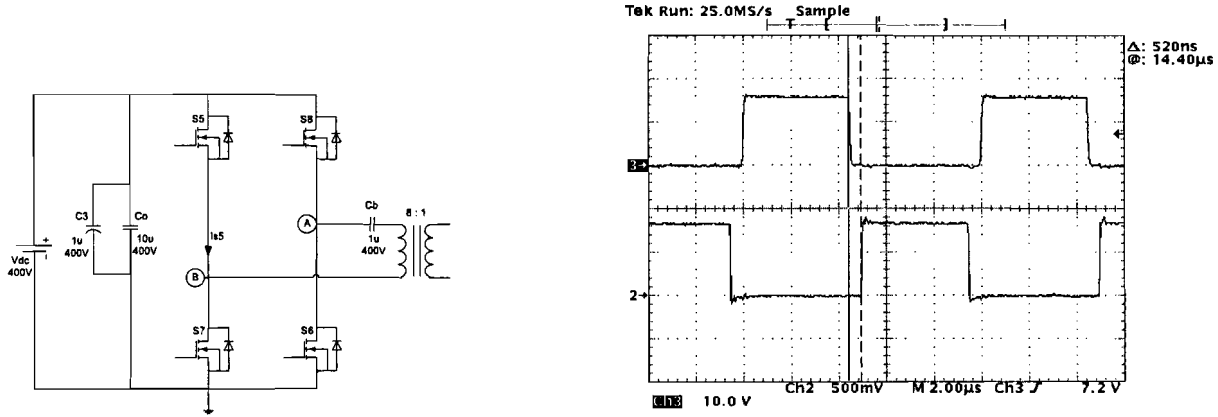


Figure 7.22: Ch2:  $V_{gs}$  of  $S_5$ ,  $10\text{V}/\text{div}$ , Ch3:  $V_{gs}$  of  $S_7$ ,  $10\text{V}/\text{div}$ .

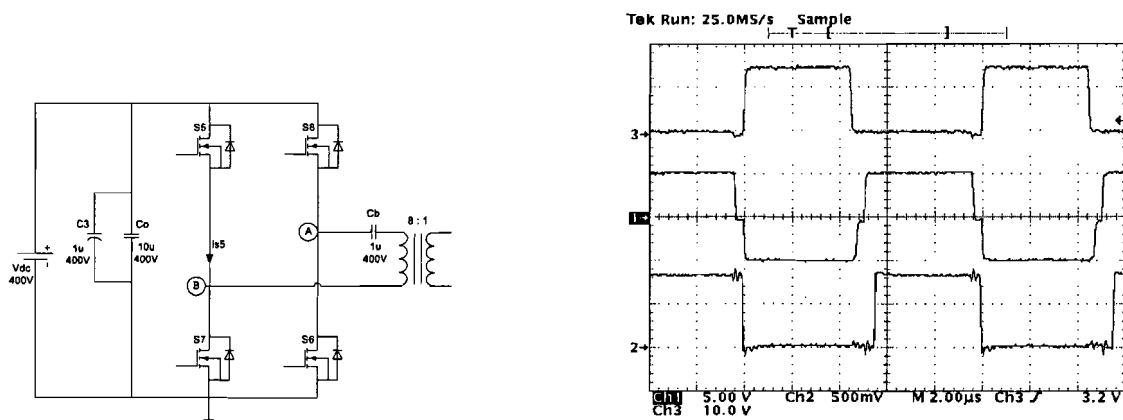


Figure 7.23: Ch1:  $V_{bridge}$  ( $V_{AB}$ ),  $400\text{V}/\text{div}$ , Ch2:  $V_{gs}$  of  $S_5$ ,  $10\text{V}/\text{div}$ , Ch3:  $V_{gs}$  of  $S_7$ ,  $10\text{V}/\text{div}$ .

Finally, the battery voltage  $V_{bat}$  and the battery charging current  $I_{bat}$  are depicted in the figure below.

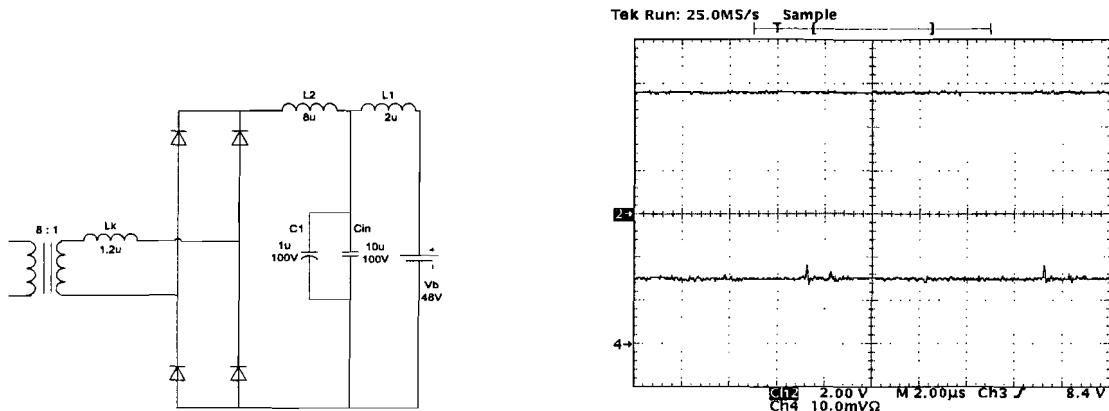


Figure 7.24: Ch2:  $V_{bat}$ , 20V/div., Ch4:  $I_{bat}$ , 1.5A/div.

# Chapter 8

## Conclusions and recommendations for future work

### 8.1 Conclusions on bi-directional DC-DC converter

This report has presented a bi-directional DC-DC converter for a Fuel Cell energy management system. As PEM Fuel Cells have a delay of several minutes, they cannot immediately take over full load in case of a power failure if assuming that the Fuel Cell is operated in a UPS system. Therefore a battery should compensate for response delay. The bi-directional DC-DC converter should be operated in Fuel Cell energy management system to discharge the battery during the start up period of the Fuel Cell to ensure that the load is properly supplied.

When the Fuel Cell is powering up and is able to provide 1kW power to the load, the bi-directional converter should switch to the charging mode. That means that the battery should be recharged with a fraction of full power from the bi-directional converter.

The bi-directional DC-DC converter that has been presented in this report concerns a converter with two active switch bridges on both sides of an isolation transformer:

- Voltage fed full-bridge, a bridge on the high voltage side fed by a voltage source
- Current fed full-bridge, a bridge on the low voltage side fed by a current source

This converter consists also of an active clamp branch that is placed across the current-fed bridge. The active clamp branch consists of an active switch and an energy storage capacitor. The benefits of the active clamp branch are as follows:

- It is used to achieve soft switching for the voltage-fed bridge in charging mode.
- In combination with the input inductor  $L$ , the active clamp branch works as an up converter during discharging mode. That means that the battery voltage is boosted leading to a smaller transformer ratio.

- In discharging mode, it limits the overshoot of the bridge switch's turn off and enables the energy stored in the transformer leakage inductance to be used for zero voltage switching.

## **8.2 Conclusions on bi-directional DC-DC converter in discharging mode**

The bi-directional DC-DC converter in discharging mode has been implemented and was tested under full input power,  $P_{in} = 1kW$  and a switching frequency,  $F_s = 100kHz$  for different load conditions. It showed good experimental results which are presented in paragraph 7.2. Furthermore, the overall efficiency is about 85% after being adjusted for power losses that can be avoided, for example by using shorter cables at the test setup.

In the test setup the battery was emulated by a power supply that was able to provide  $1kW$ . In order to determine which battery should be chosen in the future, the load profile for the system must be analyzed. That can be done by testing the load profile during a time period of 24 hours in order to determine the load requirement. Based on the load profile, the battery can be chosen on its ability to supply the required energy for a given time period. Furthermore, the required battery voltage of  $48V$  can be acquired by placing four  $12V$  batteries in series.

## **8.3 Conclusions on bi-directional DC-DC converter in charging mode**

The bi-directional DC-DC converter has been tested for a battery power,  $P_{bat} = 100W$  and a switching frequency of  $F_s = 100kHz$ . The experimental results are presented in paragraph 7.3.

As the power in charging mode is only about  $100W$ , the benefits of using the secondary active clamp are negligible. That means that the active-clamp Mosfet  $S_c$  is permanently turned on during charging mode in this application. The advantages of using the secondary active clamp that are described in paragraph 4.5 are especially attractive for high power applications ( $\geq 1kW$ ). Using the secondary active clamp prevents free-wheeling current during charging mode and improves the overall efficiency.

# Bibliography

- [1] EG&G Technical Services, Inc.  
Fuel Cell Handbook (sixth edition)  
Science Applications International Corporation, 2002
- [2] J.A. Sabate, V. Vlatkovic, R.B. Ridley, F.C. Lee, and B.H. Cho  
Design considerations for high-power full-bridge zero-voltage-switched PWM converter  
Proc. IEEE Applied Power Electronics Conference, 1990, pp. 275-284
- [3] I. Barbi  
Soft switching high-frequency isolated DC-DC converter  
Authors edition  
Florianopolos, 1999
- [4] K. Wang, C.Y. Lin, L. Zhu, D. Qhu, F.C. Lee, and J.S. Lai  
Bi-directional DC to DC converters for Fuel Cell Systems  
IEEE Trans. On Power Electronics, 1998
- [5] J.G. Cho, C.Y. Jeong, and F.C. Lee  
Zero-voltage and zero-current-switching full-bridge PWM converter using secondary active clamp  
IEEE Trans. On Power Electronics, 1998
- [6] N. Mohan, T. Undeland, and W.Robbins  
Power Electronics: Converters, Applications and Design  
Wiley, 2002
- [7] F.B.M van Horck, and J.L. Duarte  
A treatise on magnetics and power electronics  
TU Eindhoven, 2002
- [8] J.W. Baek, J.G. Gho, D.W. Yoo, G.H. Rim and H.G. Kim  
An improved zero voltage and zero current switching full bridge PWM converter with secondary active clamp  
IEEE Trans. on Power Electronics, 1998

- [9] H.L. Chan , K.W.E. Cheng , D. Sutanto  
Phase-shift controlled DC-DC convertor with bi-directional power flow  
IEE Proceedings-Electric Power Applications 148 (2): 193-201 MAR 2001
- [10] A. Emadi and S. Williamson  
Status review of power electronics converters for Fuel Cell applications  
Journal of Power Electronics, vol. 1, no. 2, Oct. 2001, pp. 133-144
- [11] B. Essig and G. Braun  
Selecting batteries for uninterruptible power supply systems  
IEEE APEC Conference Proc., 1991, pp. 642-645
- [12] G. Hua, C.S. Leu, Y. Jiang and F.C. Lee  
Novel zero voltage-transition PWM converters  
IEEE Trans. on Power Electr., Vol 9, no 2, pp. 213-219, March 1994
- [13] M.H. Kheraluwala, R.W. Dedoncker and D.M. Divan  
Analysis, design and experimental evaluation of a high-power high-frequency bi-directional dc/dc converter  
EPE 1991, Firenze, Proc. Vol. 1, pp.568-573
- [14] J. Larminie and A. Dicks  
Fuel Cell systems explained  
Wiley & Sons, 2000
- [15] T. Reimann, S. Szeponik, G. Berger and J. Petzoldt  
A novel control principle of bi-directional dc-dc power conversion  
Conf. Rec. of IEEE PESC. St. Louis, MO, June 1998, pp. 978-989
- [16] E. Santi, D. Franzoni, A. Monti, D. Patterson, F. Ponci and N. Barry  
A Fuel Cell based domestic uninterruptible power supply  
IEEE Trans. on Power Electronics, 2002
- [17] L. Schuch, C. Rech, H.L. Hey, H.A. Grundling, H. Pinheiro and J.R. Pinheiro  
A battery ZVT bi-directional charger for uninterruptible power supplies  
IEEE PESC, 2002, pp.1841-1846
- [18] L. Schuch, C. Rech, H.L. Hey, H.A. Grundling, H. Pinheiro and J.R. Pinheiro  
Analysis and design of a new high-efficiency bi-directional ZVT PWM converter for DC bus and battery bank interface  
IEEE Applied Power Electr. Conf. Proc., 2002, pp. 567-573
- [19] L. Schuch  
AC/DC system with a bi-directional PWM converter for DC bus and battery bank interface  
Master Thesis, Federal University of Santa Maria, Brazil, july 2001

# Appendix A

## Matlab code: Derivation of system parameters

```
% This program calculates the leakage inductance of the bi-directional dc-dc
% converter in discharging mode operation for a given q and D

Vi=48;
Vo=400;
Io=2.5;

fs=input('Give a value for the switching frequency in kHz: ');
Po=1000;

q=input(' Give a value for q (q=Vopri/Vi): ');
D=input('Give a value for D (D=2*dT/Ts), with D smaller than 1: ');

Vc=(1/D)*Vi
Vopri=Vc*q
n=Vo/Vopri

Iopri=Io*n

Ioprinorm=D*(2-D)-q^2

d=1-D/2
Lk=(Ioprinorm*Vc)/(Iopri*8*fs*1000)
```

## Appendix B

### Matlab code: DCM and CCM algorithm

```
%The CCM mode:  
%This is given by q=sqrt(D*(2-D)-I).*(I>=D*(2-D))  
  
I=[0:1E-6:1];  
D=0.125;  
q1=sqrt(D*(2-D)-I).*(I<=D*(2-D));  
D=0.25;  
q2=sqrt(D*(2-D)-I).*(I<=D*(2-D));  
D=0.5;  
q3=sqrt(D*(2-D)-I).*(I<=D*(2-D));  
D=0.75;  
q4=sqrt(D*(2-D)-I).*(I<=D*(2-D));  
D=1;  
q5=sqrt(D*(2-D)-I).*(I<=D*(2-D));  
  
  
%Then DCM mode:  
%This mode is given by: q=2D^2/(I+2D^2)  
  
D=0.125;  
q1d=(2*D^2)./(I+2*D^2);  
D=0.25;  
q2d=(2*D^2)./(I+2*D^2);  
D=0.5;  
q3d=(2*D^2)./(I+2*D^2);  
D=0.75;  
q4d=(2*D^2)./(I+2*D^2);
```

```

D=1;
q5d=(2*D^2)./(I+2*D^2);

%The boundary between CCM and DCM:
%q0=0.5*(1+sqrt(1-2I)) and q02=0.5*(1-sqrt(1-2I)) for I<=0.5

I2=[0:1E-6:0.5-1E-6];%I2 is only up to 0.5
q0=0.5*(1+sqrt(1-2*I2));
q02=0.5*(1-sqrt(1-2*I2));

%Pad with zeros to have the same indices from 0:1E-6:1

q0f=[q0 0*[0.5:1E-6:1]];
q02f=[q02 0*[0.5:1E-6:1]];

%Then cut the CCM mode below the boundary curve and the DCM mode above it
%           CCM condition
%           |
%           V
%           ----- The second boolean condition is related to the DCM
%           /           \
q1f=q1.*((q1<=q02f) | (q1>=q0f))+q1d.*((q1d>q02f)&(q1d<q0f));
q2f=q2.*((q2<=q02f) | (q2>=q0f))+q2d.*((q2d>q02f)&(q2d<q0f));
q3f=q3.*((q3<=q02f) | (q3>=q0f))+q3d.*((q3d>q02f)&(q3d<q0f));
q4f=q4.*((q4<=q02f) | (q4>=q0f))+q4d.*((q4d>q02f)&(q4d<q0f));
q5f=q5.*((q5<=q02f) | (q5>=q0f))+q5d.*((q5d>q02f)&(q5d<q0f));

figure
hold on
plot(I,q1f)
plot(I,q2f)
plot(I,q3f)
plot(I,q4f)
plot(I,q5f)
plot(I2,q02,'b')
plot(I2,q0,'b')

```

## Appendix C

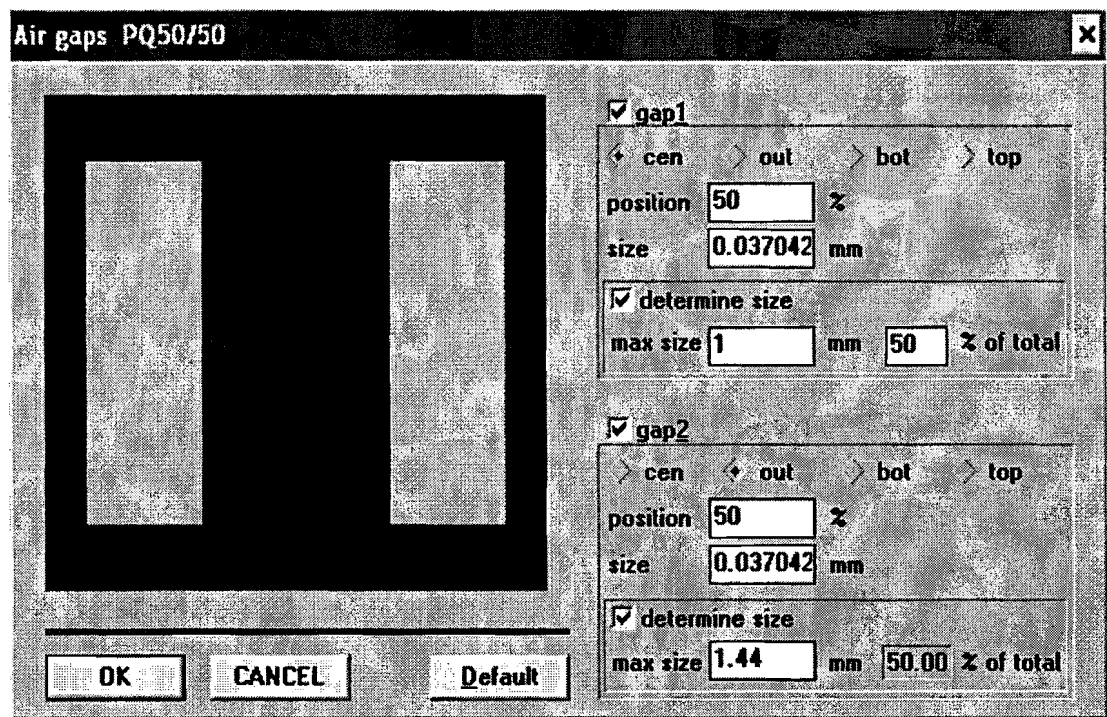
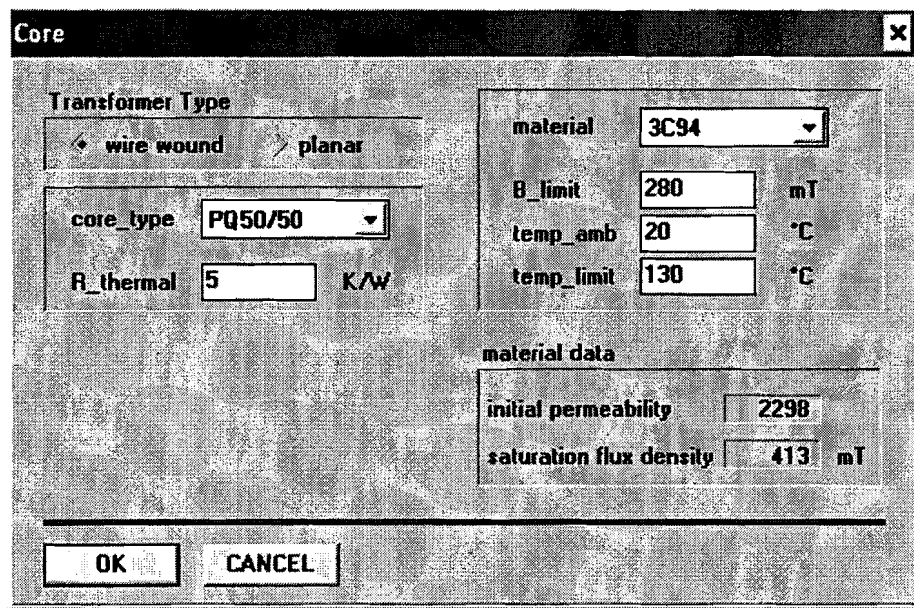
### Magtool results: Transformer

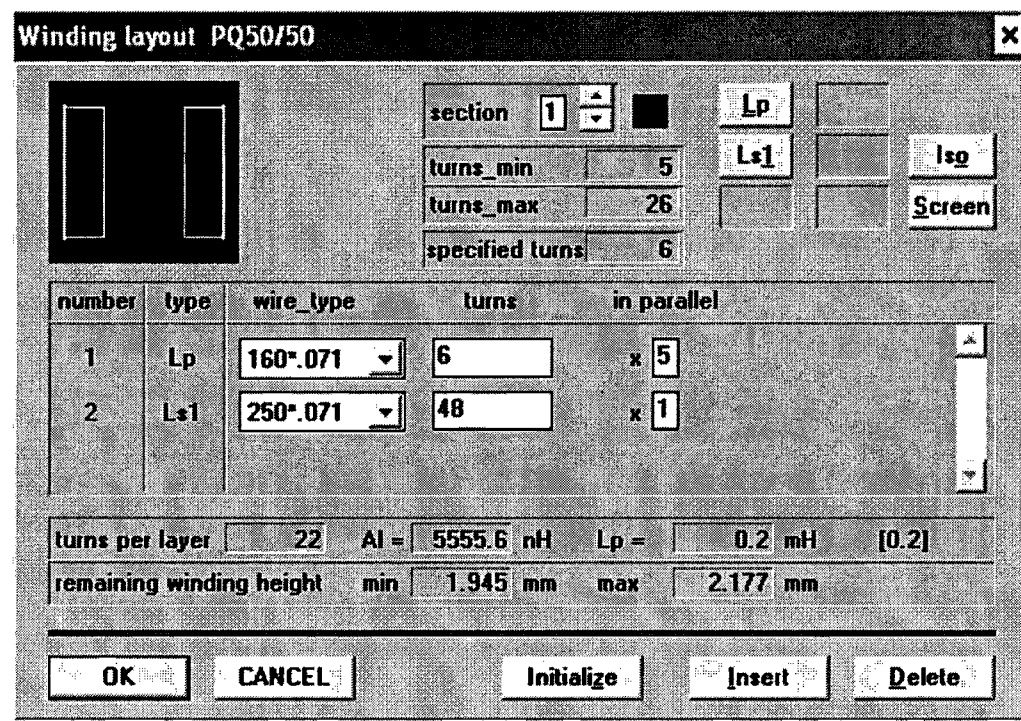
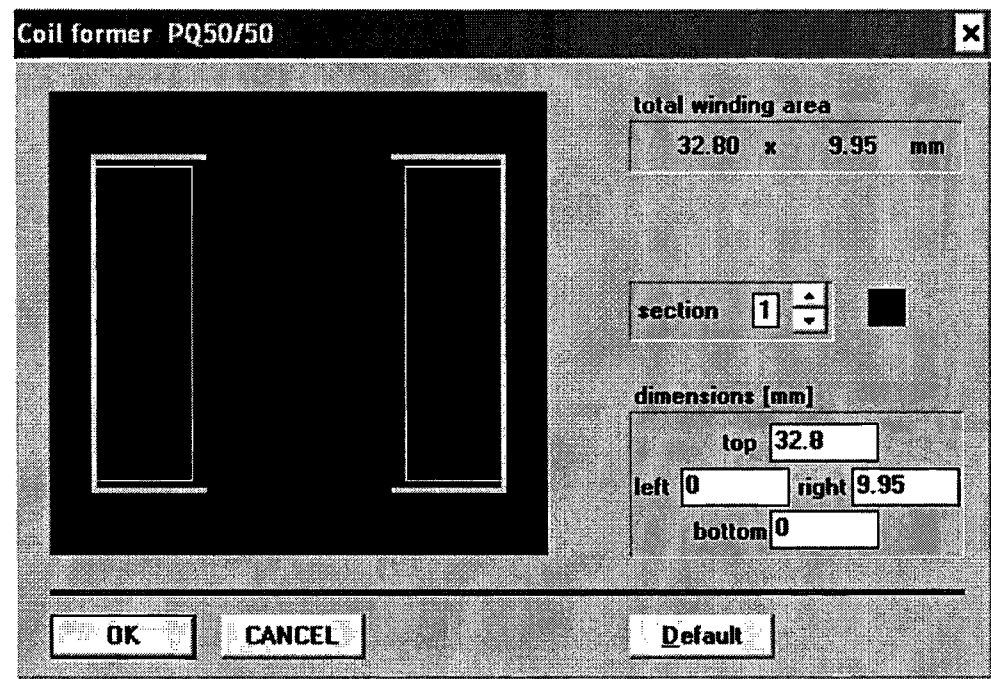
Component

primary inductance	tolerance	turns ratios Nprim/Nsec +/- tol
L <sub>p</sub> 0.2 mH	+ 5 %	N <sub>1</sub> 0.125 + 5 % N <sub>2</sub> 0 + 5 % N <sub>3</sub> 0 + 5 % N <sub>4</sub> 0 + 5 % N <sub>5</sub> 0 + 5 %
Component Name		
Transformer		
OK		CANCEL

Sinewave Current <Transformer>

	i_peak [A]	phase shift [°]
i <sub>p</sub>	48	
i <sub>s_1</sub>	6	180
frequency 100 kHz		
OK		CANCEL





**Design Data:**

<b>Realized values (temp_amb)</b>		<b>Results</b>	
L <sub>p</sub>	0.2 [mH]	turns	L <sub>p</sub> 0.25798 [mH] at 53.8 °C
N_1	0.125		B <sub>max</sub> 0.0 [mT] for Ae
N_2			B <sub>min</sub> 0.0 [mT] for Ae
N_3			B <sub>max</sub> 0.0 [mT] for Amin
N_4			B <sub>min</sub> 0.0 [mT] for Amin
N_5			B <sub>sat</sub> 382 [mT] at 53.8 °C
<b>Core data</b>		AI 5555.6 [nH]	
PQ50/50	3C94	u_eff	1525
gap1	0.013 [mm]	gap2	0.013 [mm]

**Total Losses: Transformer**

<b>Winding Losses [W]</b>							
turns	L <sub>p</sub>	L <sub>s1</sub>	L <sub>s2</sub>	L <sub>s3</sub>	L <sub>s4</sub>	L <sub>s5</sub>	total
rms	4.899	2.613					7.512
skin	0.317	0.322					0.638
proximity	0.398	1.398					1.796
total	5.613	4.333					



<b>Screen Losses [W]</b>	
specific	0.000
eddy current	0.000

<b>Core Losses [W]</b>	
specific	0.000
eddy current	0.000

<b>Total Losses [W]</b>	
9.946	

# Appendix D

## Magtool results: $L_1$

Component

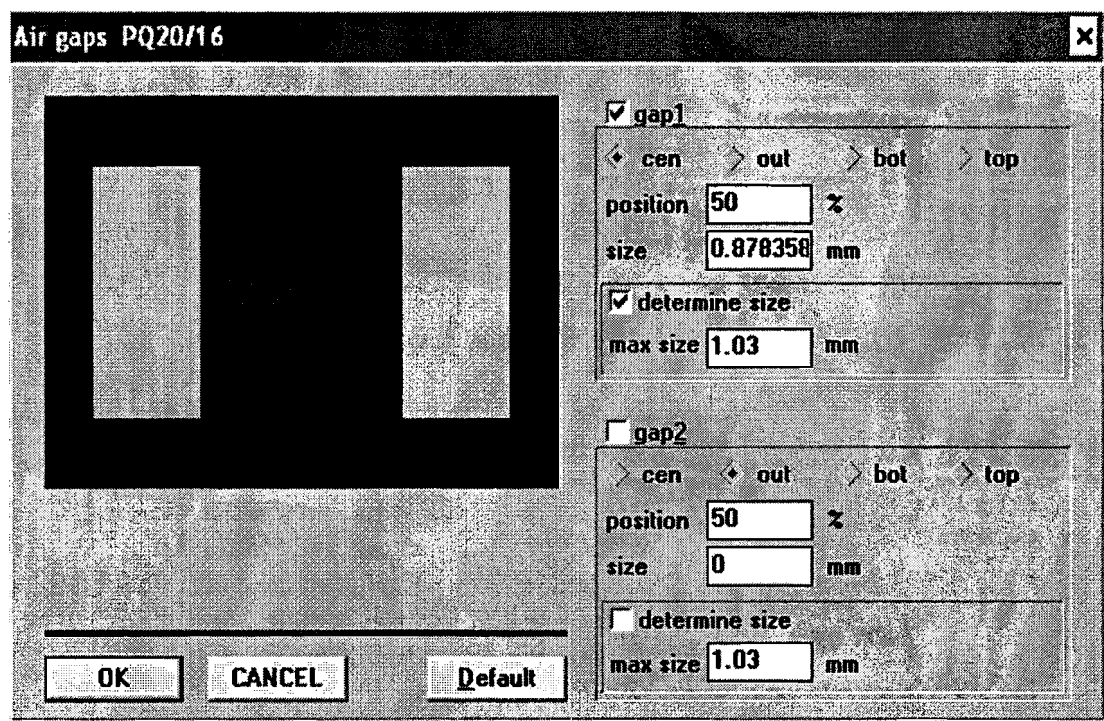
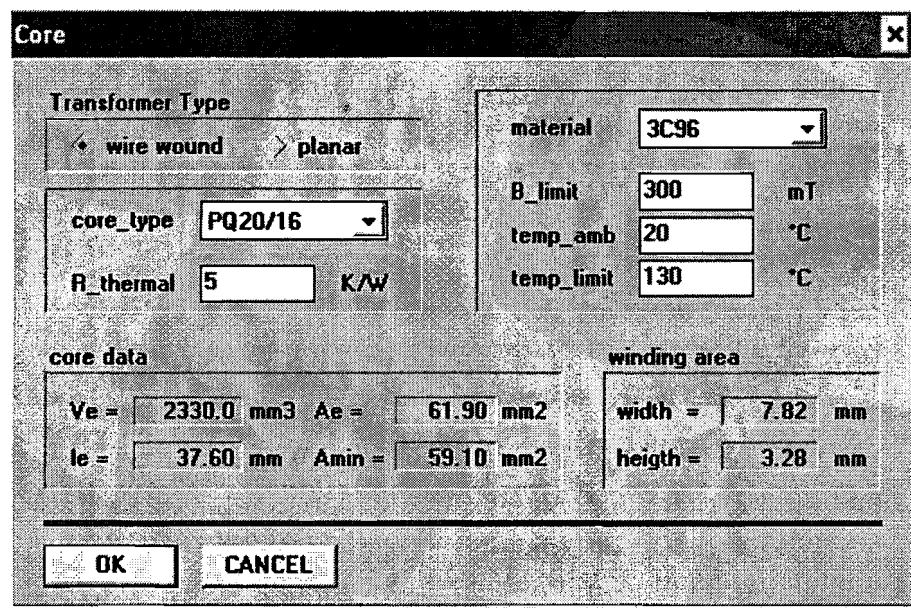
primary inductance	tolerance
$L_p$ 0.002 mH	$\pm 5\%$
Component Name :	
L1	
turns ratios: $N_{prim}/N_{sec} \pm tol$	
$N_1$	0 $\pm 5\%$
$N_2$	0 $\pm 5\%$
$N_3$	0 $\pm 5\%$
$N_4$	0 $\pm 5\%$
$N_5$	0 $\pm 5\%$

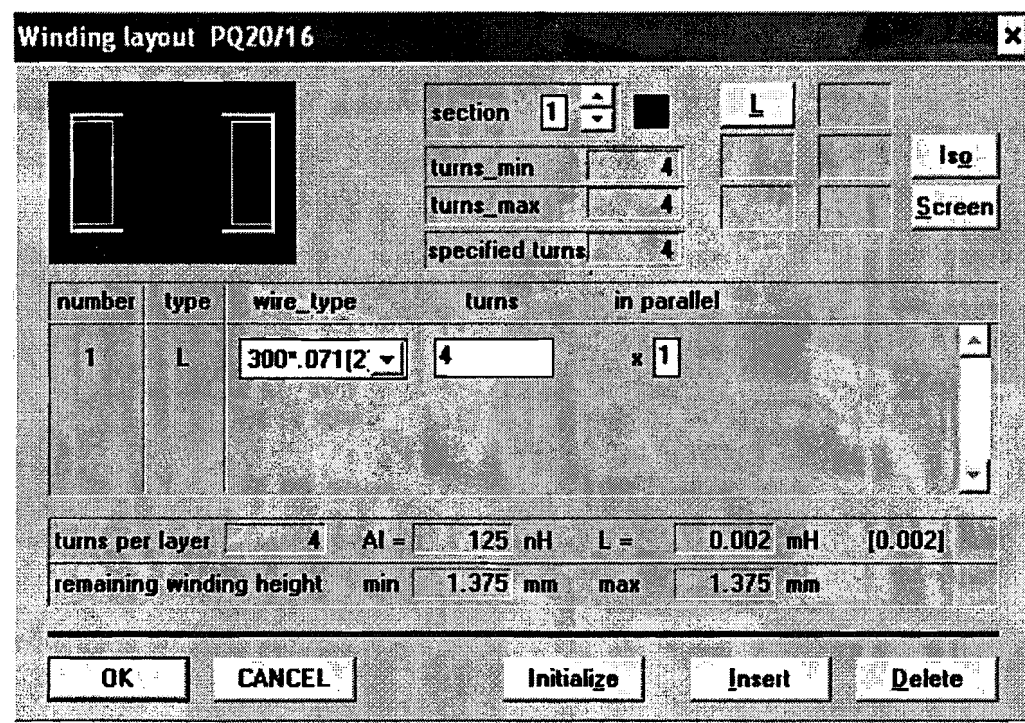
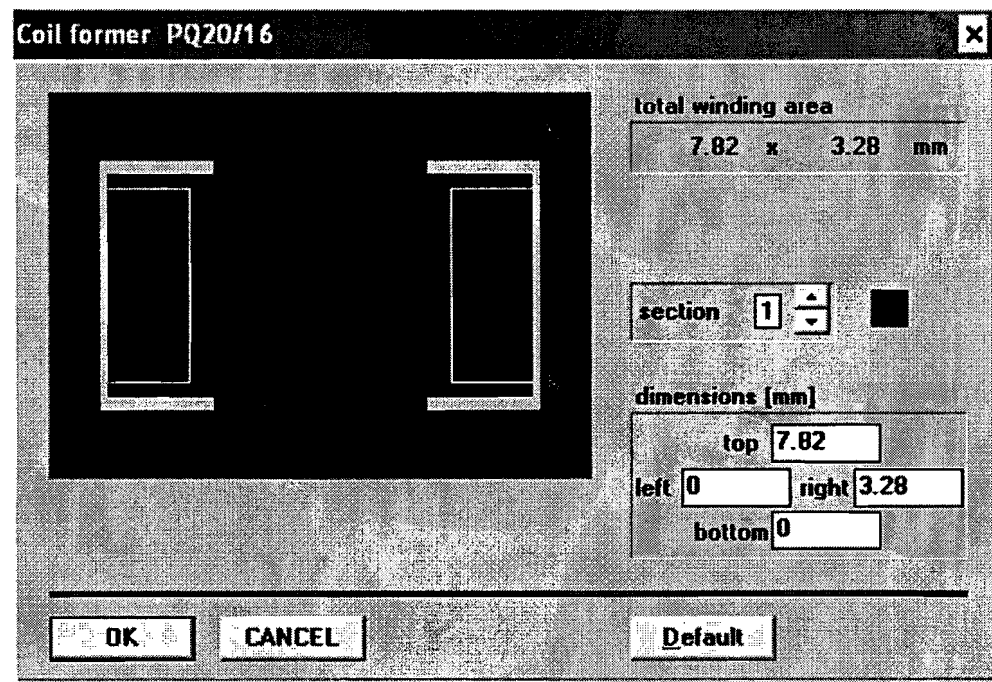
OK CANCEL

Sinewave Current <Choke>

i_L_peak	30 A
frequency	100 kHz

OK CANCEL





**Design Data: L1**

<b>Realized values (temp_amb)</b>		<b>Results</b>	
L <sub>p</sub>	0.002 [mH]	L <sub>p</sub>	0.0019996 [mH] at 39.5 °C
N_1		B <sub>max</sub>	242.2 [mT] for Ae
N_2		B <sub>min</sub>	242.2 [mT] for Ae
N_3		B <sub>max</sub>	253.6 [mT] for Amin
N_4		B <sub>min</sub>	253.6 [mT] for Amin
N_5		B <sub>sat</sub>	417 [mT] at 39.5 °C
		AI	125 [nH]
		u <sub>eff</sub>	60
<b>Core data</b>		gap1	0.878 [mm]
PQ20/16	3C96	gap2	0.000 [mm]

**Total Losses: L1**

<b>Winding Losses [W]</b>							
	L <sub>p</sub>	L <sub>s1</sub>	L <sub>s2</sub>	L <sub>s3</sub>	L <sub>s4</sub>	L <sub>s5</sub>	total
rms	1.144						1.144
skin	0.200						0.200
proximity	0.106						0.106
total	1.450						



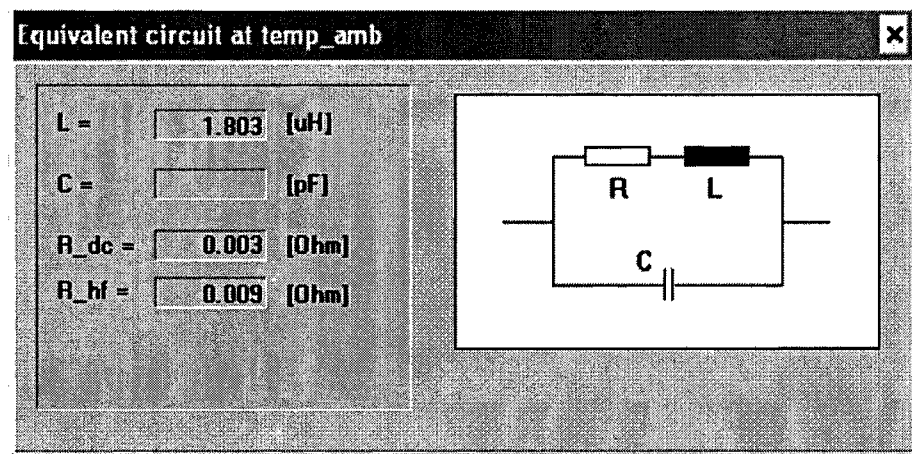
**Screen Losses [W]**

rms	0.000
skin	0.000
prox	0.000
screen	0.000
core	0.000

**Core Losses [W]**

specific	2.433
eddy current	0.025

**Total Losses [W]** 3.907



## Appendix E

### Magtool results: $L_2$

Component

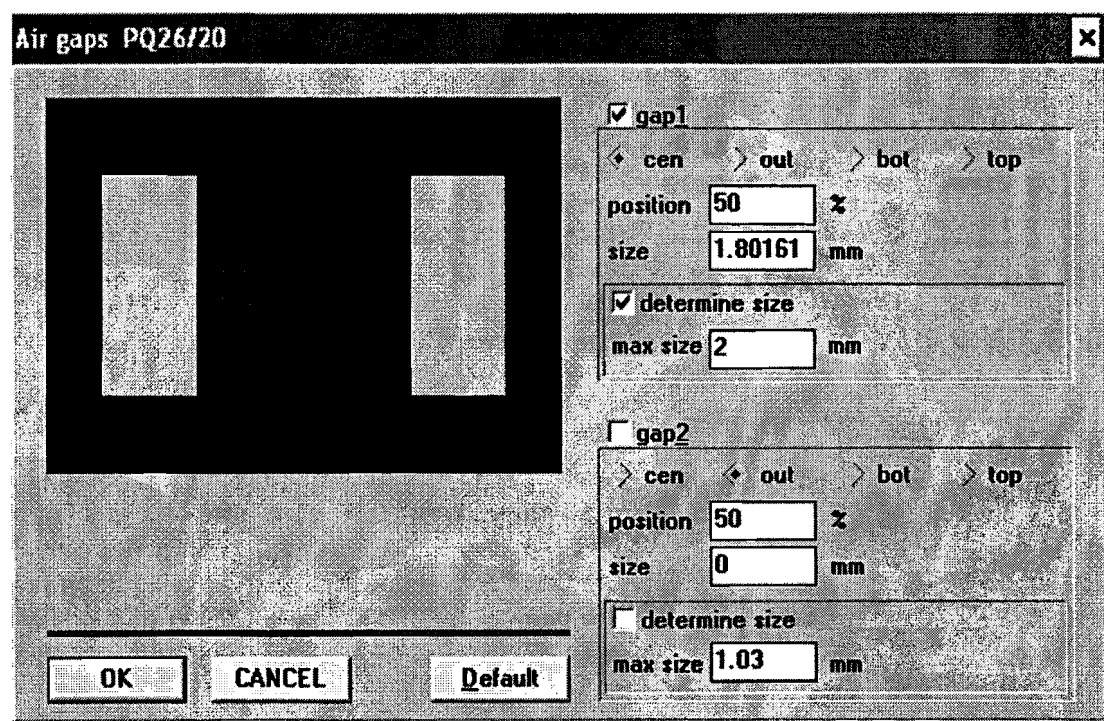
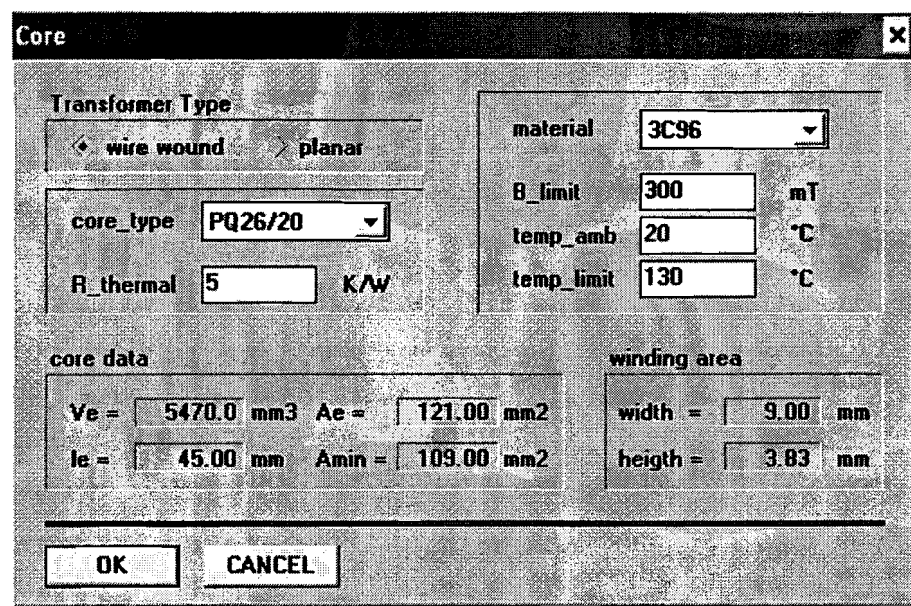
primary inductance	tolerance
$L_p$ L <sub>p</sub> <input type="text" value="0.006"/> mH	+ - <input type="text" value="5"/> %
Component Name:	
<input type="text" value="L2"/>	
turns ratios	Nprim/Nsec + - tol
N_1	<input type="text" value="0"/> + - <input type="text" value="5"/> %
N_2	<input type="text" value="0"/> + - <input type="text" value="5"/> %
N_3	<input type="text" value="0"/> + - <input type="text" value="5"/> %
N_4	<input type="text" value="0"/> + - <input type="text" value="5"/> %
N_5	<input type="text" value="0"/> + - <input type="text" value="5"/> %

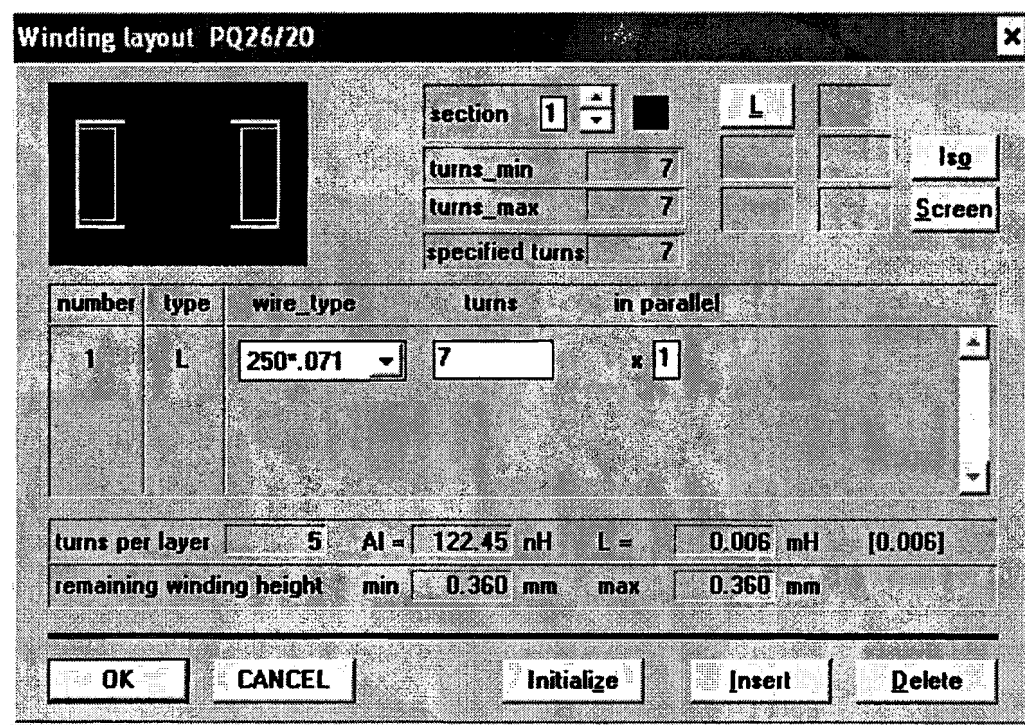
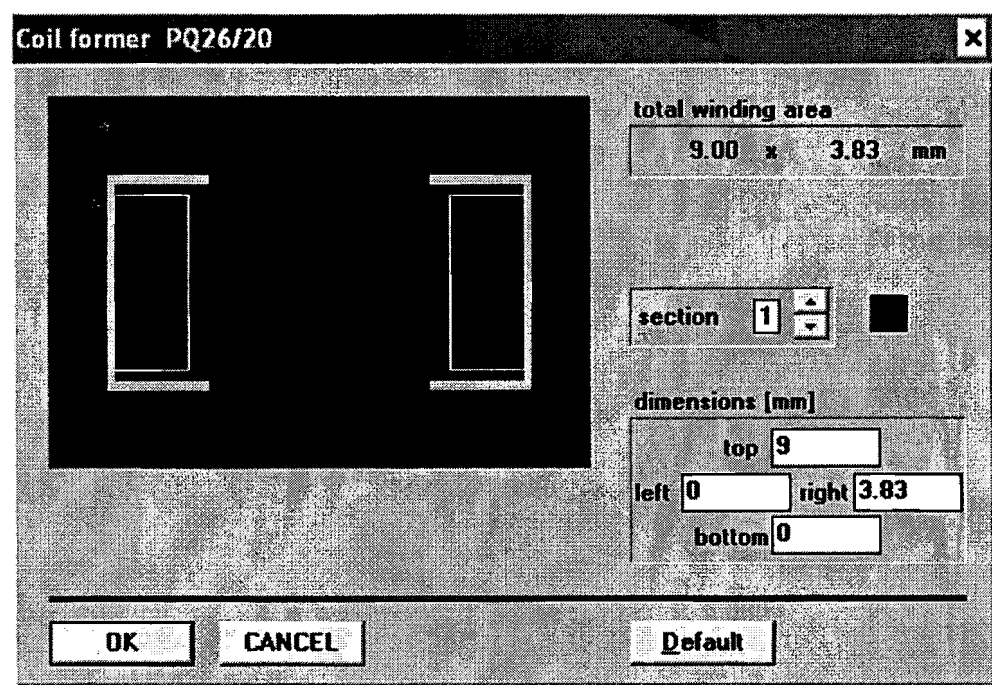
OK CANCEL

Sinewave Current <Choke>

i_L_peak	<input type="text" value="35"/> A
frequency	<input type="text" value="100"/> kHz

OK CANCEL





**Design Data: L2**

<b>Realized values (temp_amb)</b>		<b>Results</b>	
L <sub>p</sub>	0.006 [mH]	turns	L <sub>p</sub> 0.0059991 [mH] at 72.0 °C
N <sub>1</sub>			B <sub>max</sub> 248.0 [mT] for Ae
N <sub>2</sub>			B <sub>min</sub> -248.0 [mT] for Ae
N <sub>3</sub>			B <sub>max</sub> 275.3 [mT] for Amin
N <sub>4</sub>			B <sub>min</sub> -275.3 [mT] for Amin
N <sub>5</sub>			B <sub>sat</sub> 381 [mT] at 72.0 °C
<b>Core data</b>		AI	122.45 [nH]
PQ26/20	3C96	u_eff	36
		gap1	1.802 [mm]
		gap2	0.000 [mm]

**Total Losses: L2**

<b>Winding Losses [W]</b>							
	L <sub>p</sub>	L <sub>s1</sub>	L <sub>s2</sub>	L <sub>s3</sub>	L <sub>s4</sub>	L <sub>s5</sub>	total
rms	4.181						4.181
skin	0.645						0.645
proximity	0.637						0.637
<b>total</b>	<b>5.464</b>						

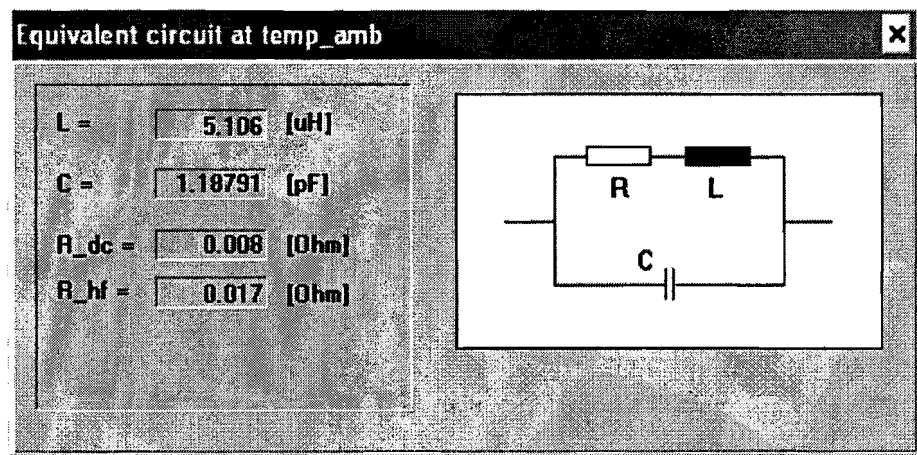
**Screen Losses [W]**

	rms	skin	prox	screen	core
--	-----	------	------	--------	------

**Core Losses [W]**

specific	4.258
eddy current	0.186

**Total Losses [W]** 9.908



## Appendix F

### Magtool results: $L_k$

Component

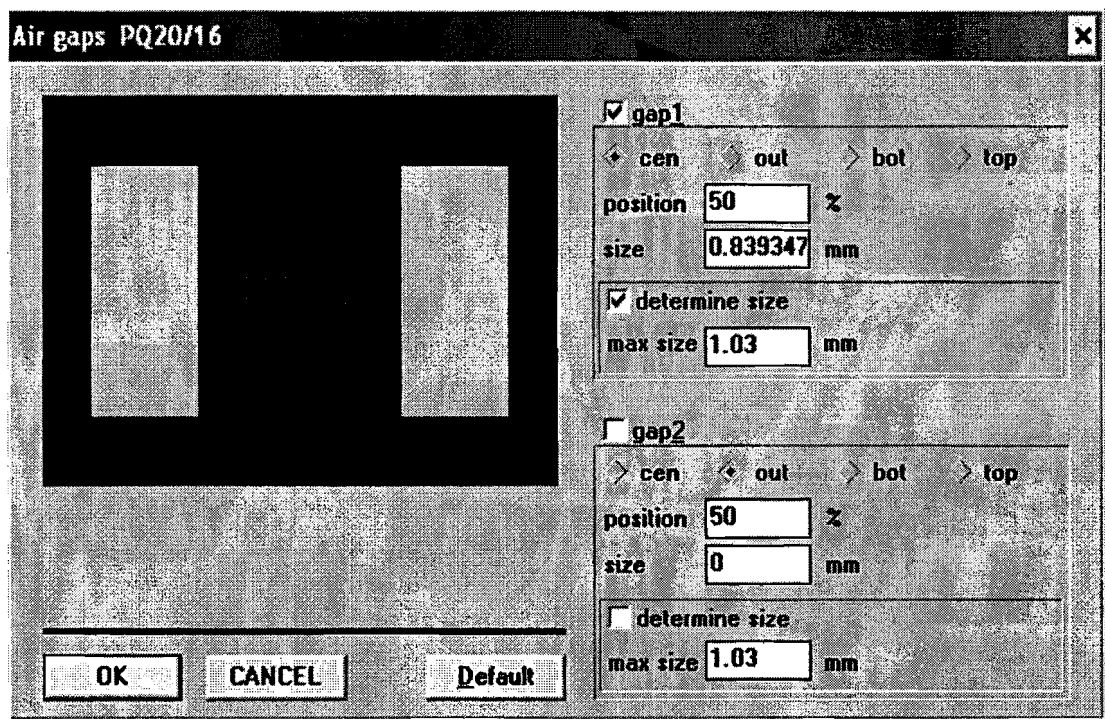
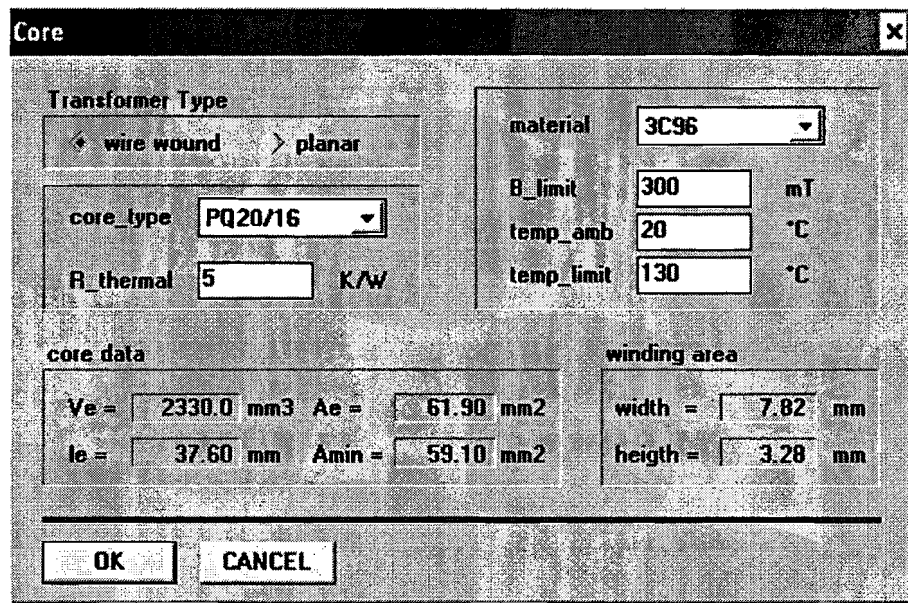
primary inductance	tolerance
$L_p$ 0.0012 mH	$\pm 5\%$
Component Name:	
Lk	
turns ratios Nprim/Nsec + tol	
N_1	0 $\pm 5\%$
N_2	0 $\pm 5\%$
N_3	0 $\pm 5\%$
N_4	0 $\pm 5\%$
N_5	0 $\pm 5\%$

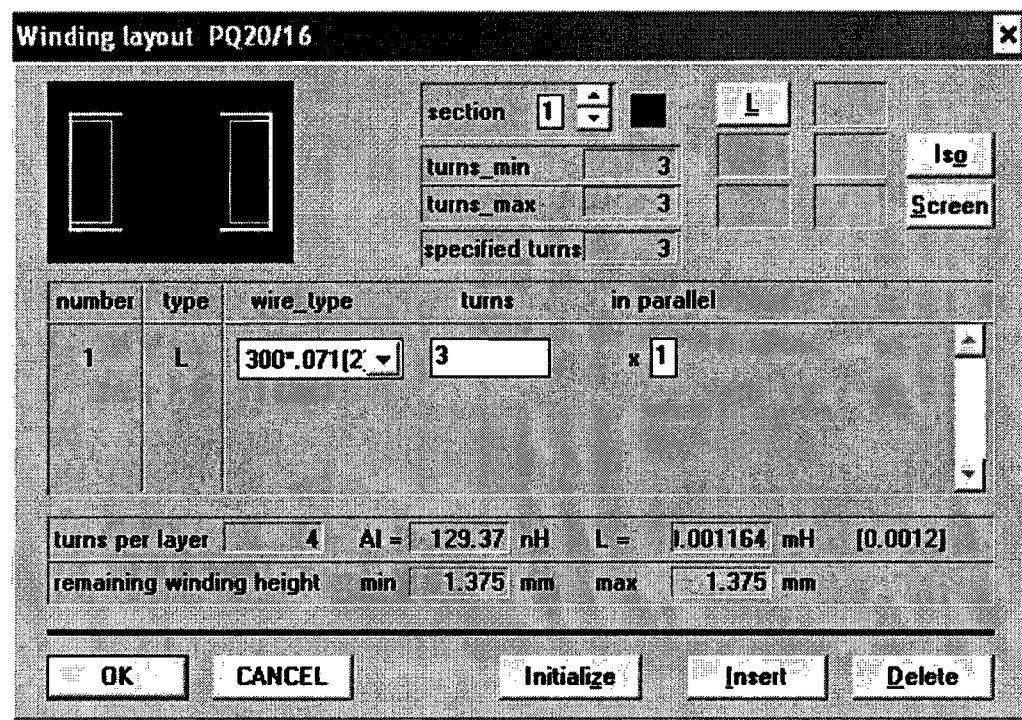
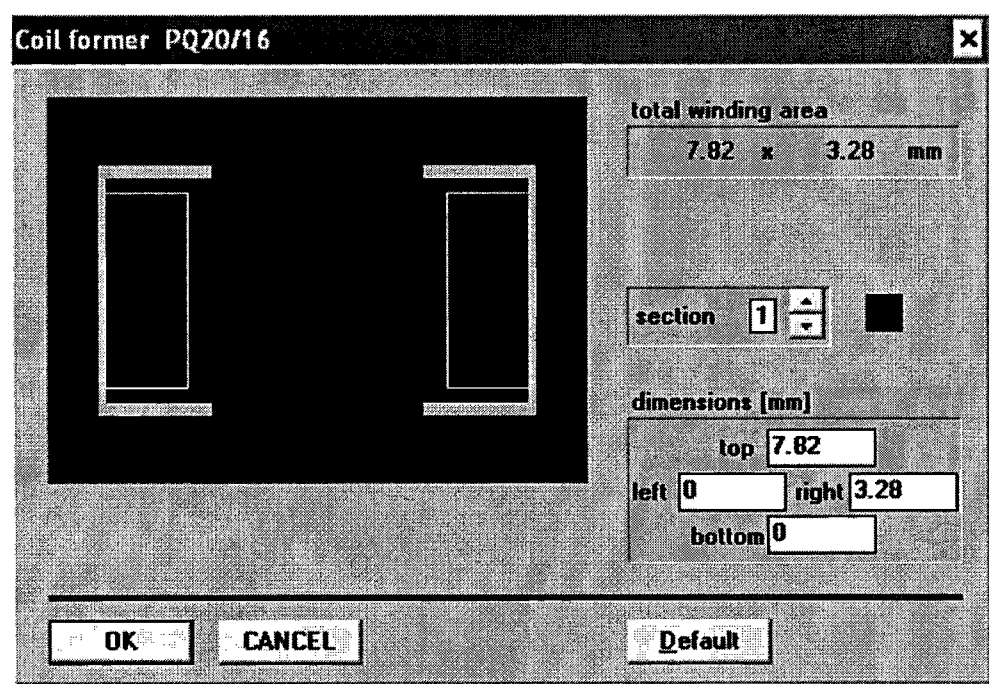
OK CANCEL

Sinewave Current «Choke»

i L_peak	45 A
frequency	100 kHz

OK CANCEL





**Design Data: Lk**

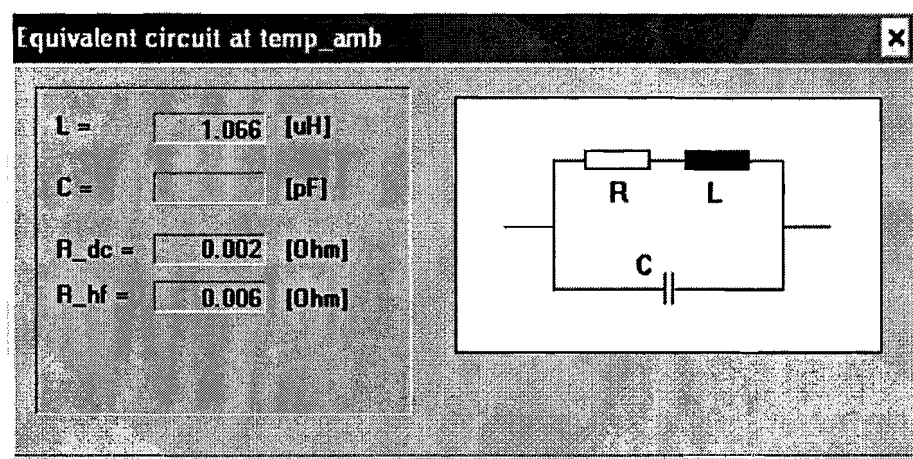
<b>Realized values (temp_amb)</b>		<b>Results</b>	
L <sub>p</sub>	1.0011643 [mH]	turns	L <sub>p</sub> 1.0011639 [mH] at 49.5 °C
N_1			B <sub>max</sub> 281.9 [mT] for Ae
N_2			B <sub>min</sub> -281.9 [mT] for Ae
N_3			B <sub>max</sub> 295.3 [mT] for Amin
N_4			B <sub>min</sub> -295.3 [mT] for Amin
N_5			B <sub>sat</sub> 407 [mT] at 49.5 °C
<b>Core data</b>		A <sub>i</sub> 129.37 [nH]	u <sub>eff</sub> 62
PQ20/16	3C96	gap1 0.839 [mm]	gap2 0.000 [mm]

**Total Losses: Lk**

<b>Winding Losses [W]</b>							
	L <sub>p</sub>	L <sub>s1</sub>	L <sub>s2</sub>	L <sub>s3</sub>	L <sub>s4</sub>	L <sub>s5</sub>	total
rms	2.002						2.002
skin	0.335						0.335
proximity	0.136						0.136
total	2.473						

<b>Screen Losses [W]</b>	
core	3.403
specific	3.403
eddy current	0.039

<b>Total Losses [W]</b>	
rms	5.916
skin	
prox	
screen	
core	



## Appendix G

### Power and control circuits discharging mode

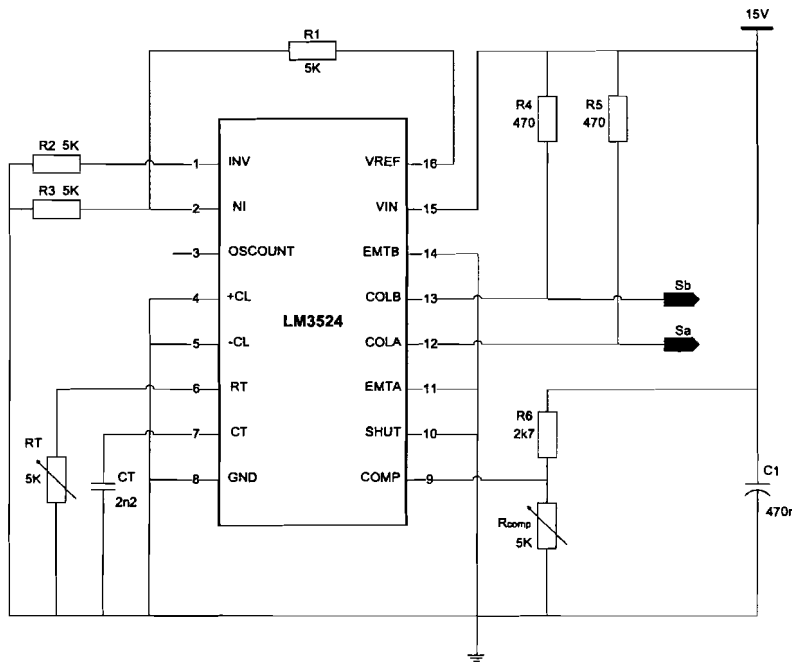


Figure G.1: Circuit used for implementing PWM signals

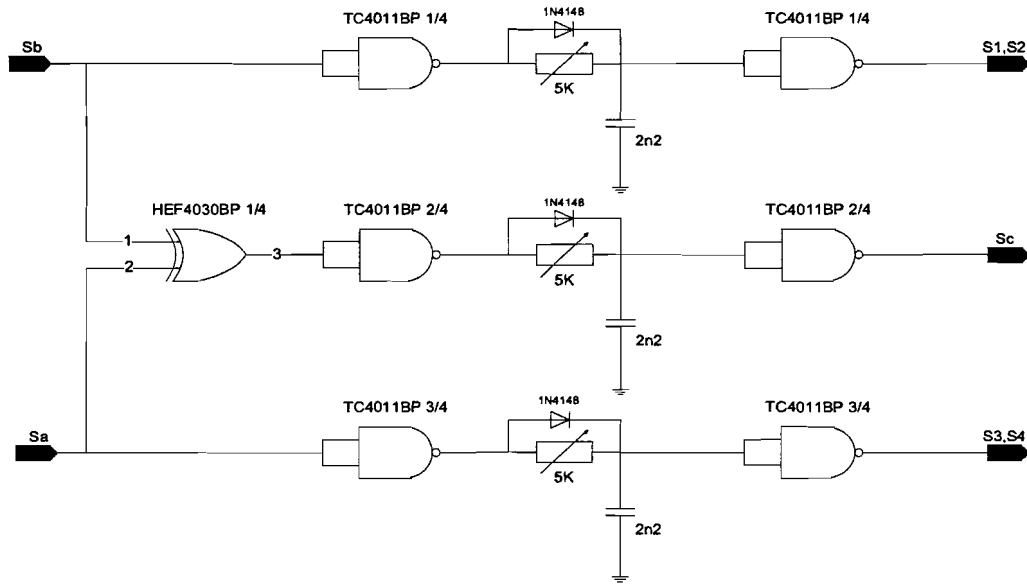


Figure G.2: Control circuit of  $S_c$  including deadtime circuit

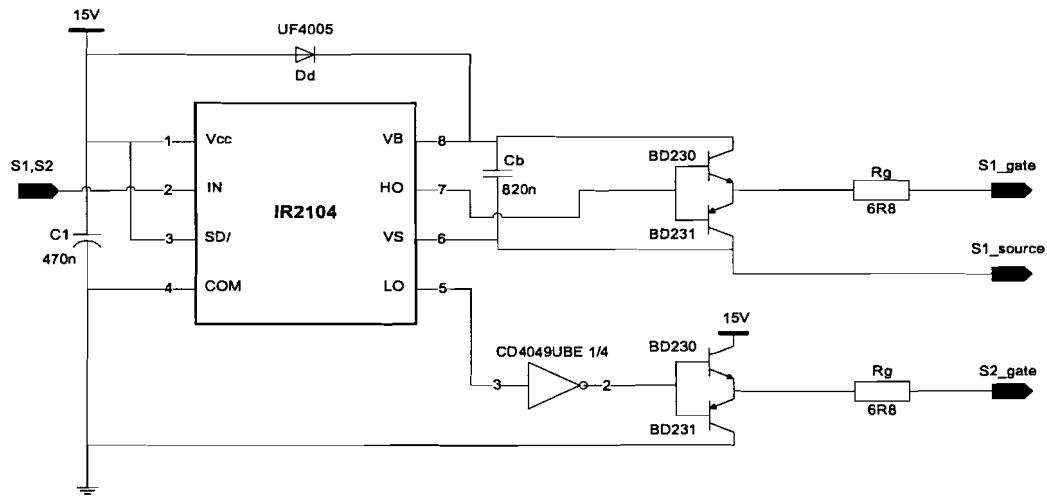


Figure G.3: Mosfet driver circuit of  $S_1$  and  $S_2$

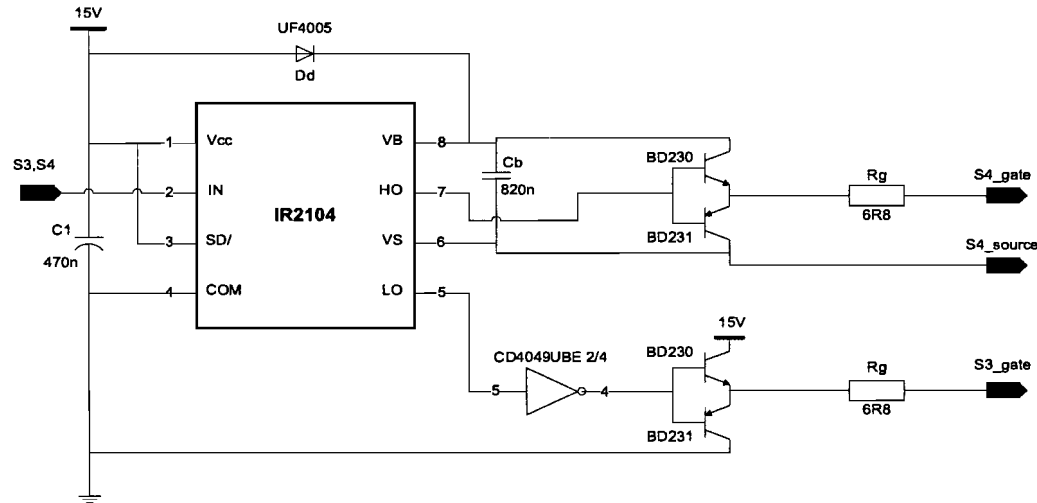


Figure G.4: Mosfet driver circuit of  $S_3$  and  $S_4$

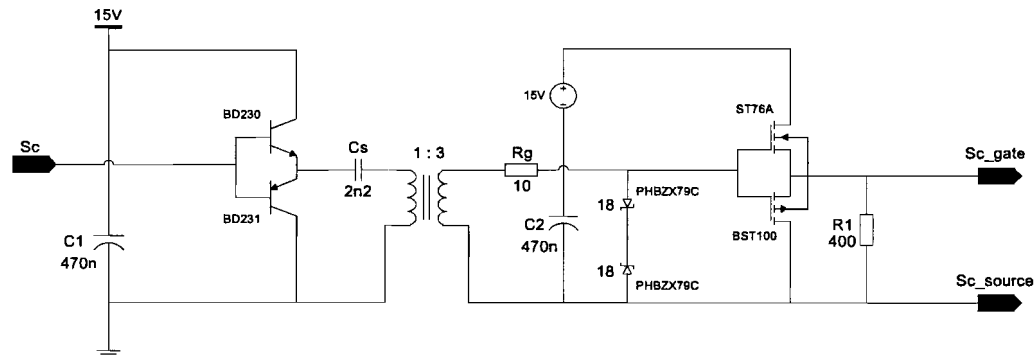


Figure G.5: Mosfet driver of  $S_c$

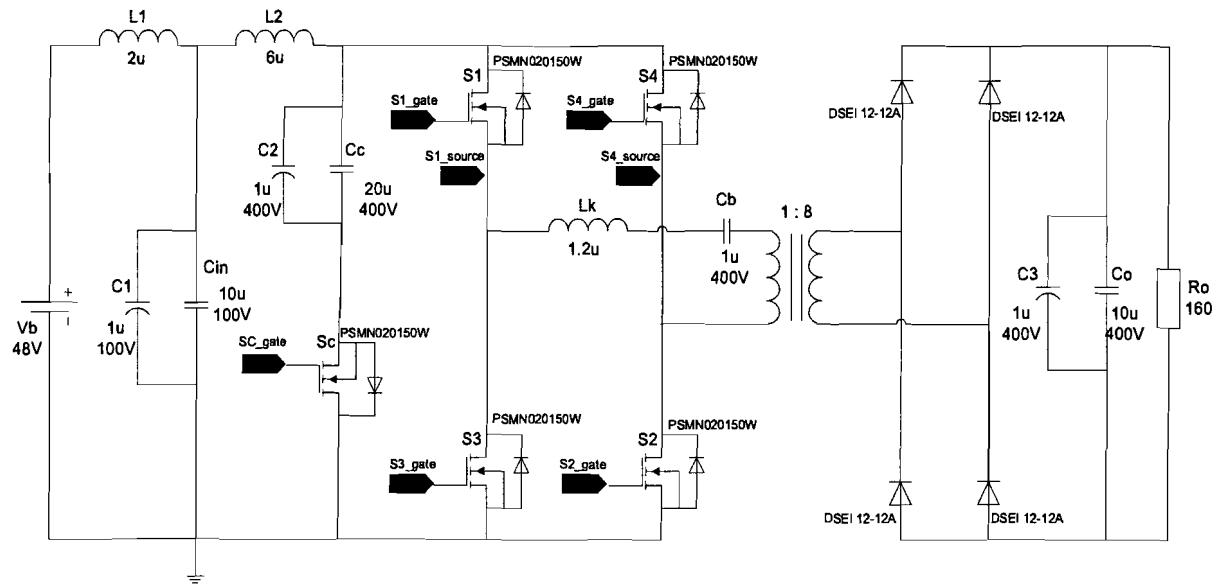


Figure G.6: Power stage component selection

## Appendix H

# Power and control circuits charging mode

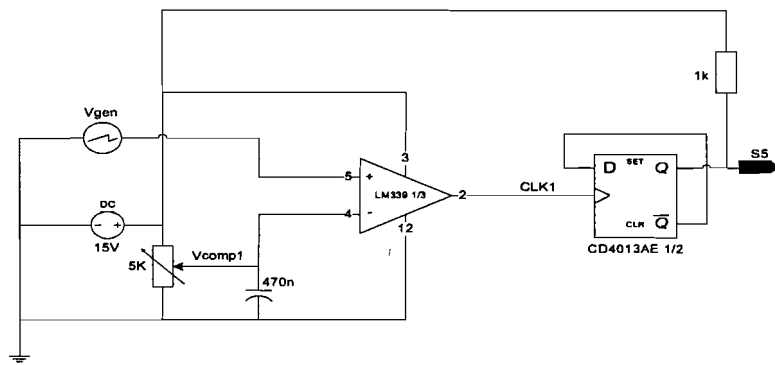


Figure H.1: Phase shift control of converter leg 1

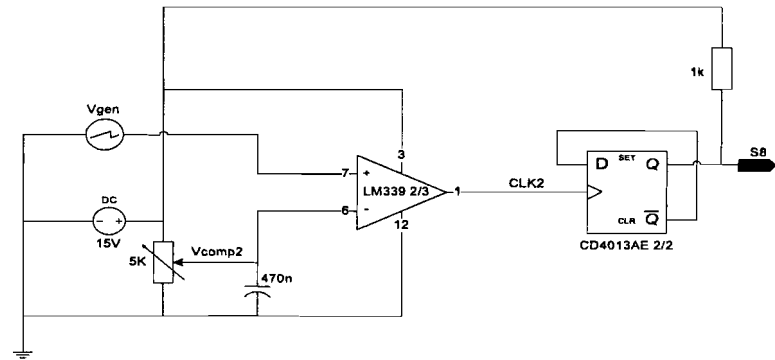


Figure H.2: Phase shift control of converter leg 2

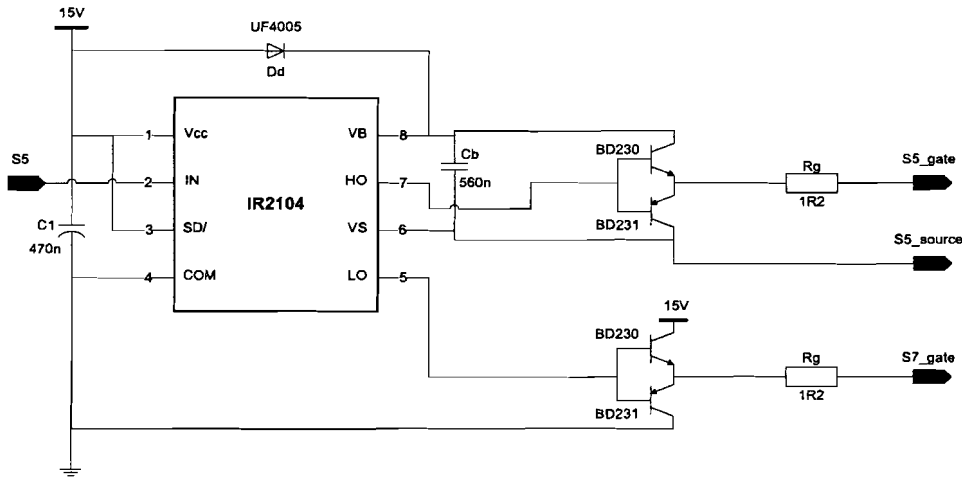


Figure H.3: Mosfet driver circuit of  $S_5$  and  $S_7$

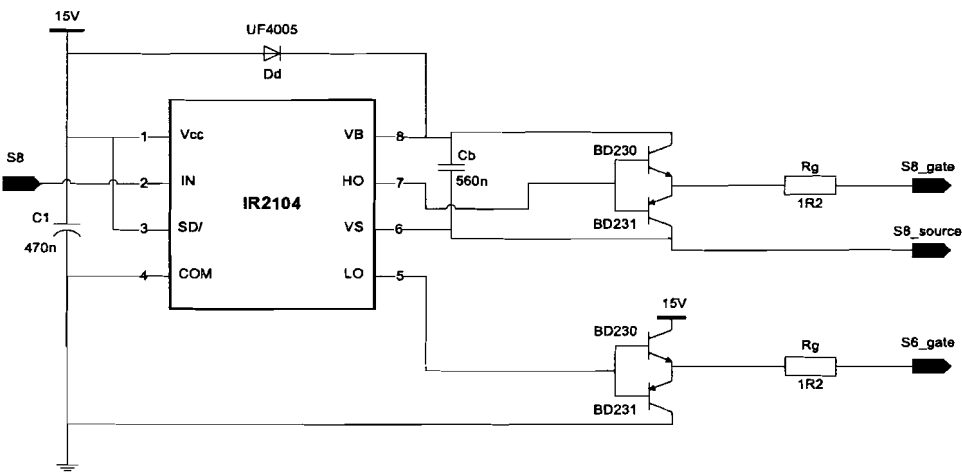


Figure H.4: Mosfet driver circuit of  $S_8$  and  $S_6$

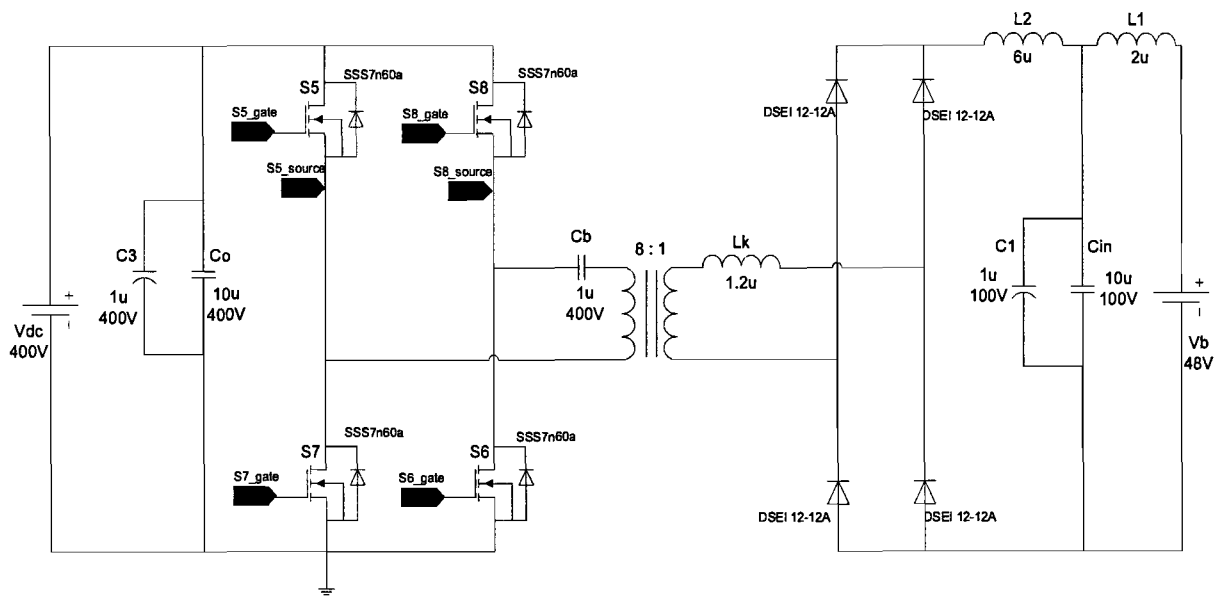


Figure H.5: Power stage component selection

# **Appendix I**

## **Pcad Schematic: Discharging mode**

Because of the size of the figure it is depicted on the next sheet.

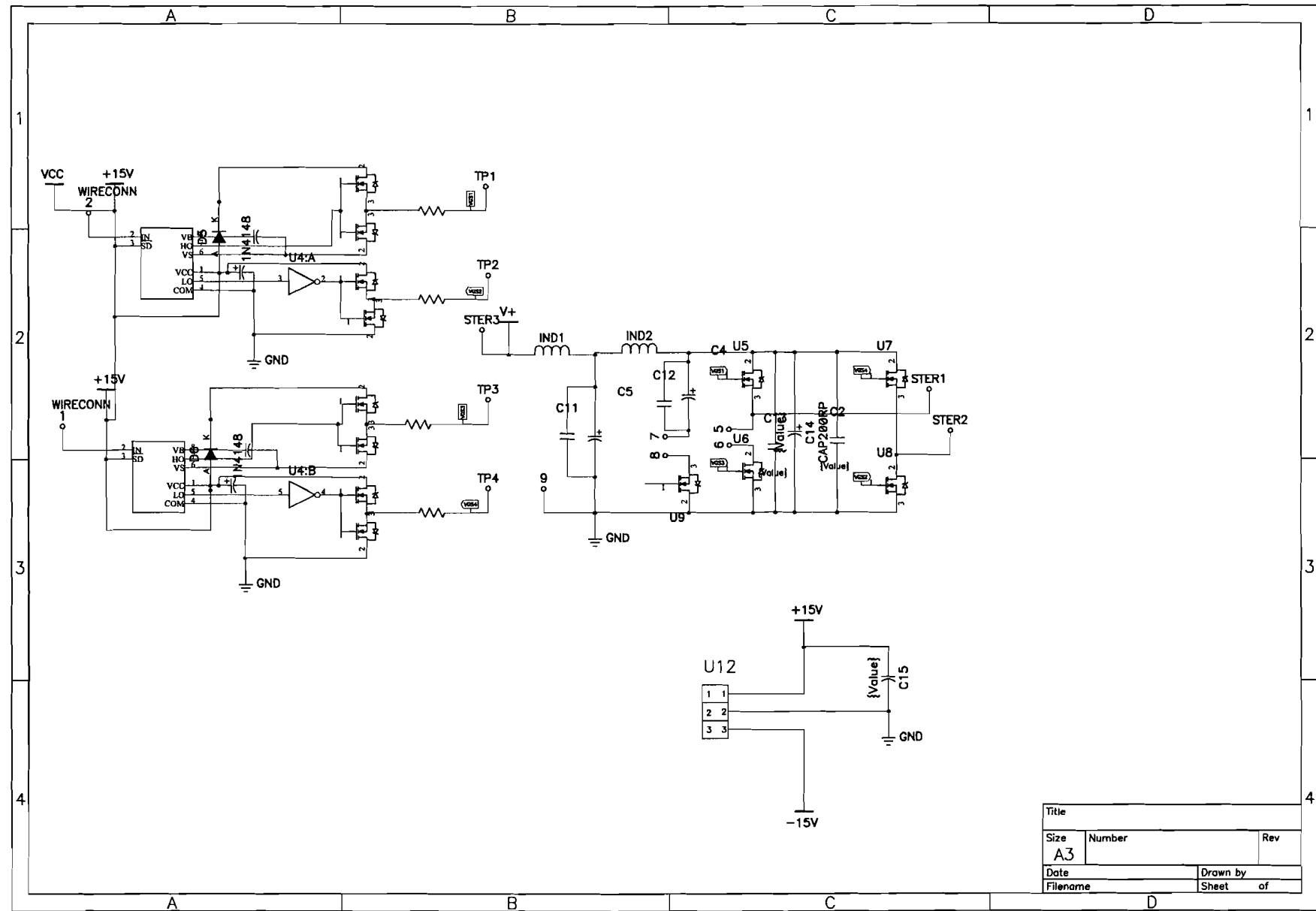


Figure I.1: Pcad schematic of discharging mode part 1

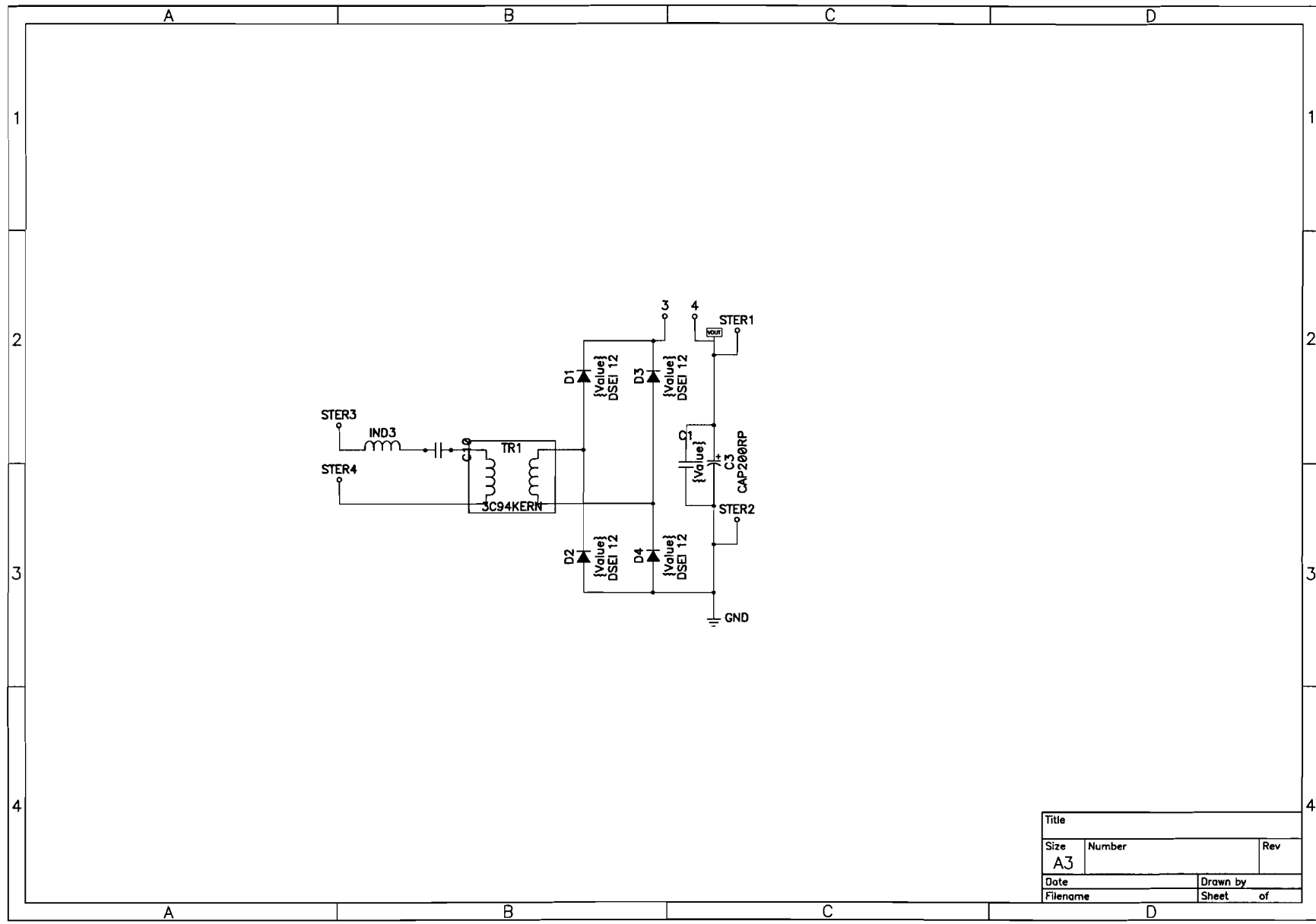


Figure I.2: Pcad schematic of discharging mode part 2

## **Appendix J**

### **Pcad Schematic: Charging mode**

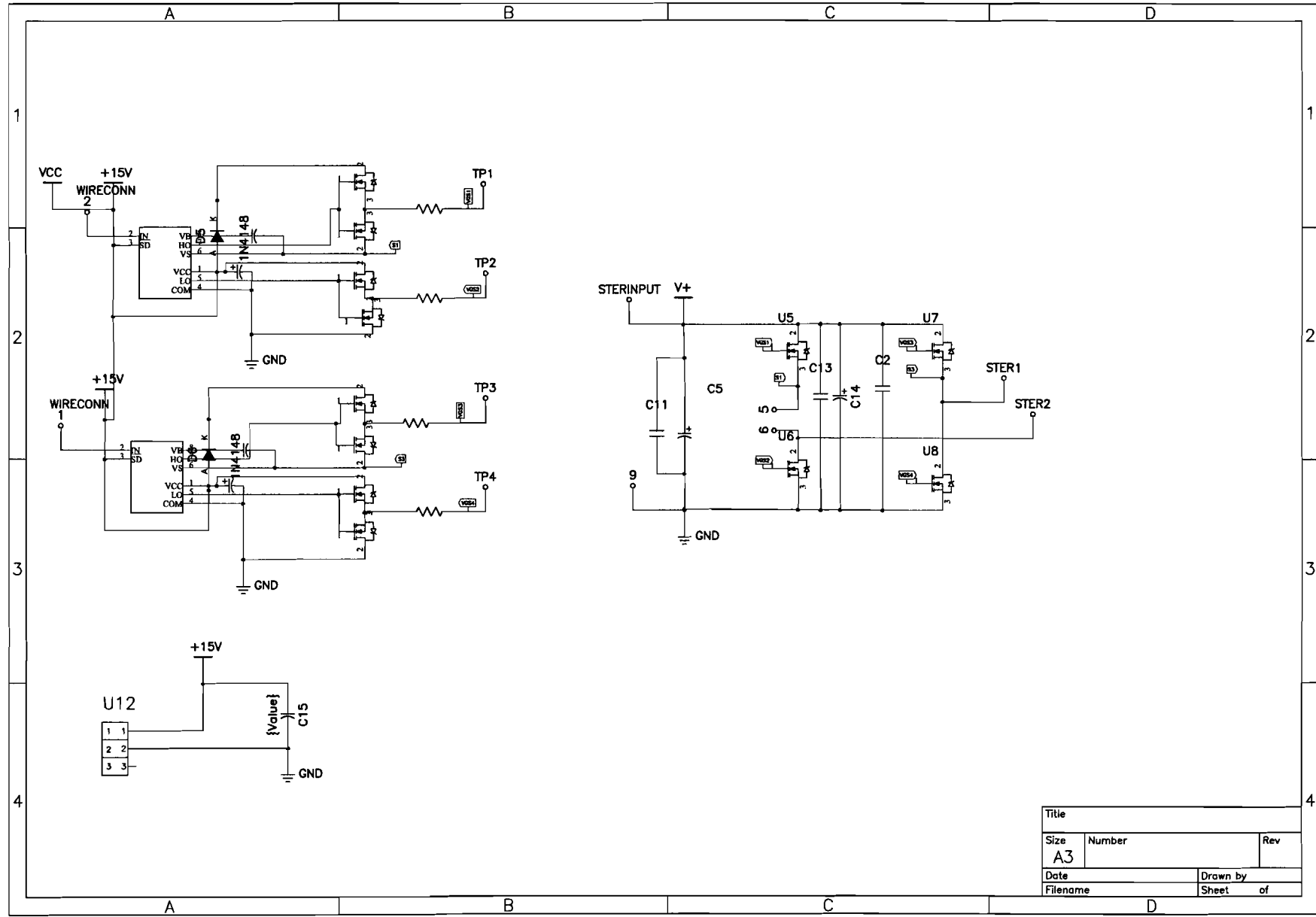


Figure J.1: Pcad schematic of charging mode part 1

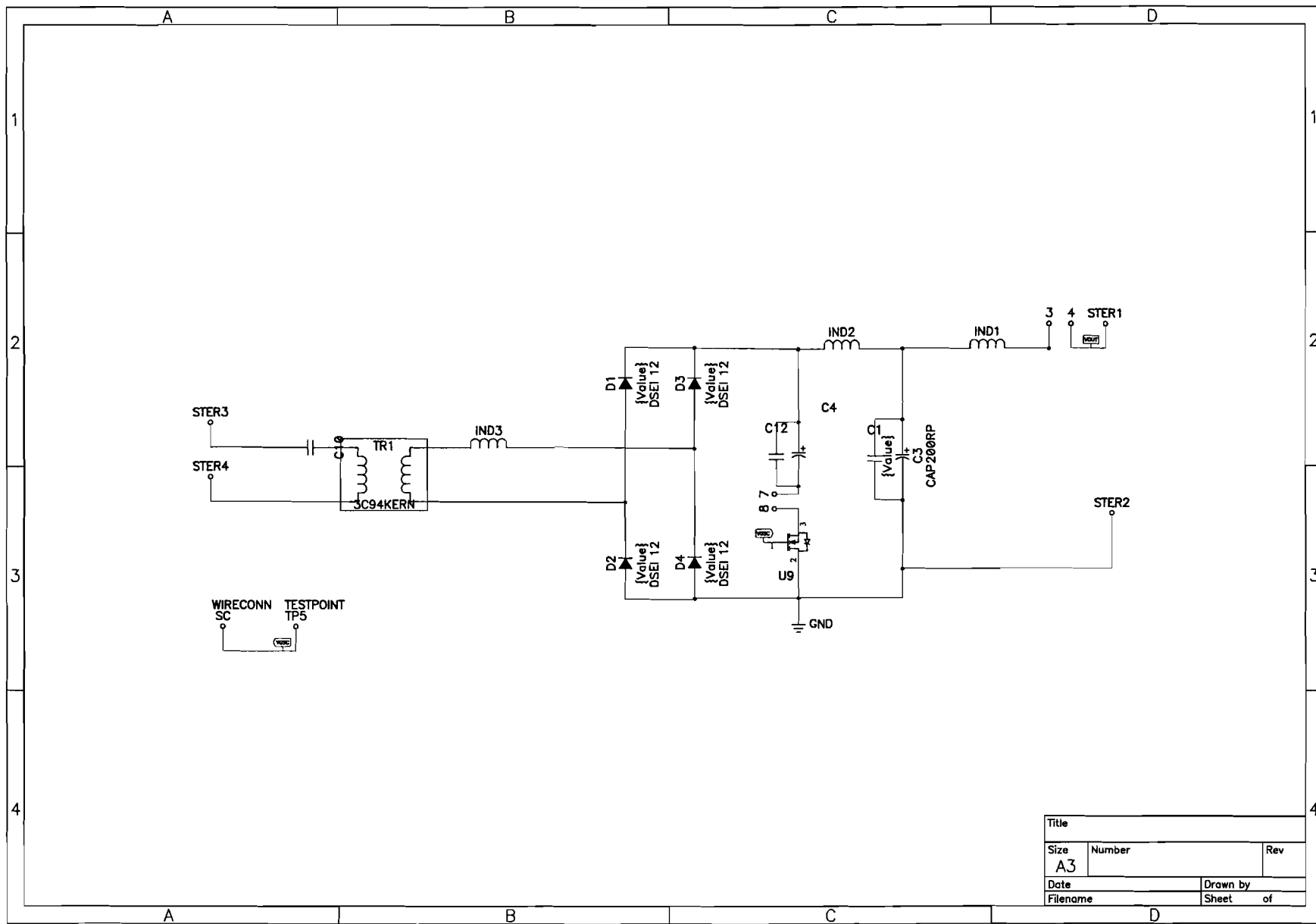


Figure J.2: Pcad schematic of charging mode part 2

# Appendix K

## Measurement results @ 100kHz

Measurements @ $F_s = 100kHz$						
$V_{in}(V)$	$I_{in}(A)$	$P_{in}(W)$	$V_{out}(V)$	$I_{out}(A)$	$P_{out}(W)$	$\eta = \frac{P_{out}}{P_{in}} \cdot 100$
4.6	2.0	9.2	40.0	0.21	8.4	91.3
9.6	4.0	38.4	75.0	0.45	33.8	87.9
11.9	5.0	59.5	92.5	0.55	50.88	85.5
14.2	6.0	85.0	110.0	0.67	73.7	86.7
18.8	8.0	150.4	145.0	0.88	127.6	84.8
23.2	10.0	232.0	180.0	1.09	196.2	84.6
27.6	12.0	331.2	215.0	1.30	279.5	84.4
31.9	14.0	446.6	247.5	1.50	371.3	83.1
34.0	15.0	510.0	265.0	1.60	424.0	83.1
36.0	16.0	576.0	277.5	1.72	476.9	82.8
39.9	18.0	718.2	310.0	1.91	593.2	82.6
43.9	20.0	878.0	342.5	2.11	724.4	82.5
47.8	22.0	1051.6	372.5	2.32	863.3	82.1

Table K.1: Measurement results of converter in discharging mode at  $F_s = 100kHz$

# Appendix L

## Measurement results @ 120kHz

Measurements @ $F_s = 120kHz$						
$V_{in}(V)$	$I_{in}(A)$	$P_{in}(W)$	$V_{out}(V)$	$I_{out}(A)$	$P_{out}(W)$	$\eta = \frac{P_{out}}{P_{in}} \cdot 100$
5.4	2.0	10.8	37.5	0.25	9.4	87.0
10.5	4.0	42.0	77.5	0.46	35.7	85.0
12.9	5.0	64.5	95.0	0.57	54.2	84.0
15.3	6.0	91.8	112.5	0.68	76.5	83.3
20.1	8.0	160.8	149.0	0.90	134.1	83.4
24.6	10.0	246.0	182.5	1.12	204.4	83.1
29.2	12.0	350.4	217.5	1.33	289.3	82.6
33.5	14.0	469.0	250.0	1.52	380.0	81.0
35.6	15.0	534.0	267.5	1.62	433.4	81.2
37.6	16.0	601.6	282.5	1.71	483.1	80.3
41.6	18.0	748.8	311.0	1.88	584.7	78.1
45.4	20.0	908.0	341.0	2.08	709.3	78.1
49.0	22.0	1078.0	366.5	2.29	840.8	78.0

Table L.1: Measurement results of converter in discharging mode at  $F_s = 120kHz$

# Appendix M

## Measurement results @ 80kHz

Measurements @ $F_s = 80kHz$						
$V_{in}(V)$	$I_{in}(A)$	$P_{in}(W)$	$V_{out}(V)$	$I_{out}(A)$	$P_{out}(W)$	$\eta = \frac{P_{out}}{P_{in}} \cdot 100$
3.9	2.0	7.8	32.5	0.20	6.5	83.3
7.6	4.0	30.4	64.0	0.40	25.6	84.2
9.4	5.0	47.0	80.0	0.49	39.2	83.4
11.3	6.0	67.8	95.0	0.59	56.1	82.7
14.6	8.0	116.8	125.0	0.78	97.5	83.5
18.6	10.0	186.0	157.5	0.99	155.9	83.8
22.3	12.0	267.6	187.5	1.18	221.3	82.7
26.0	14.0	364.0	220.0	1.38	303.6	83.4
27.8	15.0	417.0	235.0	1.48	347.8	83.4
29.6	16.0	473.6	250.0	1.57	392.5	82.9
33.3	18.0	599.4	282.5	1.77	500.0	83.4
36.8	20.0	736	311.0	1.95	606.5	82.4
40.3	22.0	886.6	340.0	2.14	727.6	82.1

Table M.1: Measurement results of converter in discharging mode at  $F_s = 80kHz$

# Appendix N

## List of equipment used for test setup

List of equipment for converter in discharging mode		
Apparatus	Type	Manufacturer
Power supply (Battery)	SM 70-22	Delta Elektronika
Power supply	E060-0.6	Delta Elektronika
Power supply	D030-1	Delta Elektronika
Differential probe	SI9000	
Differential probe	SI9000	
High voltage differential probe	P5205	Tektronix
Four channel digitizing oscilloscope	TDS-744A	Tektronix
Current probe	A6303	Tektronix
Current probe amplifier	AM503	Tektronix
Meter $I$	EM-534	
Meter $V$	EM-8	
RMS multimeter	PM2518	Philips
Infrared temperature probe	80T-IR	Fluke

Table N.1: List of equipment for converter in discharging mode

List of equipment for converter in charging mode		
Apparatus	Type	Manufacturer
High voltage power supply	BHK500-0.4	Kepco
Function/arbitrary waveform generator	33120A	Hewlett Packard
Power supply	D030-1.5	Delta Elektronika
Differential probe	SI9000	
Differential probe	SI9000	
High voltage differential probe	P5205	Tektronix
Four channel digitizing oscilloscope	TDS-744A	Tektronix
Current probe	A6303	Tektronix
Current probe amplifier	AM503	Tektronix
Meter $I$	EM-11	
Meter $V$	EM-192	

Table N.2: List of equipment for converter in charging mode